DEVELOPMENT OF A NEW GENERATION OF FLUORESCENT LABELING AGENTS BASED ON RARE-EARTH DOPED PHOSPHORS

TSANG MING KIU

M.Phil

The Hong Kong Polytechnic University

2014

THE HONG KONG
POLYTECHNIC UNIVERSITY
香港理工大學

Department of Applied Physics

Development of a New Generation of Fluorescent Labeling Agents Based on Rare-earth Doped Phosphors

Tsang Ming Kiu

A thesis submitted in partial fulfillment of the requirements for the degree of Master of Philosophy

July, 2013

CERTIFICATE OF ORIGINALITY

I hereby declare that this thesis is my own work and that, to the best of my knowledge and belief, it reproduces no material previously published or written, nor material that has been accepted for the award of any other degree or diploma, except where due acknowledgement has been made in the text.

_____ (Signed)

TSANG MING KIU (Name of student)

Abstract

Upconversion nanoparticles (UCNPs) have emerged as a new generation of fluorescent probes for bioimaging owing to their unique upconversion (UC) property. Traditional labeling agents, such as quantum dots (QDs), organic dyes and fluorescent proteins suffer from non-idealities such as autofluorescence and photobleaching. QDs have also inherent high toxicity which may pose potential health hazards. Therefore, these non-idealities limited their applications as labeling agents. In contrast, UCNPs are excited by near infrared (NIR) radiation and thus they offer reduced autofluorescence, photodamage and deep tissue penetration. Moreover, they have low toxicity and high resistance to photobleaching. This work aims to develop new types of UC materials for multi-modal bioimaging based on rare-earth doped UCNPs. The UCNPs are synthesized by one-step and facile hydrothermal synthesis and then characterized by transmission and scanning electron microscopy, Fourier transform infrared spectroscopy, photoluminescence, X-ray diffraction, vibrating sample magnetometer, confocal optical microscopy and cytotoxicity.

Firstly, $NaGdF_4$:Yb/Er phosphors are synthesized by various surface modifiers via hydrothermal synthesis. The red to green ratio of UC emission and crystal phase variations are observed. Therefore, rational choices of surface modifiers can tailor the UC and structural properties of UCNPs. Moreover, these phosphors demonstrate paramagnetic and cathodoluminescence properties, which are suitable for applications in magnetic resonance imaging (MRI) and bioseparation.

Additionally, barium based UCNPs have pure simple cubic phase structure, eliminating the phase transition issue. Novel PEI-modified Ba_2LaF_7 UCNPs possess small average size suitable for bioimaging. The Ba_2LaF_7 UCNPs achieved *in-vitro* bio-imaging at low concentration and the corresponding images are clearly recorded in green and red channel. Besides, fluorescent imaging in HeLa cells and MRI with various concentrations are successfully demonstrated using multi-functional PEI-modified $BaGdF_5$:Yb/Er UCNPs. The cytotoxicity assay confirms the low toxicity nature of $BaGdF_5$:Yb/Er UCNPs. Moreover, PEG-modified $BaGdF_5$:Yb/Er UCNPs consist of Ba and Gd elements which show strong X-ray k-edge absorption values. The $BaGdF_5$:Yb/Er UCNPs are injected intravenously into a living mouse and the spleen is clearly imaged under irradiation of X-ray with a circulation time of 2 h. Importantly, a tri-modal UC/MRI/computed X-ray tomography bioprobe is developed in a single phased compound by one-step hydrothermal method.

In conclusion, a facile technique for controlling UC and crystal phase provides a low cost and simple strategy for synthesizing tailor-made UC phosphors. Also, PEI-modified Ba_2LaF_7 UNCPs have no problem with phase transition and they are able to demonstrate clear fluorescent imaging. Moreover, multi-functional $BaGdF_5$:Yb/Er UCNPs are very useful multi-modal bio-imaging agent because three imaging techniques are integrated in one simple system and the corresponding advantages of one imaging technique can compensate the weakness of the others. Owing to low inherent toxicity, it is expected that the barium based UC materials are useful multi-modal bio-imaging agent.

List of publications

Peer-reviewed Journals

1. Ming-Kiu Tsang, Songjun Zeng, Helen L.W. Chan and Jianhua Hao, "Surface ligand-mediated phase and upconversion luminescence tuning of multifunctional $NaGdF_4$:Yb/Er materials with paramagnetic and cathodoluminescent characteristics**", Optical Materials**, 2013, **12**, 2691-2697. (IF:1.918)
2. Ming-Kiu Tsang, Songjun Zeng, Helen L.W. Chan and Jianhua Hao, "One-step synthesis and upconversion fluorescence of water-soluble Ba_2LaF_7:Yb/Er nanoparticles for bioprobe application", (Special issue in **Materials Science and Engineering: C**, EMRS 2013 spring meeting 27th May to 31st May 2013) (Submitted). (IF: 2.404)
3. Songjun Zeng, Ming-Kiu Tsang, Chi-Fai Chan, Ka-Leung Wong, Bin Fei and Jianhua Hao, "Dual-modal fluorescent/magnetic bioprobes based on small sized upconversion nanoparticles of amine-functionalized $BaGdF_5$:Yb/Er", **Nanoscale,** 2012, **4**, 5118-5124. (IF: 6.233)
4. Songjun Zeng, Ming-Kiu Tsang, Chi-Fai Chan, Ka-Leung Wong and Jianhua Hao, "PEG modified $BaGdF_5$:Yb/Er nanoprobes for multi-modal upconversion fluorescent, in vivo X-ray computed tomography and biomagnetic imaging", **Biomaterials,** 2012, **33**, 9232-9238. (IF: 7.604)

5. Hon-Tung Wong, Ming-Kiu Tsang, Chi-Fai Chan, Ka-Leung Wong, Bin Fei and Jianhua Hao, "In vitro cell imaging using multifunctional small sized $KGdF_4:Yb^{3+},Er^{3+}$upconverting nanoparticles synthesized by a one-pot solvothermal process", **Nanoscale**, 2013, **5**, 3465-3473. (IF: 6.233)

Presentations in international conferences

1. Ming-Kiu Tsang, Songjun Zeng and Jianhua Hao, "Synthesis and Characterizations of $NaGdF_4$ Nanoparticles for Biomedical Applications", **International Symposium on Integrated Functionalities 2012**, the Hong Kong Polytechnic University, Hong Kong, 21st June 2012.
2. Ming-Kiu Tsang, Songjun Zeng, Chi-Fai Chan, Ka-Leung Wong, Helen L.W. Chan and Jianhua Hao, "Fluorescent imaging bioprobe based on water soluble Ba_2LaF_7:Yb/Er upconversion nanoparticles", **European Materials Research Society 2013 Spring meeting**, Strasbourg, France, 28th June 2013.
3. Ming-Kiu Tsang, H. L. W. Chan and Jianhua Hao, "Upconverting nanoparticles for optofluidic bioimaging systems", to be presented in **The 3rd International Conference on Optofluidics 2013**, Hong Kong, August 15-17, 2013 (Best paper award).

Acknowledgements

I would like to express my appreciation to my supervisors Dr. J. H. Hao and Prof. Helen L.W. Chan for their excellent guidance and constant encouragement throughout the whole period of my research work.

Moreover, I would like to thank Dr S. J. Zeng for his encouragement and technical support in synthesis and characterizations. I would also like to thank the support of Mr. C. F. Chan and Dr. K. L. Wong of the Hong Kong Baptist University for assisting in *in-vitro* bioimaging and cytotoxicity test. Also, I would like to thank Dr. H. T. Wong for giving useful advices and guidance in synthesis and VSM measurement. In addition, I would like to thank Dr. T. L. Chan for teaching me the operation of SEM.

I gratefully acknowledge the financial support from the Innovation and Technology Fund of the HKSAR Government (ITS/008/10) and technical support provided by the Materials Research Centre of the Hong Kong Polytechnic University.

Last but not least, I would like to thank my parents and girlfriend for their understanding, constant support and encouragement.

Table of contents

List of figures and table

Chapter 1 Introduction

1.1 Photoluminescence

Luminescence is the phenomenon that the electronic state of a substance is agitated by external excitation, such as electrical, photo or thermal energy, and subsequently the emitted energy is released in the form of photons. The emission does not confine in the visible region (400 to 700 nm) of the electromagnetic wave spectrum, but also the neighboring regions such as, ultraviolet (UV) and infrared (IR) regions [1]. In this work, photoluminescence (PL) is the major process that accounts for the emission of the rare-earth (RE) doped phosphors. PL is initiated by the absorption of electromagnetic radiation. Schematically, the mechanism of PL can be explained by Fig. 1.1. In general, a photoluminescent material consists of a host material and activator ions. The host material is a crystal or a grain in which activators are well occupied in the lattice sites of the host materials. Fig. 1.1a shows a simple system which consists of host material and activators. In this system, the activator ions (denoted as 'A') are excited by the incoming energy directly and return to ground state to emit a photon. The excessive energy is dissipated as heat and emit as phonons. As a result, the emitted energy does not equal to the excitation energy and this is known as the Stoke shift process ($h\upsilon_2 < h\upsilon_1$). For example, $GdF_3:Eu^{3+}$ nanocrystals consist of the host material GdF_3 and the activator Eu^{3+} ions. The nanocrystals are excited by UV and emit visible radiation [2].

To date, co-doped ion system is very popular because sensitizer ions are doped into the host material to enhance the emission efficiency of the photoluminescent material. Fig. 1.1b shows a sensitizer (denoted as 'S')-activator system, sensitizer ions are doped to assist the absorption of incoming photons and thus enhancing the efficiency of energy transfer type PL. Sensitizer ions, such as Yb^{3+} ions, are doped into host material to solve the problem of poor absorption cross section of activator ions. Common upconverting nanoparticles, $NaYF_4$:Yb/Er, rely on Yb^{3+} ions to facilitate energy transfer between neighboring ions for efficient upconversion photoluminescence because Er^{3+} ions exhibit poor absorption cross section in near infrared (NIR) region, thus Yb^{3+} ions can assist the absorption of NIR energy [3-5]. Similar to Fig. 1.1a, the transferred energy eventually reaches the activator ions and results in the emission of photons.

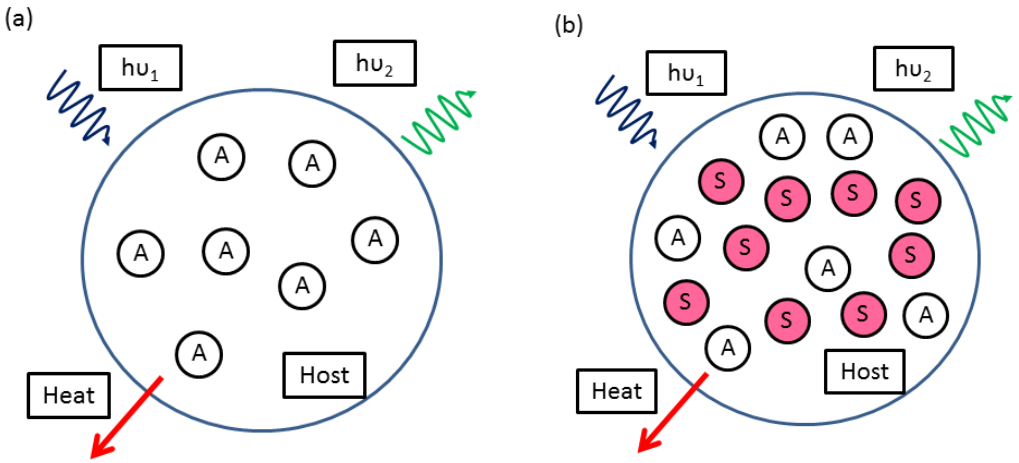

Figure 1.1 Schematic diagram of (a) Host-activator photoluminscent material with activator labeled as 'A' (b) Sensitizer-activator co-doped photoluminscent material with sensitizer ion labeled as 'S' and activator ion as 'A'.

1.2 Upconversion

In optics, there are two kinds of processes: linear optics and non-linear optics. In the former process, the optical property of the materials is independent of the intensity of the incident light. Besides, non-linear optical process is describing the dependence of the optical material on the intensity of the incoming radiation. Upconversion (UC) refers to non-linear optical processes that facilitate successive multi-absorption of two or more pumping photons to convert lower energy photons into higher energy photons [6]. The UC phenomena can be further divided into three types of processes: excited state absorption (ESA), energy transfer upconversion (ETU) and photon avalanche (PA) [7-9]. The three processes are based on the nature of ladder-like energy levels and long life time of the metastable states of RE ions. Therefore, the unique property of UC materials enables successive absorption of two or more photons. However, it should be noted that UC process should be distinguished from multi-photon processes (MP) and second harmonic generation (SHG), in which simultaneous absorption of two or more photons and high excitation power are required [10-13].

1.2.1 Excited state absorption

Firstly, excited state absorption is the simplest process among the UC phenomena and it facilitates sequential absorption of two or more photons by a single activator ion. A simplified energy level diagram is shown in Fig. 1.2a to aid the understanding of the process. According to Fig. 1.2a, if the energy of photon equals to the difference of G and E1, the photon will resonant the ions and thus the ion will populate E1 from G in a process known as ground state absorption (GSA). Owing to the

long life time of metastable state, the ion absorbs the second photon and populates E2. The downward transition from E2 to G results in UC emission [12], [14-15].

1.2.2 Energy transfer upconversion

To a certain extent, the ESA process is comparable to the energy transfer upconversion (ETU) due to its sequential absorption of photons to populate the activator ion to higher energy levels. The basic difference between ESA and ETU is the manifestation of energy transfer between neighboring ions. In order to realize ETU process, Fig. 1.2b shows two ions where the ion on the left is a sensitizer ion and the right one is an activator ion. The two independent ions absorb the incoming pumping photon simultaneously and results in population of E1. Eventually, the sensitizer ion returns from E1 to G and emits a phonon to resonant to the neighboring activator ion. As a result, the activator ion is promoted to E2 and return to G for UC emission. It is important to note the average separation of ions is determined by the concentrations of doping ions which affects the UC efficiency significantly [12], [14-15].

1.2.3 Photon avalanche

The photon avalanche (PA) phenomenon was introduced by Chivan's group and the observation was based on a Pr^{3+} ion infrared quantum counter. The uniqueness of PA is distinguished in high pumping power to overcome the threshold PA value. The mechanism of PA can be explained by the simplified energy level diagram in Fig. 1.2c. PA starts with the population of ion from G to E1 by non-resonant weak GSA. After that, resonant ESA populate E2 (The transition of E2 to E1 is eye-visible radiation) for setting up of metastable state. Then, energy transfer takes place between excited ion and

a neighboring ion at G. Hence, two ions will occupy E1. This process continues for intense UC emission and known as PA [12], [14-16].

1.2.4 Energy migration upconversion

Recently, a new upconversion process termed EMC was discovered and this process requires a well-defined core-shell structure UCNPs. The RE ions are well distributed in the core and shell. For example, the core is $NaGdF_4$:Yb/Tm and the shell is $NaGdF_4$:Tb [9]. To aid the understanding of EMC, fig. 1.2d shows a simplified energy level diagram with two zones. The first zone is the core region consisting of type I ion (sensitizer), type II ion (accumulator) and type III ion (migrator) while the second zone is the shell region consisting of migrator and type IV ion (activator) [8-9]. Similar to ETU and PA, this process is initiated by sensitization of pumping photon and populating the accumulator ions to higher energy states. Then, the migrator ion extracts the energy and transfer to neighboring migrator ions by exchange interaction Eventually, the transferred energy arrives at the activator ion and released as visible photons [8-9].

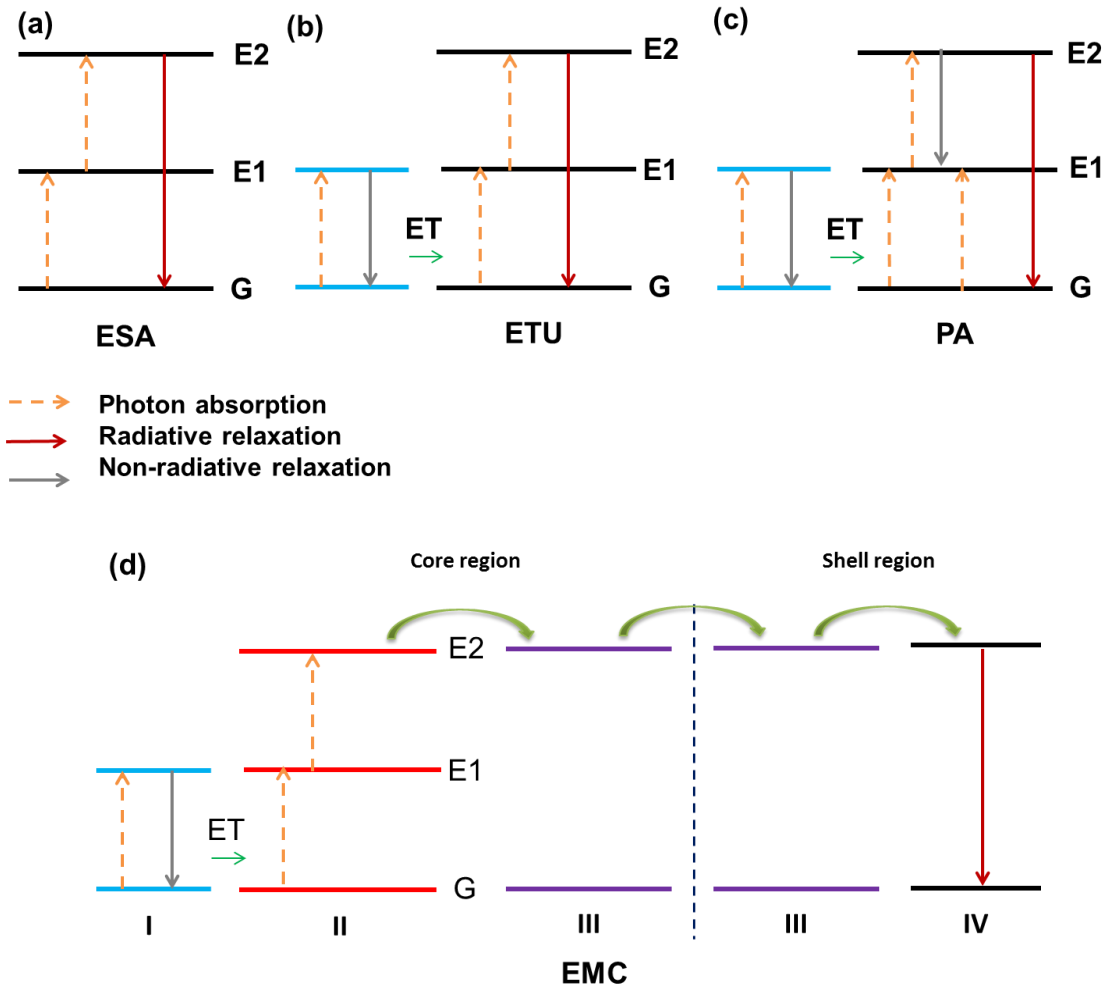

Figure 1.2 Simplified energy level diagram showing different type of upconversion processes: (a) excited state absorption (ESA) (b) energy transfer upconversion (ETU) (c) photon avalanche (PA) (d) energy migration upconversion (EMC) with ground state (G), energy levels (E1 and E2) and energy transfer (ET).

1.2.5 Upconversion efficiency

After the introduction of different types of UC process, it is worthwhile to compare their efficiencies. Among them, ESA is the least efficient process. PA may be an efficient UC process because the establishment of metastable state for photon storage. Unfortunately, PA suffers from some non-idealities such as, high pump power, slow response time looping of ESA cycles and cross-relaxation processes. In contrast, ETU process is fast and independent of pump power. Therefore, ETU has been employed in the development of advanced upconverting nanoparticles for various applications over the past decades [12], [14-15]. Moreover, Auzel has reported that the UC efficiency of ETU is higher than ESA by about two orders of magnitude [6].

1.3 Properties of trivalent rare-earth ions

Nowadays, trivalent RE ions have found many applications in bio-labeling, laser, solid state lightings and displays [17-20]. This is due to various properties of RE ions including luminescence and magnetism. In this work, the luminescence and magnetism of RE doped fluoride phosphors are studied extensively for bio-labeling applications and thus the properties of some RE ions are highlighted in this section. From Table 1.1, those RE ions that lack 4f electrons, such as Sc^{3+}, Y^{3+} , La^{3+} and Lu^{3+} lack electronic energy levels in or near the visible region. Other 4f electron-possessing RE ions has partial filled 4f orbitals such as, Ce^{3+} to Yb^{3+} ions, is usually doped in the photoluminescent materials and contributes to different emission characteristics of the photoluminescent materials. The electronic states of different energy levels are characterized by the term symbol. The term symbol is defined as $^{2S+1}L_J$ with S, L and J

representing spin angular momentum, orbital angular momentum and total angular momentum respectively. Fig. 1.3 shows the energy levels (electronic states) of various RE ions to explain the energy transfer and existence of UC emission peaks in this work.

1.3.1 Luminescence property of co-doping Er and Yb ion

Nowadays, common rare-earth doped phosphors (REPs) are doped with Er^{3+} and Yb^{3+}. In this case, 980 nm laser is used as an excitation source because the photon energy matches well with the energy difference between $^2F_{5/2}/^2F_{7/2}$ of Yb^{3+} ions and $^4I_{11/2}/^4I_{15/2}$ and $^4F_{7/2}/^4I_{11/2}$ of Er^{3+} ions (Fig. 1.3). As a result, this combination can enable efficient energy transfer between Yb^{3+} and Er^{3+} ions for UC emission. Usually, Yb^{3+} ions are doped into the host lattice with high concentration of about 18-20 mol% [12]. In fact, Er^{3+} ion is known to emit green and red colors and the observation of these colors are mainly due to the three transitions $^2H_{11/2}/^4S_{3/2} \rightarrow {}^4I_{15/2}$ and $^4F_{9/2} \rightarrow {}^4I_{15/2}$ with corresponding UC emission center wavelengths at about 521, 544 and 660 nm [21-26].

1.3.2 Magnetic property of Gd ion

Originally, Gd atoms are ferromagnetic but Gd^{3+} ions are paramagnetic. The paramagnetic behavior of Gd^{3+} ion originates from the seven unpaired 4f electrons. The seven unpaired inner 4f electrons are closely bound to the nucleus and effectively shielded by the outer closed shell electrons $5s^2$ $5p^6$ from the crystal field. Also, the doping of Gd^{3+} ions in REPs reduces the spatial overlap of the 4f orbitals and hence the magnetic moments are localized [2], [27-28]. As a result, the Gd-doped REPs demonstrate paramagnetic property upon applied magnetic field.

Table 1.1 Electronic configurations of rare-earth elements at ground state [1].

Atomic number	Ions	Corresponding element	4*f* electrons	S Σs	L Σl	J Σ(L+S)
21	Sc^{3+}	Ar		0	0	0
39	Y^{3+}	Kr		0	0	0
57	La^{3+}			0	0	0
58	Ce^{3+}	Xe	↑	1/2	3	5/2
59	Pr^{3+}	Xe	↑ ↑	1	5	4
60	Nd^{3+}	Xe	↑ ↑ ↑	3/2	6	9/2
61	Pm^{3+}	Xe	↑ ↑ ↑ ↑	2	6	4
62	Sm^{3+}	Xe	↑ ↑ ↑ ↑ ↑	5/2	5	5/2
63	Eu^{3+}	Xe	↑ ↑ ↑ ↑ ↑ ↑	3	3	0
64	Gd^{3+}	Xe	↑ ↑ ↑ ↑ ↑ ↑ ↑	7/2	0	7/2
65	Tb^{3+}	Xe	↑↓ ↑ ↑ ↑ ↑ ↑ ↑	3	3	6
66	Dy^{3+}	Xe	↑↓ ↑↓ ↑ ↑ ↑ ↑ ↑	5/2	5	15/2
67	Ho^{3+}	Xe	↑↓ ↑↓ ↑↓ ↑ ↑ ↑ ↑	2	6	8
68	Er^{3+}	Xe	↑↓ ↑↓ ↑↓ ↑↓ ↑ ↑ ↑	3/2	6	15/2
69	Tm^{3+}	Xe	↑↓ ↑↓ ↑↓ ↑↓ ↑↓ ↑ ↑	1	5	6
70	Yb^{3+}	Xe	↑↓ ↑↓ ↑↓ ↑↓ ↑↓ ↑↓ ↑	1/2	3	7/2
71	Lu^{3+}	Xe	↑↓ ↑↓ ↑↓ ↑↓ ↑↓ ↑↓ ↑↓	0	0	0

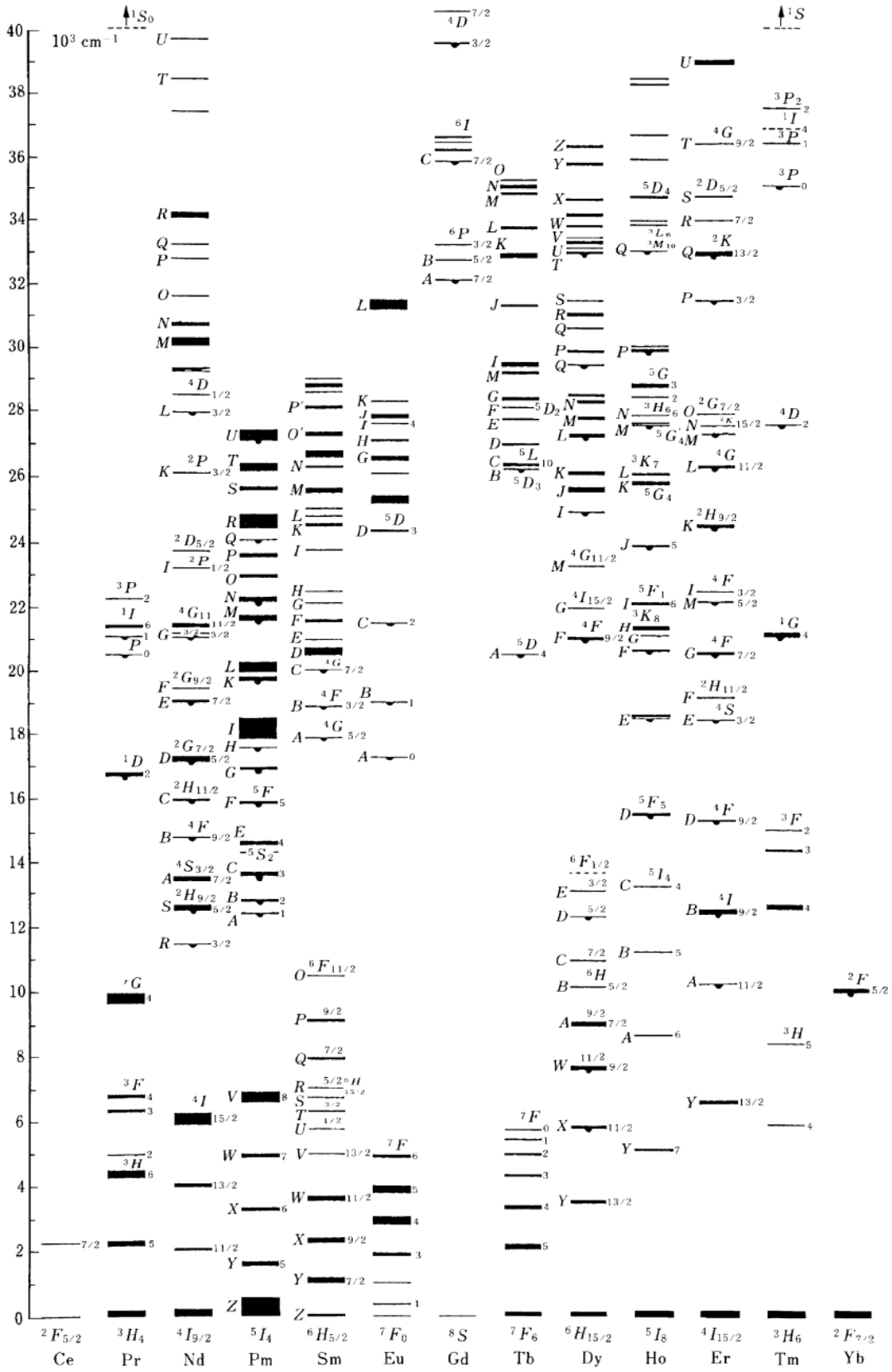

Figure 1.3 Energy levels of various rare-earth elements [1].

1.4 Current status of rare-earth doped phosphors

This work focuses on the development of new generation of REPs for bio-labeling applications. To date, there are numerous reports on the bio-labeling application of REPs. However, nano-sized REPs are preferred for bio-labeling because size of the molecule in targeted cells and tissues are usually from several to a few tens of nanometers [29-30]. Therefore, many synthesis strategies are developed to synthesize small-sized REPs. Apart from size, hydrophilic property, uniformity and physical properties are important considerations for tailoring nanoparticles for bio-labeling applications. Among various types of phosphors, RE doped upconversion nanoparticles (UCNPs) are reported extensively owing to their unique UC emission property. In order to optimize UCNPs, various reaction methods are developed by many groups, such as hydrothermal, thermal decomposition, fire combustion, and co-precipitation synthesis [5], [8], [20], [31-36]. Nowadays, hydrothermal, co-precipitation and thermal decomposition syntheses are the three popular reactions for synthesis of UCNPs [37].

1.4.1 Comparison of UCNPs with conventional phosphor for bio-labeling

Conventionally, organic dyes (ODs) [38-40] and quantum dots (QDs) [41-42] are common agents for fluorescent bio-labeling. They are excited by UV and thus prolonged exposure to these high energy sources results in DNA and cell damage. Moreover, the resultant signal to noise ratio (SNR) is low because high energy radiation causes considerable amount of autofluorescence from backgrounds due to the absorption of energy by biological tissues. This also implies a shallow penetrating depth [37]. To overcome these shortages, UCNPs are emerged as a class of fluorescent bio-

labeling material compared with traditional ODs and QDs. Firstly, the excitation wavelength range of UCNPs is broader than QDs and ODs, thus one can use different light sources for excitation (UV and NIR). Moreover, NIR enjoys advantages such as deep penetration, reduced photodamage and free of autofluorescence [8], [15], [37]. These features are pivotal for biological applications. Apart from excitation source, unlike QDs and ODs, UCNPs emit narrow bandwidth and multiple wavelengths. This unique emission characteristic of UCNPs can facilitate multi-channel tracking and imaging of biological samples without interference of channels. Among the three types of samples, UCNPs has long fluorescent lifetime, which is another advantage because long fluorescent lifetime can enable high resolution measurements to distinguish the UC signals from different nanoparticles and background. Finally, high photostability is a key merit for pro-long tracking and imaging of biological cells and tissues to observe temporal evolution of samples [43-46]. Above all, it is clear that UCNPs offers superior performance to the traditional fluorescent agents, such as QDs and ODs.

1.4.2 Biological applications of UCNPs

Recently, UCNPs have been emerged as a new class of material in therapy, luminescence assay and biological imaging. Photodynamic therapy (PDT) is capable of killing cancer cells by using the fact that some kinds of cancer cells are susceptible to attack of particular chemicals under red visible radiations. In addition, PDT is a non-intrusive, low-cost and increasingly effective treatment [47]. In addition, luminescence assay is divided into heterogeneous and homogenous assay [8], [37]. The former is achieved by using molecules which are biologically-functionalized and these molecules are conjugated to the UCNPs on a substrate. By recording the UC signal from the

UCNPs, the concentrations of the molecules can thus be measured. On the other hand, homogenous assay is based on a short ranged optical process called fluorescence resonance energy transfer (FRET) for measurement, for example Chen's group demonstrated the detection of avidin by amine-functionalized RE doped ZrO_2 sub-5 nm nanoparticles that showed a remarkable detection limit of 3.0 nM [46], [48].There is various bio-imaging techniques comprising fluorescent *in-vitro* and *in-vivo* imaging, diffuse optical tomography (DOT) and multi-modal imaging. *In-vitro* and *in-vivo* imaging and DOT utilize the UC emission property of UCNPs under the irradiation of NIR excitation. Human cervical cells, living nematode and nude mouse have been successfully imaged by UCNPs [49-52]. On the other hand, DOT can image the cross-section of the target under irradiation of NIR radiation [52]. Multi-modal imaging is the incorporation of two or more imaging modes within a single system. It is known that the paramagnetic property of Gd^{3+} ions enables UCNPs to be applied as magnetic resonance imaging (MRI) contrast agent [53-54]. Doping Gd^{3+} avoids the complexity of combining two kinds of imaging modes into a host material. In addition, doping offers a greater degree of control on synthesis of smaller particles for multi-modal imaging [46].

1.5 Motivation of research

Owing to the versatile ability of UCNPs in biological application, many strategies are developed to synthesize well-dispersed and water soluble UCNPs. Thermal decomposition of organic chemicals in coordinating oleic acid is a common approach to synthesize uniform UCNPs [53], [55-57]. However, this method requires high reaction temperature with purging of protective inert gases. Obviously, the as-synthesized products require further surface ligand engineering to change the

hydrophobic UCNPs to hydrophilic UCNPs for biological applications [37] and thus this increases the complexity and cost of synthesis procedures. Apart from synthesis method, sodium based host are frequently reported for bio-imaging purpose [17], [51] [58-60]. Unfortunately, as-synthesized sodium based UCNPs consist of cubic and hexagonal phases [61]. Therefore, additional physical and chemical modifications are needed to synthesize pure phase UCNPs. Moreover, the existing reports mainly focus on UC fluorescent imaging of cells. Fluorescent imaging offers good planar resolution but it is not able to provide 3D information of tissues. Besides, MRI and computed X-ray tomography (CT) imaging techniques are able to overcome the shortage of fluorescent imaging and they can image the 3D structure of soft tissues and organs [62]. As a result, it is important to explore simple and one-step synthesis for synthesizing hydrophilic UCNPs at low temperature. Additionally, further researches can focus on developing new UC host materials beyond sodium-based UCNPs for multi-modal imaging.

1.6 Scope of work

This work aims to develop new generation of UC materials for multi-modal bioimaging based on RE doped UCNPs.

This thesis consists of five chapters. In Chapter one, the fundamental mechanism for different types of UC process, physical properties of RE ions and the current status of RE doped phosphors are introduced.

In Chapter two, the hydrothermal synthesis is briefly introduced. Characterization instruments and techniques including PL and VSM are discussed in

detail while XRD, FTIR, TEM and SEM are briefly discussed.

In Chapter three, the phase and UC control of multi-functional $NaGdF_4$:Yb/Er upconversion phosphors (UCPs) is discussed. The $NaGdF_4$ UCPs demonstrate photo luminescence, cathodoluminescence and paramagnetic property. The underlying physical mechanisms of the phenomena are investigated.

In Chapter four, fluorescent imaging in HeLa cells was achieved by Ba_2LaF_7 UCNPs with a low concentration. The images are free of autofluorescence and MTT assay indicates that the Ba_2LaF_7 UCNPs has low toxicity. Moreover, a novel multi-modal bioprobe based on $BaGdF_5$:Yb/Er UCNPs with PEI and PEG surface modification is synthesized and studied. The $BaGdF_5$:Yb/Er UCNPs consist of pure cubic phase with average size less than 20 nm, which is an ideal average size for biological application. Moreover, *in-vitro* fluorescent imaging, MRI and *in-vivo* CT was demonstrated.

In Chapter five, conclusions and future work will be presented.

Chapter 2 Hydrothermal synthesis and characterizations

2.1 Hydrothermal synthesis

In Section 1.6, some of the phosphor synthesis methods have been reviewed and this work relied on a facile and one-step hydrothermal method to synthesize water dispersible phosphors. Hydrothermal is a synthesis technique that heat up a solvent under high pressure and temperature above the critical point of the system to enhance the solubility of solid. Therefore, it can speed up the reaction between solids. In addition, hydrothermal synthesis requires Teflon-lined container stored in a stainless steel container. The whole container is known as autoclave [15]. The popularity of this method is ascribed to the easy control of experimental parameters such as pH, reaction duration and temperature to yield different morphologies and shapes of nanostructures, such as nanorods, nano-arrays and nanospheres. However, the shortcomings of this method are poor yield, irregular shapes and size of UCNPs [3], [34], [63-67].

2.2 Characterizations

In this work, several characterization techniques are applied to characterize the as-synthesized phosphors. They include X-ray diffraction (XRD), scanning electron microscopy (SEM), transmission electron microscopy (TEM), Fourier transform infrared spectroscopy (FTIR), photoluminescence (PL), vibrating sample magnetometer (VSM) measurement, optical confocal microscopy and 3-(4,5-dimethylthiazol-2-yl)-2,5-diphenyltetrazolium bromide assay (MTT assay). Except for the confocal optical microscopy and MTT assay, the listed characterization techniques will be briefly introduced.

2.2.1 Photoluminescent measurement

The photoluminescence property of the as-synthesized phosphors is characterized by the photoluminscent spectrometer from Edinburgh Instruments Limited of model FLSP920. The exterior and interior structures of the system are shown in Fig. 2.1a and b.

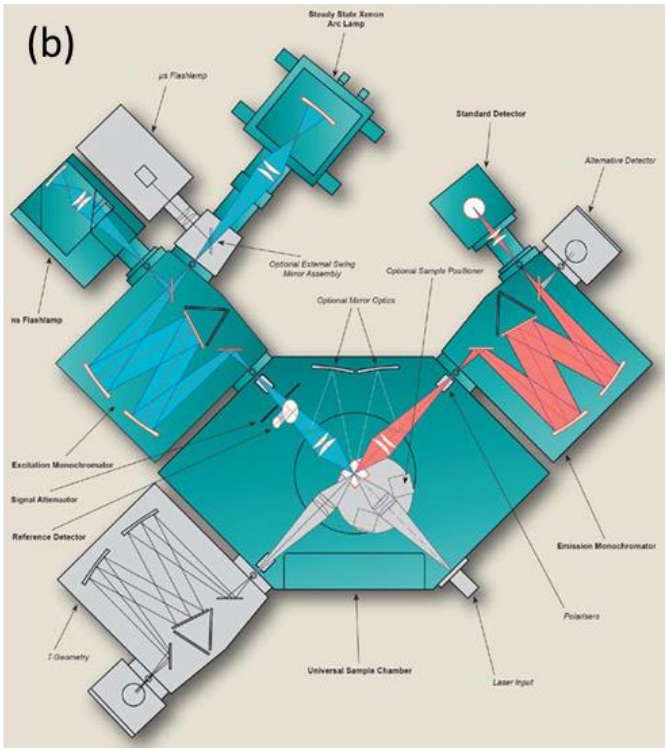

Figure 2.1 (a) Photograph of exterior structure of the photoluminscent spectrometer system and (b) interior structure of Edinburgh Instruments Limited (model FLSP920) **[68]**.

This PL system can be used to measure steady-state, temperature dependent and time-resolved photoluminescence property. A xenon lamp and various types of lasers ranging from ultraviolet to near infrared can be equipped as excitation source for PL measurements. Moreover, powder, liquid and thin film samples can be readily mounted on the testing platform by using quartz holders. There are two optical detectors, the visible light photomultiplier tube (PMT) and NIR PMT with detecting ranges from 200 to 900 nm and 400 nm to 1700 nm respectively.

2.2.2 Vibrating Sample Magnetometer

The vibrating sample magnetometer (VSM) examines the magnetic property of the as-synthesized phosphors and the structure of the commercial VSM from Lakeshore of model 7400 series - 7407 is shown in Fig. 2.2. This system consists of a pair of electromagnets to supply magnetic field to the mounted sample in the middle of the coil. At the same time, the sample vibrates with the driving frequency of the head drive. Owing to the change in magnetic flux of the sample, an electrical signal is detected by the machine and thus records the magnetization of the sample at different magnetic field.

Figure 2.2 An external view of Lakeshore vibrating sample magnetometer (model: 7400 series - 7407) **[69]**.

2.2.3 X-ray diffraction

The crystal phases of the phosphors are revealed by X-ray diffraction (XRD). Mainly, XRD technique is performed to reveal the crystalline planes, 2-theta angle and size of the phosphors. This is due to the fact that each material possesses a unique set of diffraction angles and planes. By acquiring the diffraction angles, the diffraction planes at each angle can be indexed to standard XRD patterns to evidence the crystallographic information of the materials.

2.2.4 Scanning electron microscopy and transmission electron microscopy

In order to investigate the morphologies, chemical composition, planar information and average size of the as-synthesized phosphors, scanning electron microcopy (SEM) and transmission electron microscopy (TEM) are used. SEM is suitable for characterizing phosphors with size of greater than 100 nm and this technique constructs a 3-dimentsional image of the phosphors. The scintillating detector of SEM collects secondary electrons due to bombardment of high energy electron on the sample surface for secondary electron imaging. While, TEM can characterize phosphors smaller than 100 nm and this technique is capable of investigating the average size, morphologies and phase of particles because of selected area electron diffraction and high resolution transmission electron microscopy. Both SEM and TEM can be equipped with energy dispersive X-ray system to reveal the chemical composition of a point or an area on the sample.

2.2.5 Fourier Transform Infrared spectroscopy

Fourier transform infrared spectroscopy (FTIR) is a spectroscopic method to evident the existence of organic ligands on the surface of the sample. The broadband light source of the machine will illuminate a combination of frequencies of optical radiation on the sample and detect the amount of absorbed light at each wavelength. Also, the spectrometer consists of a motorized mirror which blocks and transmits light periodically. At the mirror, the optical signal will interfere and reaches the optical detector. Then, the raw data are processed by the computer using Fourier transform algorithm to form spectrum.

Chapter 3 Phase and upconversion control of $NaGdF_4$:Yb/Er phosphor

3.1 Introduction

UC photoluminescence is a non-linear optical process facilitated by successive multi-absorption of two or more pumping photons to convert lower energy photons into higher energy photons [6], [70]. Owing to the ability of converting near-infrared (NIR) radiation to visible light, RE doped UCNPs offer advantages such as minimized photo-damage, high penetration depth and low background fluorescence [71-72]. Differing from conventional fluorescent phosphors including organic dyes and quantum dots [73-74], RE doped UCNPs are excited by NIR to emit visible emission. Therefore, RE doped UCNPs have demonstrated promising applications in biological fluorescent labeling, flat-panel displays and light sources [17-18], [20], [62], [75-76]. In recent years, many UC host materials including oxides and fluorides have been developed because of their unique luminescent property [77-78]. Among them, $NaYF_4$:Yb/Er has been regarded as the most efficient host material for UC emission because of its high UC luminescent efficiency [20], [33], [79]. However, literature data indicated that the as-synthesized $NaYF_4$:Yb/Er nanocrystals consist of α- and β- $NaYF_4$:Yb/Er. Moreover, reports found that the β-$NaYF_4$:Yb/Er exhibits an order of UC emission intensity enhancement relative to its α phase counterpart [23]. Apart from the phase issue, the ability to tune multi-color UC emission wavelength is important to applications, such as field-emission display (FED), solid state lasers and light sources. In principle, the tailoring of UC emission can be achieved by rational choice of host/activator material

and dopant concentrations [24]. However, the presence of high concentration and multiple types of RE dopants may lead to high cross relaxation and energy loss [80]. As a result, tuning multi-color UC emission and single β phase have become challenges for advance.

Recently, an annealing strategy to transform mixture of α- and β-$NaGdF_4$:Yb/Er into pure β-$NaGdF_4$:Yb/Er at 700 ^oC and the UC emission intensity of β-$NaGdF_4$:Yb/Er is enhanced at 600 ^oC [61]. Unfortunately, high temperature results in detrimental aggregation of nanoparticles. On the other hand, Liu's group developed a strategy for simultaneous phase and emission tuning for UCNPs through Gd^{3+} doping method and controlling Gd^{3+} sub-lattice mediated energy migration through a well-defined core-shell structure [9], [81]. Later on, the former technique was applied in the development of other RE-based phosphors, such as $NaLuF_4$ which exhibits high dispersibility and intense UC luminescence property [82]. Apart from modifying dopant concentrations and host/activator combinations, surface modification by using organic ligand is a common approach in tuning UC emission and single β phase UCNPs. By varying the molar ratio of octadecylamine and oleamide, UC emission with different red/green ratio was observed. Meanwhile, the resultant pure β-$NaYF_4$:Yb/Er UC phosphors have regular shape and high dispersibility [83]. However, this method suffers from high reaction temperature and the use of an inert gas medium. Although many works have been done on the phase and emission tuning of UC phosphors, it is still a challenge to develop a simple and cost effective protocol to tune single β phase and UC emission of UC phosphors. Besides, due to the large magnetic moment of Gd^{3+}, the UC phosphors containing Gd^{3+} present paramagnetic behavior and can be used as magnetic resonance

imaging (MRI) agent [84-86]. Moreover, Lin's group demonstrated cathodoluminescence (CL) property of $GdBO_3$:Eu and $GdBO_3$:Tb under the irradiation of low-voltage electron beam [87]. However, there are only limited reports on the CL property of Re doped $NaGdF_4$ host material.

In this part, tunable UC emission color and single β phase of multifunctional $NaGdF_4$:Yb/Er phosphor with fixed composition of host/activator are synthesized by a facile and one-pot hydrothermal method using ethylene glycol (EG) as reaction medium. Phase and different red/green ratios (RGR) can be tuned simply through surface modification using fixed amount of 3-Mercaptopropionic acid (3MPA), polyethylene glycol (PEG) and polyethylenimine (PEI). The physical mechanism underlying the tunable luminescence is discussed. Moreover, the magnetic and CL properties are investigated. Our approach provides an alternative pathway for rational phase and UC emission tuning. Therefore, these multifunctional phosphors have high potential in FEDs, light sources and solid state lasing applications.

3.2 Experimental

3.2.1 Hydrothermal synthesis of $NaGdF_4$:Yb/Er phosphor

RE nitrate $LnN_3O_9•6H_2O$ (Ln = Gd, Yb and Er) of purity 99.9% trace metal basis, 3-Mercaptopropionic acid (3MPA, 99 %+) and branched polyethylenimine (PEI, molecular weight = 25 kDa) were obtained from Sigma-Aldrich Co. Ltd. Ethylene glycol (EG, 99 %) was obtained from International Laboratory, USA. Polyethylene glycol (PEG, molecular weight = 6 kDa) and sodium fluoride powder (Analytical grade) were purchased from Sinopharm Chemical Reagent Co., China. All of these materials were used as received without further purifications. The RE nitrates were dissolved in de-ionized water to form 0.1 M $Gd(NO_3)_3$, $Yb(NO_3)_3$ and 0.05 M $Er(NO_3)_3$ solutions.

The phosphors were synthesized by a one-pot hydrothermal method [86], [88] at 200 ^oC for 20 h with surface modifier S (S = 0.5 g PEG/3MPA/PEI). Typically, total molar amount of RE dopants is 1 mmol with proportion of Gd:Yb:Er as 80:18:2. 2.1 g of NaF was dissolved in 50 ml of de-ionized water to produce a 1M NaF solution as sodium and fluorine source. The molar ratio of F^-/Re^{3+} was kept at 5 mmol. Firstly, respective amount of S was dissolved in 20 ml ethylene glycol (EG). After that, 1 mmol of RE dopants and 5 mmol of NaF were added to the above mixture under vigorous stirring for 1 h until semi-transparent colloidal solution is formed. Finally, the as-obtained solution was transferred to a Telfon-lined autoclave for hydrothermal reaction at 200 ^oC for 20 h. Then, the autoclave was allowed to cool down to room temperature naturally and separated from the reaction mixture by centrifugation using ethanol and de-ionized water.

3.2.2 Characterizations

The shape of as-prepared 3MPA, PEG and PEI modified phosphors were characterized by scanning electron microscopy (SEM) (JSM-6335F JEOL, Japan) with accelerating voltage of 8 kV. The crystal phase compositions of the synthesized phosphors were recorded by powder XRD using Rigaku smart lab 9 kW (Rigaku, Japan) with Cu K_α radiation (λ = 1.5406 Å). Fourier transform infrared spectrometry (FTIR) analysis was carried out using Magna 760 spectrometer E. S. P. (Nicolet, Thermo Scientific, USA). The UC spectra were recorded using an FLS920P Edinburgh Analytical Instrument apparatus equipped with an external 980 nm diode laser (MDL-980 nm, 2 W) as the excitation source. Low voltage CL spectra were obtained using a RELIOTRON III CL instrument. The spectra data were collected using an Ocean Optics USB4000 charge-coupled device spectrometer. The magnetization of phosphors as a function of the applied magnetic field ranging from -20 to 20 kOe was measured using a Lakeshore 7410 vibrating sample magnetometer. All measurements were performed at room temperature.

3.3 Results and discussion

3.3.1 Structural property

Phase and structure of 3MPA, PEG and PEI modified phosphors are recorded by XRD as shown in Fig. 3.1. In Fig. 3.1c, the PEG modified phosphors show that the diffracted peaks are in good agreement with the standard XRD pattern of β-$NaGdF_4$ (JSPDF No: 27-0699), which confirms that the PEG modified $NaGdF_4$ phosphors possess hexagonal phase structure with negligible amount of α-$NaGdF_4$. However, under the same experimental conditions, the diffracted peaks of 3MPA and PEI modified phosphors in Fig. 3.1a and b consist of mixture of cubic and hexagonal phases. Moreover, the relative peak intensity of α (denoted by rhombus) to β phase in PEI modified phosphors is higher than that of 3MPA and PEG modified phosphors. As a result, the portion of α-$NaGdF_4$ was reduced by using the surface modifier from PEI to 3MPA. Deduced from the XRD data, the addition of 3MPA and PEI favors the formation of α-$NaGdF_4$, in which PEI exhibited a stronger effect on the formation of α-$NaGdF_4$ compared to 3MPA.

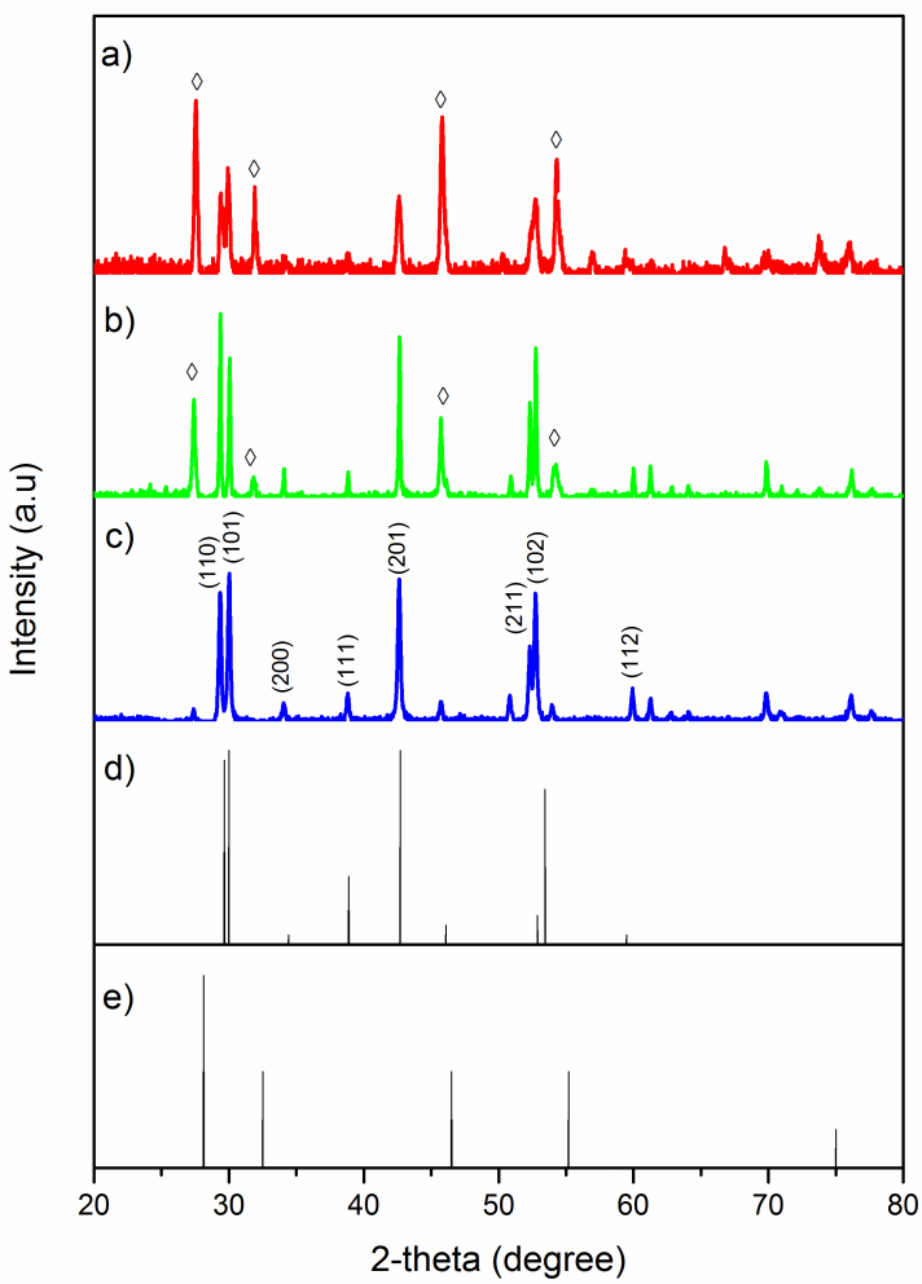

Figure 3.1 XRD patterns of the (a) PEI modified, (b) 3MPA and (c) PEG modified $NaGdF_4$:Yb/Er phosphors, (d) β-$NaGdF_4$ (JCPDS 27-0699) and (e) α-$NaGdF_4$ (JCPDS 27-0697). Rhombuses attached at diffracted peaks denote α-$NaGdF_4$.

To reveal the morphology and size of the phosphors, the as-synthesized 3MPA, PEG and PEI modified phosphors were further observed by SEM. Fig. 3.2a, b and c show the morphology of the three types of as-synthesized phosphors. From Fig. 3.2c, PEG modified phosphors present spherical shape. With the addition of 3MPA and PEI, the phosphors consist of mixed phases with both spherical and rod-like shapes. By correlating the respective XRD spectra and SEM images of phosphors, the phase, shape and size of these samples can be readily tuned simply by adding different surface modification agents, such as 3MPA, PEI and PEG. It is known that reaction time and temperature play important role in formation of phase and shape of phosphors. Here, reaction time and temperature factors are eliminated by fixing reaction conditions at 20 h and 200 ^{o}C. As a result, capping ligand is the sole factor to affect the formation of phase and shape. As far as we know, selective adhesion of capping ligand onto specific crystal planes is critical in the epitaxial growth of nanocrystals. Consequently, the growth of long rods is observed during crystallization of phosphors. Yet, the existence of spherical particles is attributed to a ligand-concentration kinetic effect. In the early stage of reaction, the concentration of ligands is high and thus selective adhesion is the dominant factor. However, PEI, 3MPA and PEG are consumed in different rates. Eventually, intra-particle movement of atoms occurs due to complete consumption of ligands. Atoms tend to move from single growing facet to other facets and thus a transition from rods to spherical particles is observed. To the best of our knowledge, the impact of different organic surface modifications on the formation of α- and β-UC phosphors has not been reported. Differing from the reported methods of annealing, RE doping phase tuning and energy migrating method [9], [61], [81], the addition of surface

modifier here can simultaneously control the crystal phase, shape and size of UCNPs.

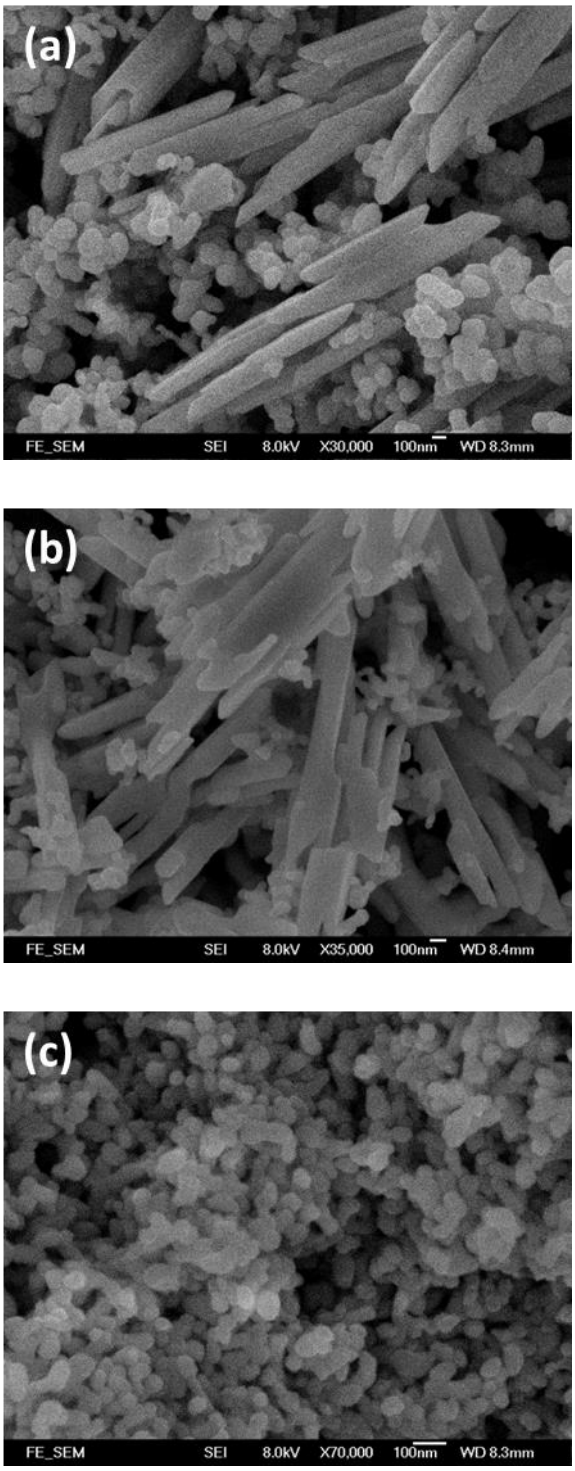

Figure 3.2 FE-SEM image of the (a) PEI modified, (b) 3MPA modified and (c) PEG modified $NaGdF_4$:Yb/Er phosphors.

3.3.2 Surface group characterization

The respective FTIR spectra of 3MPA, PEG and PEI modified phosphors are shown in Fig 3.3a. As shown in Fig. 3.3a, the absorption band at about 3445 cm^{-1} is due to the stretching vibration of O-H group. On the other hand, the weak absorption band at about 2938 cm^{-1} is attributed to the asymmetrical vibration modes of $-CH_2$ group. Originally, the wavenumber at 2569 cm^{-1} is present in the FTIR spectrum of pure 3MPA. However, this absorption is not present in Fig. 3.3a. It suggests that the –SH group at the end of 3MPA molecule is bonded on the surface of phosphors because of the strong binding ability of mercapto group and metal ions. Moreover, the peak at 1645 cm^{-1} is attributed to the asymmetrical stretching vibration modes of C=O group while the peaks at about 1409 and 1268 cm^{-1} are due to in-plane vibration of C-OH and stretching vibration of C-O groups of 3MPA, respectively [88]. From the above analysis, we deduce the successful capping of 3MPA on phosphors. In Fig. 3.3b, the broad absorption band at 3445 cm^{-1} is attributed to bond stretching of O-H. Moreover, the absorption peaks at 1632 and around 1114 cm^{-1} correspond to the methylene scissoring and C-O-C bond vibrations. From the results, we could confirm the capping of PEG on the surface of phosphors [89]. For PEI modified phosphors, Fig. 3.3c shows an absorption peak at 3451 cm^{-1} corresponding to the bond stretching of O-H and N-H bondings. In addition, the transmission peaks at 1628, 1564 and 1414 cm^{-1} are attributed to the bond vibration of C-N, bending modes of primary and secondary amine respectively, indicating the successful capping of PEI on the surface of phosphors [60].

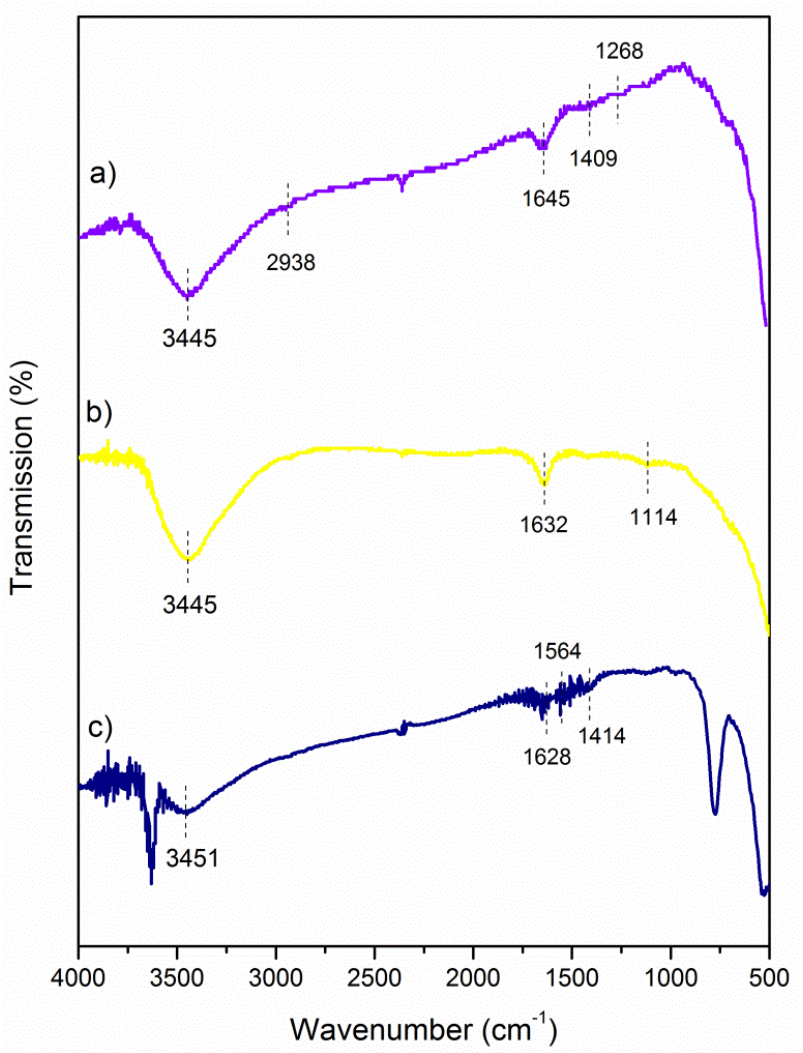

Figure 3.3 FTIR spectra of the (a) 0.5 g 3MPA, (b) 0.5 g 6 kDa PEG and (c) 0.5 g branched 25 kDa PEI modified $NaGdF_4$:Yb/Er phosphors.

3.3.3 Upconversion luminescence

The UC emission spectra of 3MPA, PEG and PEI modified phosphors are investigated under the excitation of 980 nm laser diode. The UC emission spectra of the PEG, 3MPA and PEI modified phosphors are shown in Fig. 3.4a, b and c. When the phosphors are dispersed in DI water to form colloidal solutions with concentration of 2.5 mg ml^{-1}, three kinds of eye-visible emissions of green, yellowish green and red resulting from PEG, 3MPA and PEI modified phosphors are shown in Fig. 3.4e, f and g,

respectively. All emission spectra are recorded under the same laser power and the emission intensity of PEG modified phosphors is the strongest among the three types of phosphors. This observation is consistent with the accepted fact that β-UC phosphor usually exhibits stronger emission intensities than α-UC one. Moreover, Fig. 3.4a shows three major emission bands with peak emission wavelengths of 521, 554 and 660 nm, which are attributed to the $^2H_{11/2} \rightarrow {}^4I_{15/2}$, $^4S_{3/2} \rightarrow {}^4I_{15/2}$, and $^4F_{9/2} \rightarrow {}^4I_{15/2}$ transitions of Er^{3+}, respectively [37], [90-91]. According to the energy level diagram shown in Fig. 3.4h, the UC process is initiated by the Yb^{3+} sensitizer ions and subsequent energy transfer to activator Er^{3+} leads to pumping of Er^{3+} to higher energy levels [71]. Then, non-radiative relaxations followed by further downward transitions to lower energy levels give rise to three visible emission bands. Interestingly, different red to green ratio (RGR) is observed in PEG, 3MPA and PEI modified phosphors. The quenching of two emission bands with peak wavelengths 521 and 544 nm gives rise to different RGRs as shown in Fig. 3.4d. It indicates that the decrease in green components in 3MPA and PEI modified phosphors results in yellowish green and red emissions. Different RGRs are attributed to the presence of different surface groups such as hydroxyl (-OH), mercapto (-SH) and amino ($-NH_2$) group on the surface of PEG, 3MPA and PEI modified phosphors. NH_2 groups capped on the surface of PEI modified phosphors exerts a higher green emission quenching effect than -OH and -SH groups. The quenching effect can be originated from the simplified energy level diagram in Fig. 4h in which the presence of -OH and $-NH_2$ groups favor the non-radiative relaxations at low-lying energy level, i.e. $^2H_{11/2} \rightarrow {}^4F_{9/2}$. Eventually, the green emission band is quenched and hence the emission color is changed from green, yellowish-green and finally to red. In

addition to the presence of surface ligands that change the RGRs, the ligand-induced structural and morphological change also contribute to the difference in observed RGRs. From the XRD, PL and RGR data, PEG-modified $NaGdF_4$:Yb/Er (pure hexagonal) emits intense green emission while the UC emission spectrum of 3MPA and PEI-modified $NaGdF_4$:Yb/Er in Fig. 3.4b and c consists of fewer green wavelength component than PEG-modified $NaGdF_4$:Yb/Er and therefore it is reasonable to deduce the hexagonal phase $NaGdF_4$ favors green emission component while the cubic phase favors red emission component. Typically, the luminescence lifetime and quantum yield of RE based UC phosphors are in magnitude of several milliseconds and in a range of 0.005 to 0.3 depending on size [92-93]. To further reveal the UC mechanism, power dependence study was performed on PEG-modified $NaGdF_4$:Yb/Er phosphor for the three emission peaks observed in Fig. 3.4a, b and c. The result is consistent with the power law for upconversion, $I_{UC} \alpha I^n_{IR}$. [62], [86], where n is the number of pump photons required to populate the upper emitting level and its value can be obtained from the slope of the line in the plot of log I_{UC} versus log I_{IR}. Fig. 3.4i shows the log-log plots of the UC emission intensity as a function of excitation infrared radiation power of the green and red emissions in the $NaGdF_4$:Yb/Er phosphor. The slopes of the linear fits for the green and red emissions at 521, 544 and 660 nm are 1.88 1.94 and 1.87, respectively, indicating a two photon process is required by both green and red UC emissions. As a result, this facile UC tuning technique is an advantage for controlling emission wavelength of phosphors for displays.

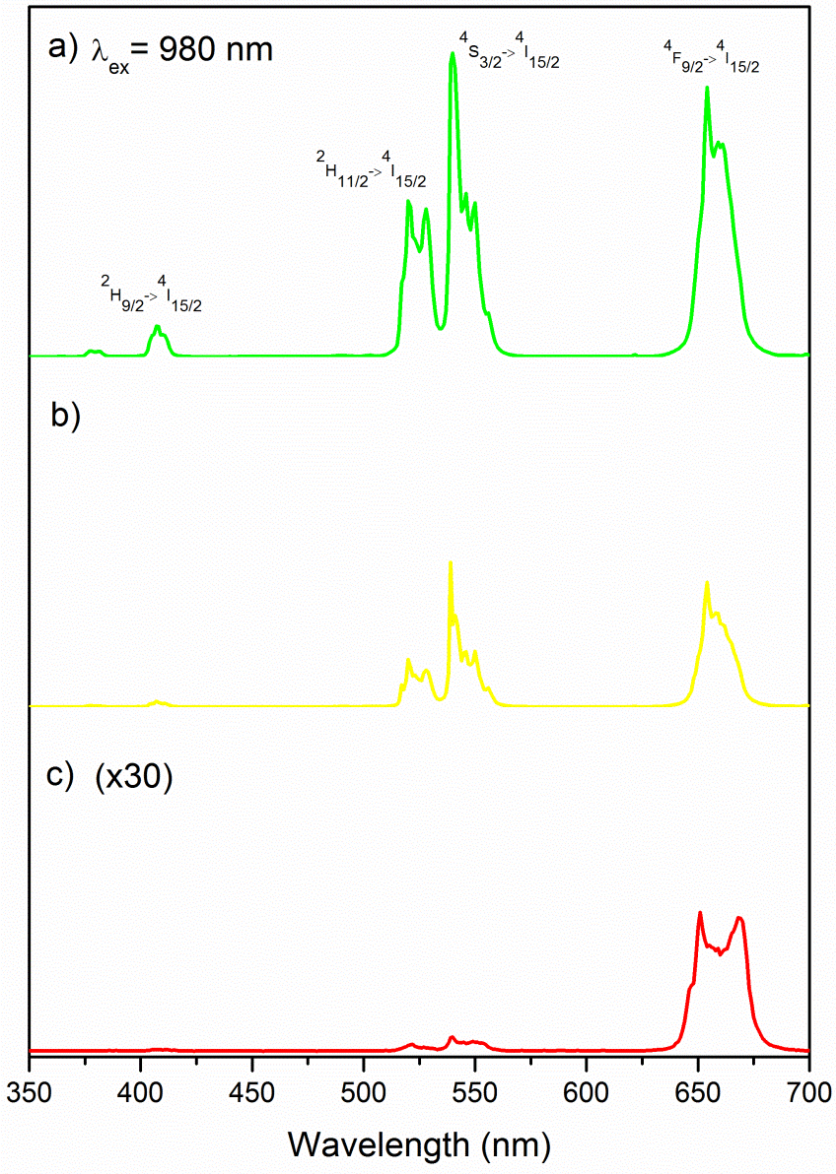
a) λex = 980 nm
4S3/2-> 4I15/2
4F9/2-> 4I15/2
2H11/2-> 4I15/2
2H9/2-> 4I15/2
b)
c) (x30)
350
400
450
500
550
600
650
700
Wavelength (nm)

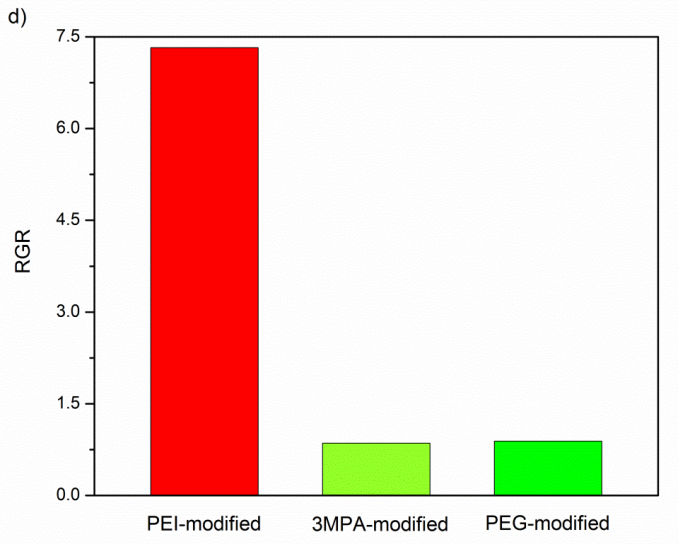
d)
RGR
7.5
6.0
4.5
3.0
1.5
0.0
PEI-modified
3MPA-modified
PEG-modified

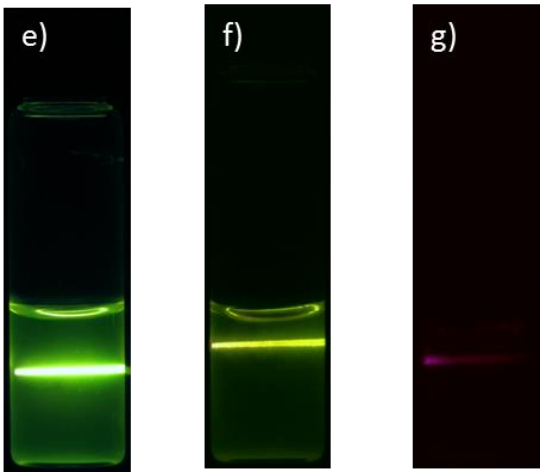

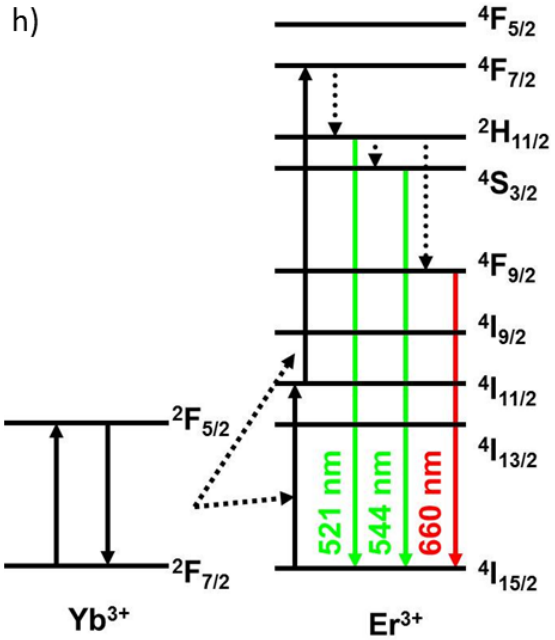

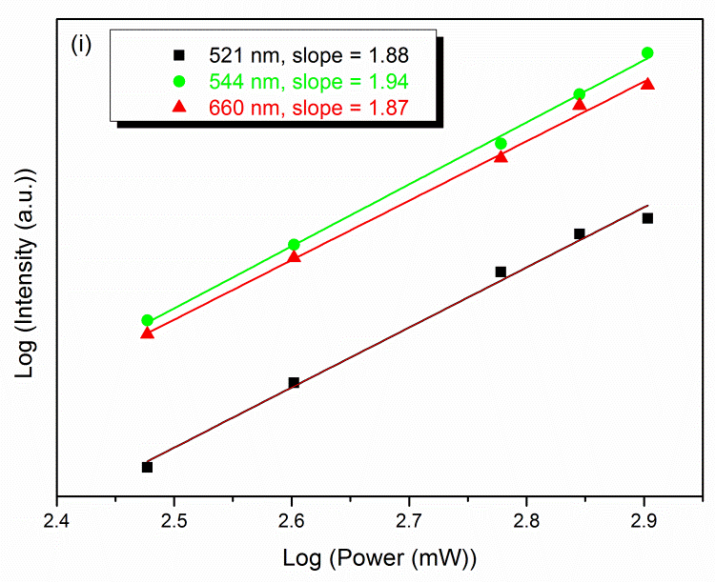

Figure 3.4 UC luminescence spectra of (a) PEG modified, (b) 3MPA modified and (c) PEI modified $NaGdF_4$:Yb/Er phosphors under 980 nm continuous wave (CW) laser excitation, (d) red to green ratio (RGR) of PEG, 3MPA and PEI modified phosphors. Emission color of (e) PEG modified, (f) 3MPA modified and (g) PEI modified phosphors dispersed in water with a concentration of 2.5 mg ml^{-1}. (h) Simplified energy

level diagram of Yb^{3+}/Er^{3+} doped system showing the upconversion process and emission wavelengths. (i) Log-Log plots of the UC luminescence intensities versus excitation power of PEG-modified $NaGdF_4$:Yb/Er phosphor.

3.3.4 Cathodoluminescence

Apart from PL property, the phosphor can also be excited by low voltage electron beam (~3.5 kV). Fig. 3.5a shows the CL spectrum of PEG modified phosphors irradiated by electron beam with 3.5 kV and a tube current of 1.396 mA. As shown in the inset of Fig. 3.5a, the intense and eye-visible green emission can be observed from the PEG modified phosphors. The obtained CL spectrum is similar to PL spectrum in Fig. 3.4a. It is known that electron beam has a greater penetration depth and thus the electrons can penetrate into the phosphors to excite the Er^{3+} to give visible emission. Moreover, the current and voltage dependent CL intensity measurement was carried out by adjusting the vacuum condition and the measured results are shown in Fig. 3.5b and c respectively. The CL intensity for PEG modified phosphors exhibits an almost linear relationship with the accelerating voltage ranging from 2.4 to 3.5 kV. These results can be explained by the equation regarding the electron penetration depth:

$$L = 250\left(\frac{A}{\rho}\right)\left(\frac{E}{Z^{1/2}}\right)^{n}$$

where, n = 1.2/(1-0.29Z), A the atomic or molecular weight of the material, ρ the bulk density, Z the atomic number or the number of electrons per molecule in the case compounds and E is the accelerating voltage of electron beam [94]. It is known that the

penetration depth of an electron beam into a particular specimen is dependent on the value of excitation voltage [61]. As a result, more Er^{3+} are being excited due to increased interaction volume of electrons and phosphors, subsequently contributes to intense emission peaks. Also, the CL intensities increase with filament current from 0.7 to 1.3 mA. Therefore, the phosphors with intensive green CL emission may be suitable to be used as phosphor for FED devices.

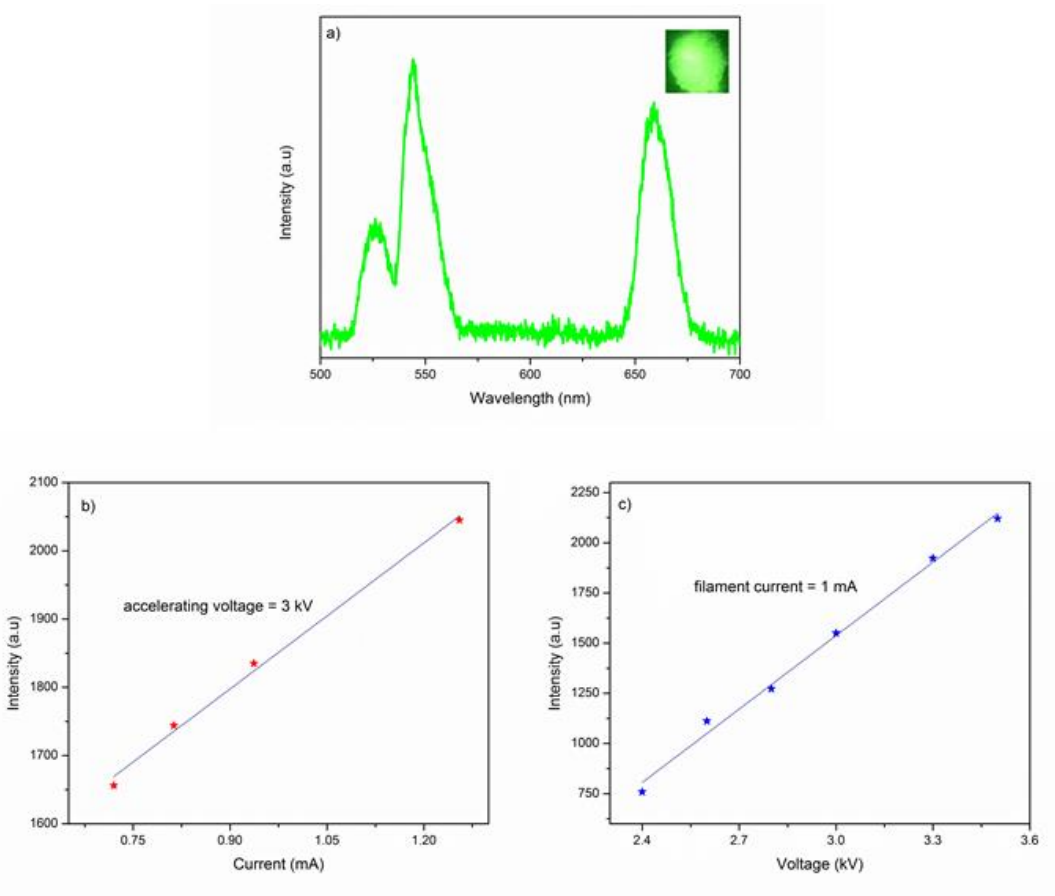

Figure 3.5 (a) Cathodoluminescence (CL) spectrum of PEG modified $NaGdF_4$:Yb/Er phosphors irradiated by low voltage electron beam at 3.5 kV with a tube current of 1.396 mA (Inset figure showing green emission), (b) current dependent CL intensity under irradiation of electron beam at 3.0 kV, (c) voltage dependent CL intensity by maintaining tube current at 1 mA of PEG modified $NaGdF_4$:Yb/Er phosphors@ 544 nm.

3.3.5 Magnetic property

In addition to UC and CL luminescence property, the magnetic property of the as-synthesized phosphors is also measured. As demonstrated in Fig. 3.6, the PEG modified phosphors possess paramagnetic property at room temperature. Existence of paramagnetic property is due to the seven unpaired inner electrons in the 4f subshell strongly bounded by the nucleus and effectively shielded by the outer closed-shell $5s^2 5p^6$ electrons from the crystal field [61]. As a result, localized and non-interacting magnetic moment of Gd^{3+} in phosphors gives rise to paramagnetism. The magnetic mass susceptibility of PEG modified phosphors are measured to be 8.36×10^{-5} emu/g Oe at 298 k. This value is similar to the reported value of GdF_3:Eu (0.94×10^{-4} emu/g Oe) and $KGdF_4$:Yb/Tm (3.99×10^{-5} emu/g Oe) [2], [95]. Moreover, a peak magnetization at 20 kOe is found to be 1.538 emu/g and this value is close to the reported values for bio-separation.

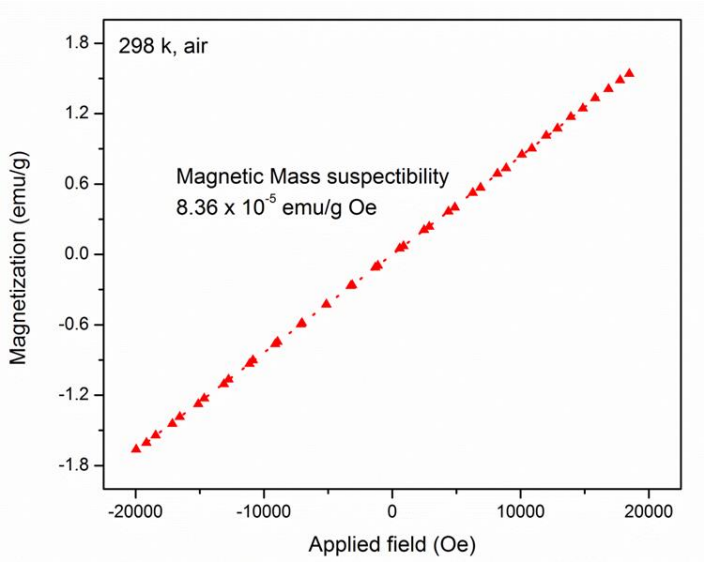

Figure 3.6 Magnetization (emu/g) as a function of the applied magnetic field (Oe) of PEG modified $NaGdF_4$:Yb/Er phosphors.

Chapter 4 Barium-based UCNPs for multi-modal biological imaging

In this chapter, PEI-modified Ba_2LaF_7:Yb/Er UCNPs with no phase transition were prepared by hydrothermal method. The as-synthesized UCNPs have small average size (< 20 nm) suitable for bioimaging. The UCNPs are able to demonstrate UC fluorescent imaging at low concentration (100 μg ml^{-1}) in HeLa cells. In addition, $BaGdF_5$:Yb/Er UCNPs was synthesized by similar method. The structural, chemical composition, phase, photoluminescence and magnetic properties were studied. The surface of $BaGdF_5$ was capped with PEI and PEG respectively to enhance uptake in HeLa cells and living animal. In contrast to high temperature method, such as thermal decomposition, $BaGdF_5$:Yb/Er was synthesized by a low temperature method which reduce the cost for synthesis. The as-synthesized $BaGdF_5$ UCNPs possess pure cubic phase structure and hydrophilic property which do not require further surface and phase transition treatment for biological application. MTT assay indicates that this host material has low cytotoxicity and high cell viability can be maintained at high UCNPs concentration. Importantly, the PEI and PEG modified $BaGdF_5$ demonstrate *in-vitro* UC fluorescent, magnetic resonance imaging (MRI) and *in-vivo* computed X-ray tomography (CT) in a single system without complicated synthesis and treatments. Thus, the respective strengths of the particular imaging technique compensate the weakness of the other technique. As a result, the barium-based UCNPs have very high potential for bio-imaging applications.

4.1 *In-vitro* fluorescent imaging by Ba_2LaF_7:Yb/Er UCNPs

4.1.1 Introduction

UCNPs have been studied extensively and applied in fluorescent bio-imaging because of their unique UC properties [96-97]. Unlike conventional bio-imaging agents, UCNPs are excited by NIR radiation which possesses deep tissue penetration. Contrary to traditional fluorescent bio-imaging agents, UCNPs have no autofluorescence, low toxicity, high photostability and large anti-stoke shift [15], [46], [98-99]. The common UC host materials are RE doped fluorides with formula ALnF (A= Na, Li, Ba or K) and this formula has been regarded as a promising host formula because this structure has low phonon energy and hence enhancing radiative transition probability and efficiency [12]. Among the host materials, sodium-based UCNPs have been studied extensively for numerous biological applications, such as detection of DNA, Avidin, Glutathione and fluorescent *in-vitro* and *in-vivo* bioimaging [37], [48], [100-105]. Owing to the size range of the targeted biomolecules in cells and tissues is usually from several to a few tens of nanometers, small-sized fluorescent probes should be relatively small in size so that the probe can be compatible with the targeted cell [27-28]. However, the size of the reported UCNPs (20–60 nm) is not optimal for their use as bioimaging probes. As a result, much effort has been focused on the synthesis of small-sized (less than 20 nm) UCNPs for bioimaging applications.

Recently, there was report about the synthesis of ultra-small sized Ba_2LaF_7 UCNPs based on an oleic-acid assisted solvothermal method [106]. The as-synthesized UCNPs demonstrated intense UC emission with a sub-10 nm size. What deserves to be mentioned is the comparison on UC emission intensity of small-sized Ba_2LaF_7 and

cubic phase $NaYF_4$ UCNPs. $NaYF_4$ is a common host material that is able to emit intense UC emission. It was found that Ba_2LaF_7 UCNPs emit stronger UC emission than cubic phase $NaYF_4$ UCNPs under the same conditions [106] .Unfortunately, the as-synthesized small UCNPs are hydrophobic which limited their biomedical applications. Obviously, further surface modifications are needed to enable hydrophilic property. Hence, it is worth to develop a simple method to synthesize UCNPs with hydrophilic and excellent UC property.

In this chapter, a one-step hydrothermal synthesis and UC fluorescent *in-vitro* imaging of PEI-modified Ba_2LaF_7 UCNPs is reported. The as-synthesized products have small average size of about 18 nm and pure cubic phase. Intense green UC emission was observed from a Ba_2LaF_7:Yb/Er colloidal solution (1 wt%) under 980 nm laser excitation. Also, the fluorescent imaging in HeLa cells and MTT assay suggests that this host is capable of presenting no autoflourescence imaging with low cytotoxicity.

4.1.2 Experimental

4.1.2.1 Hydrothermal synthesis of Ba_2LaF_7:Yb/Er UCNPs

$Ln(NO_3)_3 \cdot 6H_2O$ (Ln = La, Yb, Er) was purchased from Aldrich and dissolved in de-ionized water (DI-water) to form solutions with concentrations of 0.5 M and 0.1 M. Ethylene glycol (EG, 99%) and branched polyethylenimine (PEI, 25 kDa) were purchased from Sigma-Aldrich. NH_4F (99.99%) and $BaCl_2$ (99.99%) were obtained from Sinopharm Chemical Reagent Co., China. All of these chemicals were used as received without further purifications.

Water-soluble and PEI-modified Ba_2LaF_7:Yb/Er UCNPs with high

monodispersity were synthesized by a modified one-pot hydrothermal method (Fig. 4.1) [62] [86]. Typically, 1.0 g of PEI was added into 20 mL of EG containing 1 mmol of $La(NO_3)_3$ (0.5 M), $Yb(NO_3)_3$ (0.5 M) and $Er(NO_3)_3$ (0.1 M) with the molar ratio of 78 : 20 : 2 under vigorous stirring. Then, 1 mmol of $BaCl_2$ was added to the above solution. The mixture was stirred for 30 min to form a homogeneous solution. After that, 6 mmol of NH_4F in 10 mL of EG was added to the above mixture. The obtained mixture was agitated for another 30 min, and then transferred into a 50 mL stainless Teflon-lined autoclave and kept at 190 ^oC for 24 h. After the reaction, the system was naturally cooled down to room temperature. The prepared samples were separated by centrifugation, washed several times with ethanol and DI-water to remove other residual solvents, and finally dried in a vacuum at 70 ^oC for 24 h.

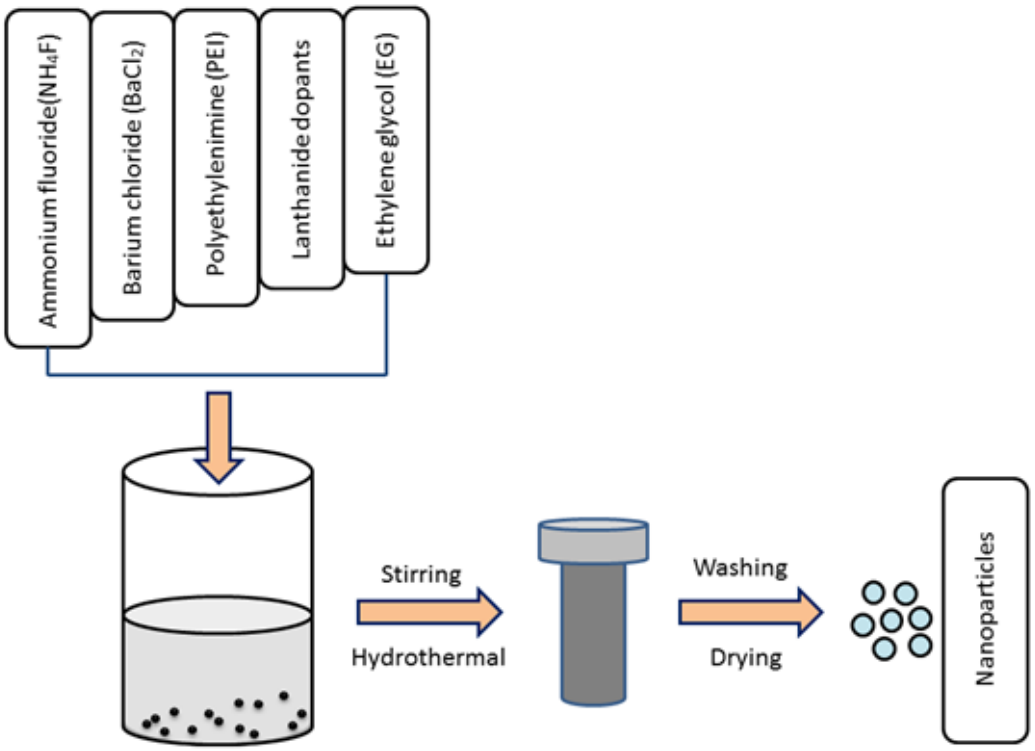

Figure 4.1 One-pot hydrothermal synthesis of PEI-modified Ba_2LaF_7 :Yb/Er UCNPs.

4.1.2.2 Characterizations

Powder X-ray diffraction (XRD) patterns of the as-prepared UCNPs were recorded using Rigaku smart lab 9 kW (Rigaku, Japan) with Cu K_α radiation (λ = 1.5406 Å) at 45 kV and 200 mA. The shape, size and structure of the as-prepared samples were characterized by using JEOL-2100F transmission electron microscopy (TEM) equipped with an Oxford Instrument EDS system, operating at 200 kV. Fourier transform infrared spectrum (FTIR) was recorded by a Magna 760 spectrometer E. S. P. (Nicolet). UC spectra were recorded using FLS920P Edinburgh analytical instrument apparatus equipped with a 980 nm diode laser as an excitation source.

Human cervical carcinoma HeLa cells were purchased from the American type Culture Collection (ATCC) (#CCL-185, ATCC, Manassas, VA, USA). The HeLa cells were grown in Dulbecco's Modified Eagle Medium (DMEM) supplemented with 10% fetal bovine serum (FBS) 1% penicillin and streptomycin at 37^oC and 5% CO_2. To apply Ba_2LaF_7:Yb/Er UCNPs for fluorescent imaging, HeLa cells were incubated in DMEM containing 100 μg mL^{-1} of PEI modified UCNPs at 37 ^oC for 24 h under 5% CO_2, and then washed with PBS sufficiently to remove excess UCNPs.

In order to test the suitability of the obtained PEI modified UCNPs as bioprobes, bioimaging of HeLa cells incubated with Ba_2LaF_7:Yb/Er UCNPs was performed on a commercial confocal laser scanning microscope, Leica TCS SP5, equipped with a Ti:Sapphire laser (Libra II, Coherent). The samples were excited by a 980 nm wavelength laser, and two visible UC emission channels were detected at green (500–600 nm) and red (600–700 nm) spectral regions.

The *in-vitro* cell viability was measured using 3-(4, 5-dimethylthiazol-2-yl)-2, 5

diphenyl-tetrazolium bromide (MTT) proliferation assay in HeLa cells. HeLa cells were seeded in a 96-well micro-plate (6000 cells per well) and pre-incubated at 37 ^{o}C under 5% CO_2 for 3 h. The cell culture medium in each well was then replaced by DMEM solutions containing PEI modified UCNPs with different concentrations. Subsequently, the cells were incubated for another 20 h in the incubator at 37 ^{o}C under 5% CO_2. After that, 10 mL of MTT (5 mg mL^{-1} in phosphate buffered saline solution) was added to each well and incubated for further 4 h at 37 ^{o}C under 5% CO_2. After the growth medium was removed, 200 mL of DMSO was added to each well and the cells sat overnight at room temperature to completely dissolve the formazan crystals. The absorbance at 570 nm was measured by Multiskan EX (Thermo Electron Corporation).

4.1.3 Results and discussion

4.1.3.1 Structural property

TEM is applied to reveal the morphology, size and shape of the as-synthesized Ba_2LaF_7:Yb/Er UCNPs. The UCNPs presented a spherical morphology with good monodispersity as shown in Fig. 4.2a and b. The corresponding selected area electron diffraction (SAED) pattern is shown in Fig. 4.2c in which the diffraction pattern suggests that the Ba_2LaF_7:Yb/Er UCNPs possess a simple cubic structure. To further investigate the UCNPs, high resolution TEM (HRTEM) of three NPs in Fig. 4.2d shows clear lattice fringes of the UCNPs. The measured d-spacing is 2.17 Å and this value was consistent with the spacing of the (220) plane of standard cubic phase Ba_2LaF_7 (2.15 Å). Therefore, the measurement confirmed the good crystallinity of the UCNPs. Moreover, the size distribution of the NPs in is shown in Fig. 4.2e, the average size of the NPs is

about 18 nm with a range of 13-24 nm. The average size of UCNPs is an ideal size for bioimaging applications. Moreover, X-ray diffraction (XRD) characterized the phase composition of Ba_2LaF_7:Yb/Er UCNPs under 45 kV and 200 mA X-ray irradiation (Fig. 4.2f) and the diffracted peaks are indexed to the standard diffraction pattern of cubic phase Ba_2LaF_7 (JCPDS: 48-0099). The diffraction peaks were well matched with the standard pattern with no impurity phases. As a result, the XRD matching agrees with the SAED pattern. In addition, owing to the substitution of La^{3+} ions by smaller Yb^{3+} ions, the diffracted peaks shift to higher angles. In fact, this observation is similar to that in the previous reported XRD of RE doped UCNPs [62], [106]. The above analysis proves that the one-pot hydrothermal synthesis iss able to produce pure cubic phase Ba_2LaF_7:Yb/Er UCNP s with high monodispersity.

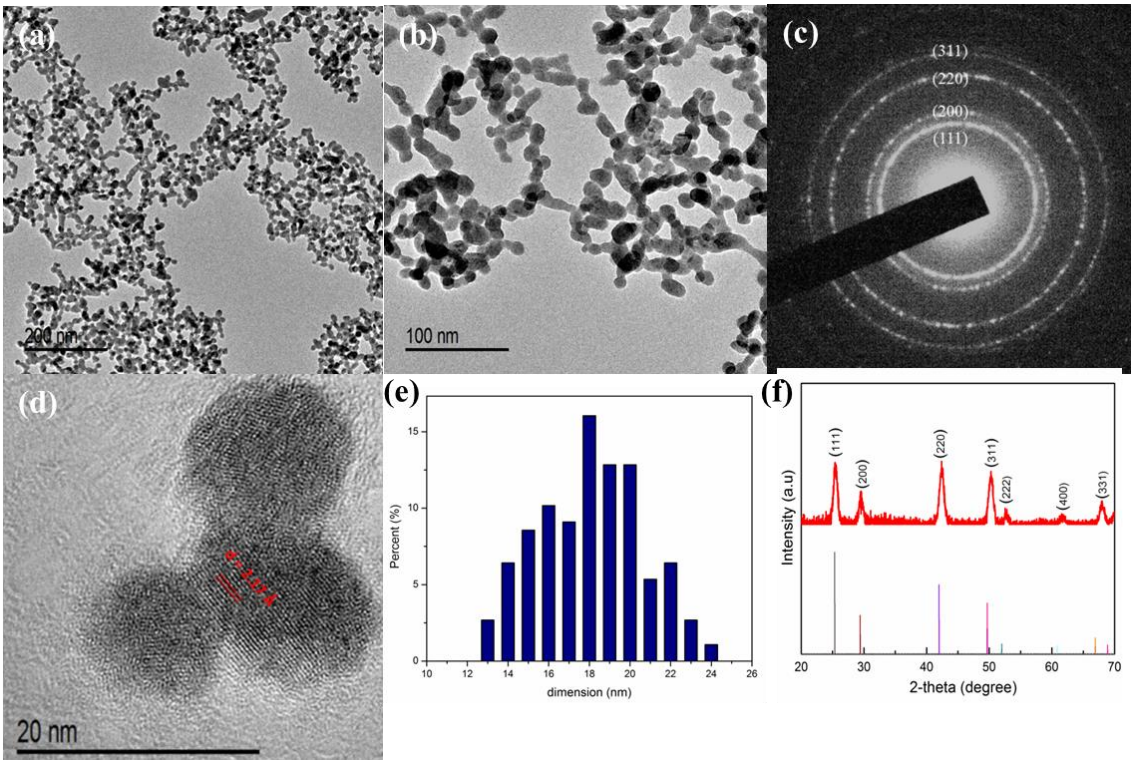

Figure 4.2 TEM and XRD results of the PEI modified Ba_2LaF_7:Yb/Er UCNPs: (a) low magnification TEM image, (b) high magnification TEM image, (c) SAED, (d) HRTEM

image of single particle, (e) histogram of the particle size distribution, (f) XRD pattern.

4.1.3.2 Upconversion photoluminescence

In bioimaging, the UCNPs were readily dispersed to form colloidal solution and excited by near infrared (NIR) radiation. However, a satisfactory signal to noise ratio (SNR) was important for clear observation of cells, therefore eye-visible and intense UC luminescence was one of the key to achieve the aim. Inset of Fig. 4.3 shows colloidal solution of as-prepared Ba_2LaF_7:Yb/Er UCNPs (1 wt%) emitting strong UC green color under irradiation of 980 nm laser. Three emission bands of Ba_2LaF_7:Yb/Er UCNPs centered at 521, 544, and 660 nm are located in Fig. 4.3. The manifestation of emission bands could be deduced from the simplified energy level diagram of Yb/Er system (Fig. 4.4). The green and red UC emissions are due to the electronic transitions, $^2H_{11/2}$ / $^4S_{3/2} \rightarrow {}^4I_{15/2}$ and $^4F_{9/2} \rightarrow {}^4I_{15/2}$ of Er^{3+} ion, respectively. Owing to the pumping by 980 nm laser, the Yb^{3+} and Er^{3+} ion are excited simultaneously to higher metastable state. Then, Yb^{3+} ion is pumped from $^2F_{7/2}$ to the first excited state $^2F_{5/2}$. Subsequent energy transfer from Yb^{3+} ion to the nearby Er^{3+} ion pumps the Er^{3+} ion from its ground state to $^4I_{11/2}$. Owing to the long lifetime of the metastable state of Er^{3+} ion, it could further absorb energy from Yb^{3+} ion and pumps to $^4F_{7/2}$. After that, the excited Er^{3+} ion relaxed non-radiatively to $^2H_{11/2}$ / $^4S_{3/2}$/$^4F_{9/2}$. Finally, the Er^{3+} ion decays to the ground state and resulted in green (521/544 nm) and red emissions (660 nm) [8], [37], [82], [84], [86].

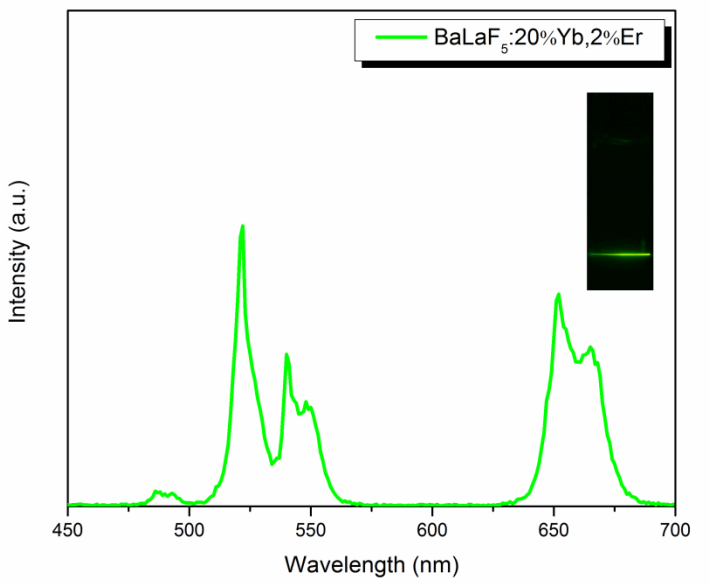

Figure 4.3 Upconversion spectrum of the PEI modified Ba_2LaF_7:Yb/Er UCNPs and the right inset shows the photograph of the Ba_2LaF_7:Yb/Er UCNPs colloidal solution (1 wt%) excited by 980 nm laser.

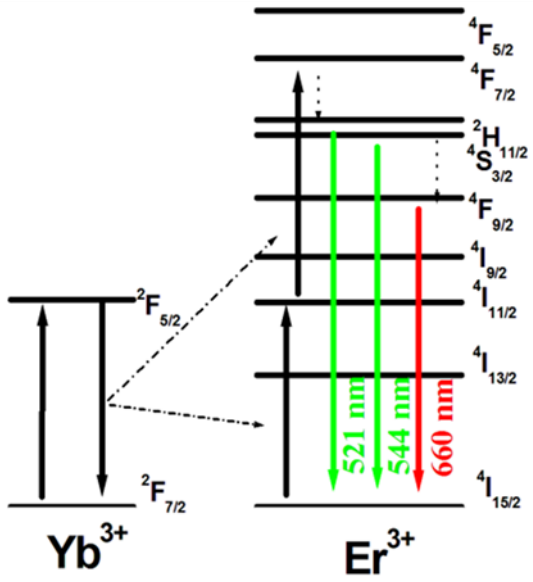

Figure 4.4 Simplified energy level diagram of Yb/Er system.

4.1.3.3 Surface group characterization

The successful capping of PEI on the surface of Ba_2LaF_7:Yb/Er UCNPs is

supported by the FTIR analysis. Fig. 4.5 shows the IR transmission spectrum of the UCNPs and the wavenumber located around 3439 cm^{-1} is due to O-H and/or N-H stretching vibration. In addition, the absorption peaks at 1409, 2850 and 2928 cm^{-1} are ascribed to the stretching vibrations of C-N bond and asymmetric and symmetric stretching vibrations of C−H bond, respectively. Also, a strong IR absorption band at 1638 is observed and this band is attributed to the N-H bond bending mode of amino group (-NH_2) and thereby supports the successful capping of PEI on the surface of the UCNPs [107-108].

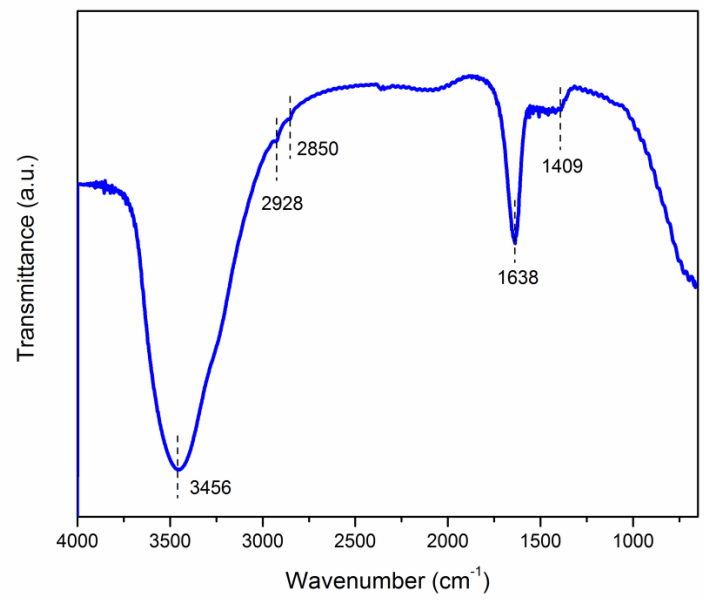

Figure 4.5 FTIR spectrum of the PEI modified Ba_2LaF_7:Yb/Er UCNPs.

4.1.3.4 *In-vitro* fluorescent bioimaging of HeLa cells

In the upconversion photoluminescence experiment, Ba_2LaF_7:Yb/Er UCNPs were excited by 980 nm laser and able to emit intense green and red UC emission. Also, the small size (< 20 nm) and good biocompatibility of the UCNPs favored them as a

fluorescent bioimaging agent. To verify the bioimaging ability, Ba_2LaF_7:Yb/Er UCNPs (100 μg ml^{-1}) was incubated with HeLa cells for 24 h at 37 ^oC with 5 % CO_2 for *in-vitro* fluorescent imaging. Firstly, the bright field image of HeLa cells (Fig. 4.6a) was taken to locate the position of cells. Upon 980 nm excitation, the fluorescent images of HeLa cells were detected in green (500-600 nm) and red (600-700 nm) channels. The HeLa cells are imaged clearly in Fig. 4.6b and c, which confirms the successful uptake of Ba_2LaF_7:Yb/Er UCNPs. Moreover, the corresponding intensity of green and red is similar to the observed UC emission spectrum that the green emission is more intense than the red emission. Fig. 4.6d-f shows the magnified bright field and respective fluorescent images of HeLa cells. These results indicated that the UCNPs had been uptaken by HeLa cells and reached the cytoplasm.

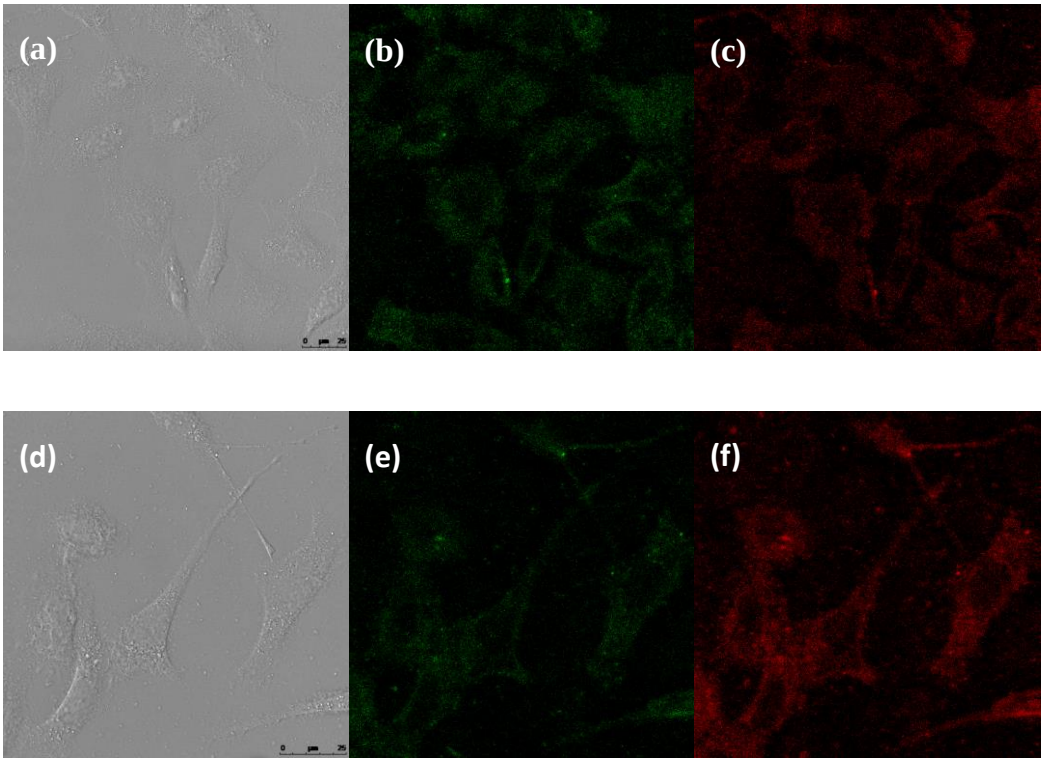

Figure 4.6 *In-vitro* imaging of the PEI modified Ba_2LaF_7:Yb/Er UCNPs in HeLa cells:

(a) bright field image of HeLa cells (low magnification) , (b) corresponding green UC fluorescent image (500–600 nm), (c) the red emission UC fluorescent image (600–700 nm) (d) bright field image of HeLa Cells (high magnification), (d) corresponding green UC fluorescent image (500–600 nm), (e) the red emission UC fluorescent image (600-700 nm). The concentration of UCNPs was 100 μg mL^{-1} and the incubation time was 24 h.

4.1.3.5 Cytotoxicity

Apart from satisfactory signal to noise ratio (SNR) for obvious fluorescent images, an ideal UC fluorescent imaging probe should present low toxicity. MTT assay was carried out to measure the toxicity of Ba_2LaF_7:Yb/Er UCNPs. HeLa Cells were incubated with Ba_2LaF_7:Yb/Er UCNPs at 37 ^oC for 24 h and 5% CO_2 at four different concentrations. Fig. 4.7 summarizes the cell viability at the corresponding concentration of Ba_2LaF_7:Yb/Er UCNPs. At 100 μg mL^{-1}, the cell viability is above 90 % which indicates the UCNPs concentration in bioimaging is of low toxicity. Importantly, when the concentration increases to 2500 μg mL^{-1}, the cell viability is able to maintain above 80 %. The fluorescent bioimaging and toxicity results indicate that the as-synthesized PEI-modified Ba_2LaF_7:Yb/Er UCNPs are low toxicity fluorescent bioimaging agent with no autoflourescence.

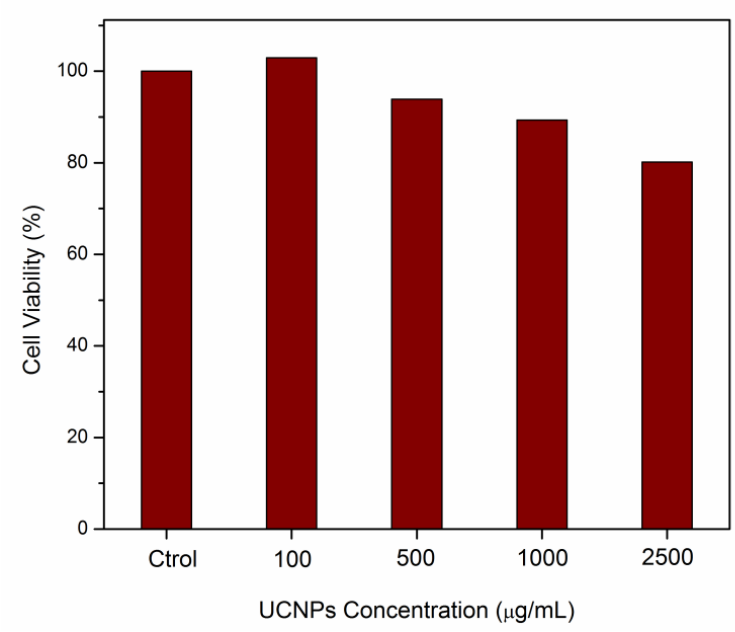

Figure 4.7 MTT assay for cytotoxicity of the PEI modified Ba_2LaF_7:Yb/Er UCNPs in HeLa cells. The PEI modified Ba_2LaF_7:Yb/Er UCNPs were incubated with HeLa cells at 37 ^oC for 24 h.

4.2 Dual-modal fluorescent/magnetic imaging by $BaGdF_5$:Yb/Er UCNPs

4.2.1 Introduction

In the previous Section, PEI modified Ba_2LaF_7 UCNPs present small average size (~ 18 nm) for bioimaging. The corresponding UC fluorescent images of HeLa cells are recorded in red and green channels. Fluorescent image provides good planar resolution but this technique is not able to image the 3D structures of soft tissues and organs [62]. Hence, it is important to increase the number of modes for bioimaging. Multi-modal imaging techniques, such as MRI and CT, are able to compensate the weakness of fluorescent imaging.

It is known that Gd doped $NaGdF_4$ UCNPs are able to demonstrate T_1 and T_2-wieghed MRI [53]. Unfortunately, the reported material is sodium based UCNPs. Recently, Lin's group reported a thermal decomposition method to synthesize core-shell structured $BaGdF_5$ which showed higher UC efficiency than hexagonal phase $NaYF_4$ UCNPs [109]. However, the as-synthesized core-shell structured $BaGdF_5$ UCNPs were hydrophobic and therefore they were not suitable for bioimaging applications. Additionally, $BaGdF_5$ provided additional paramagnetic property compared to $NaYF_4$ UCNPs because of the large magnetic moment of Gd^{3+} ions.

In this part, dual modal fluorescent/magnetic $BaGdF_5$ bioprobe were synthesized by a one-step hydrothermal synthesis with PEI modification. As-synthesized UCNPs can be readily dispersed in water and they have a size range of 8-15 nm which is ideal for bio-imaging application. Moreover, strong paramagnetic behavior was also detected

in the UCNPs. To test the biological imaging application of the PEI modified $BaGdF_5$:Yb/Er UCNPs, *in-vitro* fluorescent imaging and T_1-weighted MRI was achieved. In addition, MTT assay indicated that the $BaGdF_5$:Yb/Er UCNPs has low cytotoxicity. The $BaGdF_5$:Yb/Er UCNPs with no autofluorescence and low toxicity are expected to be a useful bioimaging probe.

4.2.2 Experimental

4.2.2.1 Hydrothermal synthesis of PEI-modified $BaGdF_5$:Yb/Er UCNPs

Water-soluble and PEI-modified $BaGdF_5$:Yb/Er UCNPs with high monodispersity were synthesized by a modified one-pot hydrothermal method [24] [88]. The synthesis procedures are the same as the aforementioned steps in section 4.1.2.1 and the molar ratio of RE dopants are changed to 78 : 20 : 2 with $Gd(NO_3)_3$ (0.5 M), $Yb(NO_3)_3$ (0.5 M) and $Er(NO_3)_3$ (0.1 M).

4.2.2.2 Characterizations

The characterization techniques are the same as mentioned in section 4.1.2.2 while ζ-potential measurements were performed on a Zetasizer 3000 HAS (Malven Instruments, UK) and the magnetization of $BaGdF_5$:Yb/Er UCNPs was measured as a function of the applied magnetic field ranging from -20 to 20 kOe at room temperature (RT) using a Lakeshore 7410 vibrating sample magnetometer (VSM).

In this section, HeLa cells are still used as the cell line for fluorescent bioimaging. Also, the cell incubation and MTT assay procedures are the same as described in section 4.1.2.2. The fluorescent agent was changed to $BaGdF_5$:Yb/Er instead of Ba_2LaF_7:Yb/Er UCNPs.

The relaxation property of the amine-functionalized $BaGdF_5$:Yb/Er UCNPs was characterized on a 3T Siemens Magnetom Trio by detecting the longitudinal relaxation times (T_1) using a standard inversion-recovery (IR) spin-echo sequence. The molar relaxivity $1/T_1$ (R_1) can be determined by the slope of the following equation [108].

$$(1/T_1)_{obs} = (1/T_1)_d + R_1[M]$$

Where $(1/T_1)_{obs}$ and $(1/T_1)_d$ are the observed values in the presence and absence of BaGdF5 UCNPs, respectively. [M] is the concentration of $BaGdF_5$ UCNPs. The T_1-weighted MRI images were acquired at RT using a 3T Siemens Magnetom Trio. Various concentrations of amine functionalized $BaGdF_5$:Yb/Er UCNPs (0, 0.2, 0.4, 0.8 mM) water solutions were put in a series of 1.5 mL tubes for T_1-weighted MRI with a T_1-weighted sequence.

4.2.3 Results and discussion

4.2.3.1 Structural property

The size and morphology of amine-functionalized $BaGdF_5$:Yb/Er UCNPs was revealed by TEM. Fig. 4.8a, b and f shows the UCNPs present a spherical-like morphology and the average size of UCNPs is about 10 nm. The selected area electron diffraction (SAED) pattern of the UCNPs is shown in Fig. 4.8c and the patterns suggest that the as-prepared UCNPs demonstrate cubic phase structure. Moreover, the observed lattice fringes in the high resolution TEM (HRTEM) image in Fig. 4.8d confirms the single crystalline nature and high crystallinity of the UCNPs. The inset of Fig. 4.8d

shows the corresponding fast Fourier Transformation (FFT) pattern of a single UCNP which results in regular diffraction spots along the [111] zone axis and therefore suggesting that the UCNPs have a single crystalline nature. Also, the inter-planar separation, d, is found to be about 2.13 Å, which is close to the d value of the (220) plane of the face-centre cubic phase of $BaGdF_5$. Moreover, the XRD pattern in Fig. 4.8e matchs well with the standard XRD pattern of cubic phase $BaGaF_5$ and no other spurious peaks are detected. To verify the chemical composition of $BaGaF_5$:Yb/Er, energy dispersive X-ray spectroscopy (EDS) was applied and the corresponding EDS spectrum is shown in Fig. 4.8g. The EDS peaks are mainly due to Ba, Gd, F and Yb. Due to the low level doping of Er, this element is not detected in the spectrum. However, it is important to note that the strong EDS peaks from Cu and C are due to the TEM copper grid and the carbon film covering the copper layer. The EDS spectrum has confirmed the chemical composition of the as-synthesized $BaGdF_5$:Yb/Er UCNPs.

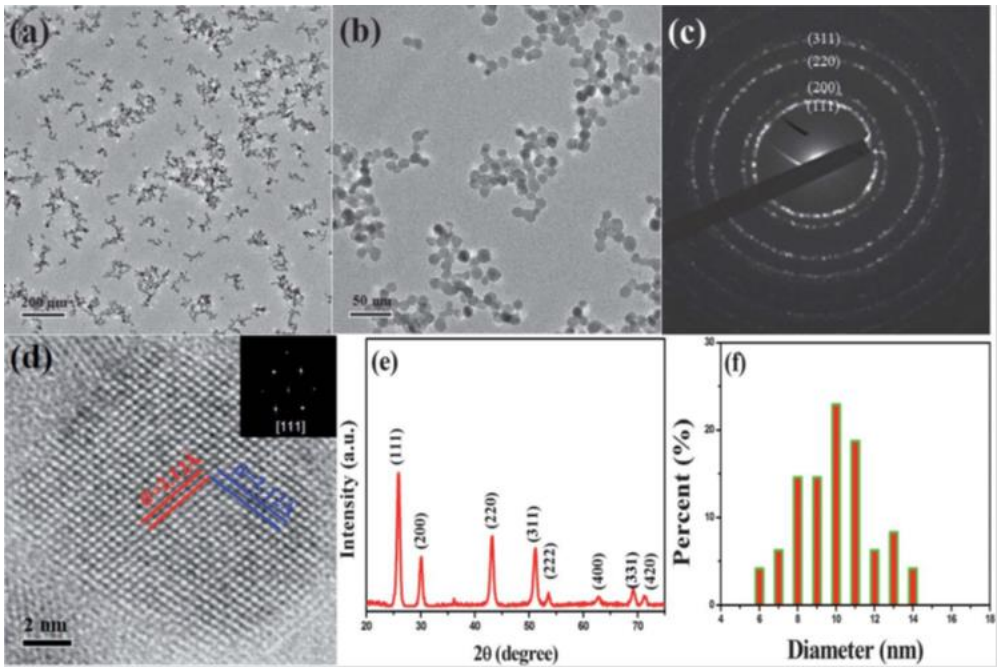

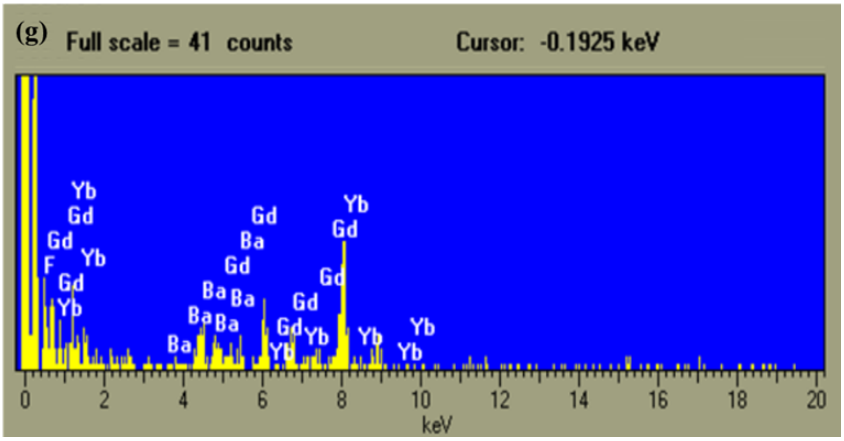

Figure 4.8 TEM and XRD results of the amine-functionalized $BaGdF_5$:Yb/Er UCNPs: (a) typical low magnification TEM image, (b) high-magnification TEM image, (c) SAED, (d) HRTEM image of single particle, (e) XRD pattern, (f) histogram of the particle size distribution, (g) energy dispersive X-ray (EDS) spectrum.

4.2.3.2 Surface group characterization

In order to enhance the water dispersibility and cell uptake of $BaGdF_5$:Yb/Er UCNPs, PEI was selected as the surfactant in hydrothermal synthesis. From earlier report, it is known that the capping of positively charged amino group on the surface of NPs can enhance the water solubility and facilitates cell-uptake compared with some neutral and negatively charged polymers such as polyvinylpyrrolidone (PVP) and polyacrylic acid (PAA) [110]. Firstly, the ζ-potential of the colloidal amine-functionalized $BaGdF_5$:Yb/Er UCNPs was measured to be about +27.6 mV and this confirmed the positive surface nature of UCNPs thus providing a primary evidence of successfully capping of PEI on UCNPs. The capping of PEI was further revealed by FTIR spectrometry and the corresponding FTIR spectrum is shown in Fig. 4.9. A broadband absorption is observed at 3449 cm^{-1} and it is attributed to the amine (N-H)

bond stretching vibration [107].

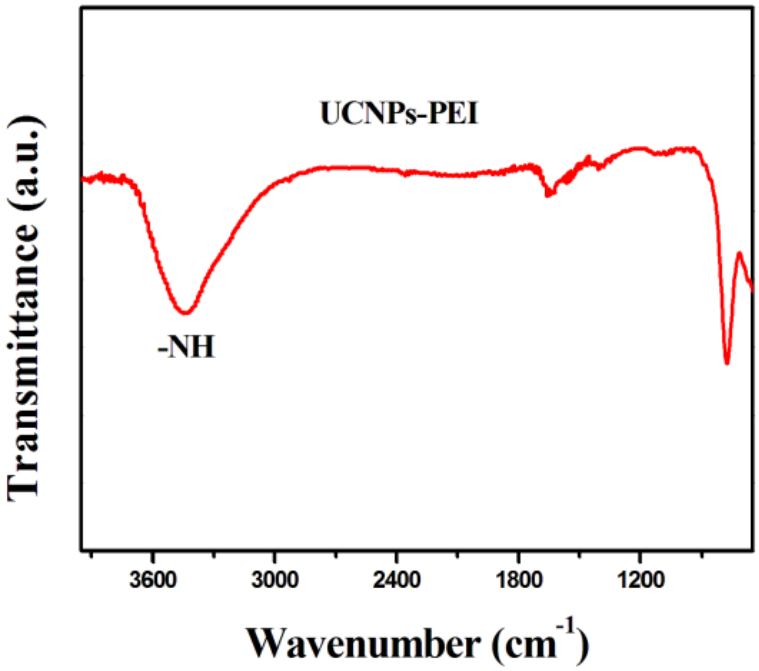

Figure 4.9 FTIR spectrum of the amine-functionalized $BaGdF_5$:Yb/Er UCNPs.

4.2.3.3 Upconversion photoluminescence

In order to demonstrate the enhancement of water solubility due to capping of PEI, the as-prepared $BaGdF_5$:Yb/Er UCNPs are dispersed in water to form a colloidal solution (1 wt%) of $BaGdF_5$:Yb/Er UCNPs solution is shown in the left inset of Fig. 4.10a. The high transparency of the solution indicates good water solubility of UCNPs in water. Moreover, the right inset of Fig. 4.10a shows intense and eye-visible green UC emission from UCNPs under illumination of 980 nm laser diode (LD). Fig 4.10a depicts the UC emission spectrum of PEI-modified UCNPs and three strong emission bands centered at 521, 544 and 660 nm are observed. The power law for UC is applied to realize the physical mechanism of the UC at 521, 544 and 660 nm, generally, the formula is given by $I_{UC} \alpha I^n_{IR}$ .The formula describes that the output UC luminescent intensity (I_{UC}) is proportional to the infrared excitation (I_{IR}) power and n is the number

of pump photons required to populate the upper emitting level and its value can be obtained from the slope of the line in the plot of log I_{UC} against log I_{IR} [35]. Fig. 4.10b shows a log-log plot of the UC emission intensity as a function of pump power intensity for each of the observed emission band. From the slope, n can be found and the values for 521, 544 and 660 nm are 1.76, 1.79 and 1.55 respectively. These values indicate that the UC at the respective wavelengths are two photon UC process. In addition, the existence of the three emission bands can be deduced by the simplified energy level diagram in Fig. 4.4. According to the diagram, it was clear that UC process is initiated by the absorption of 980 nm IR photon by Yb^{3+} ion, then energy is transferred to the neighboring Er^{3+} ion in the form of phonon due to upward transition of Yb^{3+} from $^2F_{7/2}$ to $^2F_{5/2}$. Owing to the ladder-like and well matching of energy level of Er^{3+} ion, the Er^{3+} ion was pumped to higher energy levels. It is also important to note that the life time for the metastable state of Er^{3+} ion was long to facilitate pumping of Er^{3+} ion to higher energy level is possible. As a result, Er^{3+} ion is pumped from $^4I_{15/2}$ to $^4I_{11/2}$ and $^4F_{7/2}$. Subsequently, non-radiative transition and downward transition result in three emission bands at 521, 544 and 660 nm due to electronic transitions: $^2H_{11/2}$, $^4S_{3/2}$ and $^4F_{9/2}$ to $^4I_{15/2}$ of Er^{3+} ion respectively.

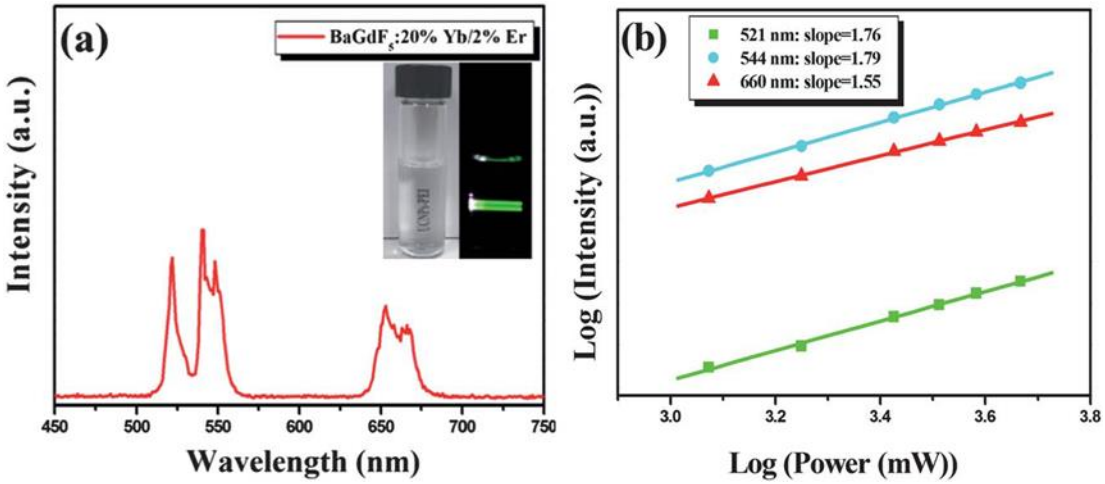

Figure 4.10 (a) UC spectra of the amine-functionalized $BaGdF_5$:Yb/Er NPs, the left inset showed the optically transparent solution of $BaGdF_5$ NPs dispersed in water, the right inset showed the photograph of the transparent solution excited by 980 nm laser, (b) log-log plots of the UC luminescence intensity versus excitation power study of $BaGdF_5$:Yb/Er NPs.

4.2.3.4 *In-vitro* bioimaging

Owing to the strong and eye-visible luminescence property of water dispersible PEI-modified $BaGdF_5$:Yb/Er UCNPs, they had high potential to be used in *in-vitro* imaging. As a result, the UCNPs (100 μg mL^{-1}) were readily incubated with HeLa cells at 37 ^{o}C with 5% CO_2 for 24 h under multi-photon confocal microscopy. The luminescence of UCNPs in HeLa cells excited by 980 nm photons were detected in two channels: green (500-600 nm) and red (600-700 nm). Fig. 4.11a shows a bright field image of the as-incubated HeLa cells and the respective UC luminescence images are shown in Fig. 4.11b and c. It is clear that the UCNPs are effectively uptaken by the HeLa cells and hence the cell membrane is imaged under 980 nm excitation. Moreover, the intensity of the green UC image in Fig. 4.11b is stronger than red color in Fig. 4.11c.

Indeed, this observation is consistent with the PL spectra of Fig. 4.10a. The power dependent UC luminescence of UCNPs in HeLa cells are examined by using the red channel. Fig. 4.12b, c and d show a series of red UC image of incident laser power ranging from 300 to 800 mW. First, this result indicates that there was no background fluorescence under a high pumping power (800 mW) and thus resulted in good signal to noise ratio. Second, the enhanced red UC signal further confirms the incubation of UCNPs in HeLa cells.

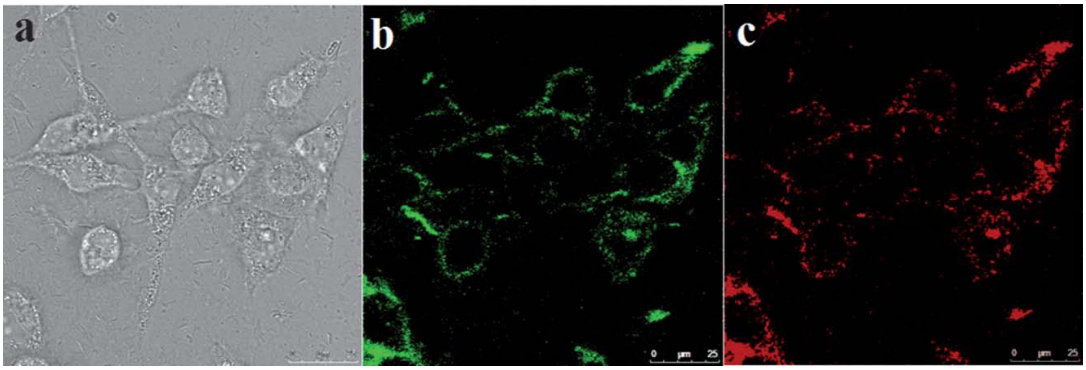

Figure 4.11 *In-vitro* imaging of the PEI modified $BaGdF_5$:Yb/Er colloidal UCNPs in HeLa cells: (a) bright field image of HeLa cells, (b) corresponding green UC fluorescent image (500–600 nm), (c) the red emission UC fluorescent image (600–700 nm). The concentration of UCNPs was 100 μg mL^{-1} and the incubation time was 24 h.

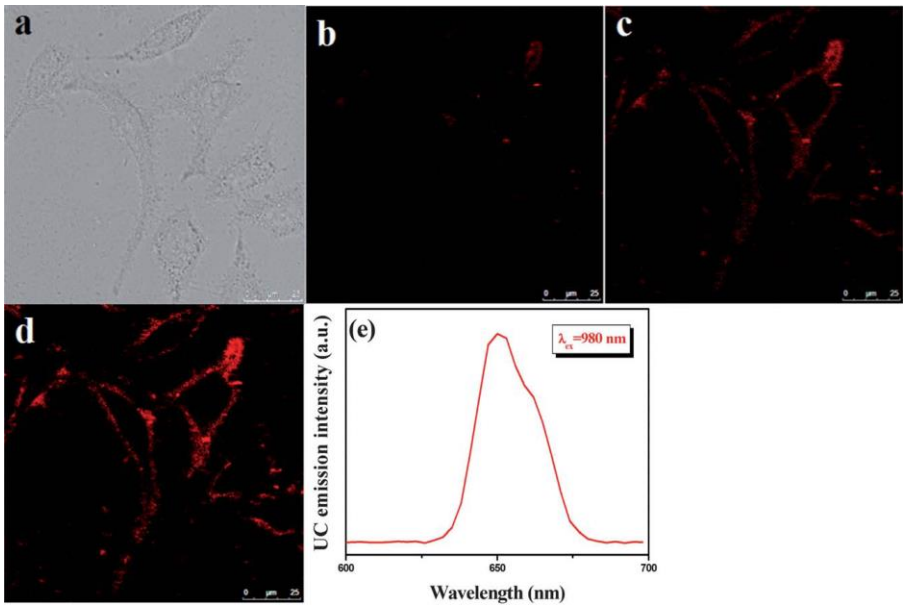

Figure 4.12 Power dependent *In-vitro* imaging of HeLa cells upon excitation by 980 nm laser with different excitation power after being incubation of amine-functionalized $BaGdF_5$:Yb/Er UCNPs: (a) bright field image, and: (b) 300 mW, (c) 500 mW, (d) 800 mW, (e) the corresponding upconverting *in-vitro* emission spectra obtained from Fig. 4d. The concentration of UCNPs was 100 μg mL^{-1} and the incubation time was 24 h.

4.2.3.5 Cytotoxicity

MTT assay was used to examine the cytotoxicity of $BaGdF_5$:Yb/Er UCNPs. Different concentrations of $BaGdF_5$:Yb/Er UCNPs were prepared and incubated with HeLa cells at 37 ^oC, 5% CO_2 for 24 h. Fig. 4.13 suggests that the cell viability is over 90 % at 100 μg mL^{-1} UCNPs. When the concentration of UCNPs is increased to 2500 μg mL^{-1}, the viability of cells is still able to maintain above 80%. As a result, the as-synthesized PEI-modified $BaGdF_5$:Yb/Er UCNPs is a low toxicity and promising fluorescent bio-probe with no autofluorescence.

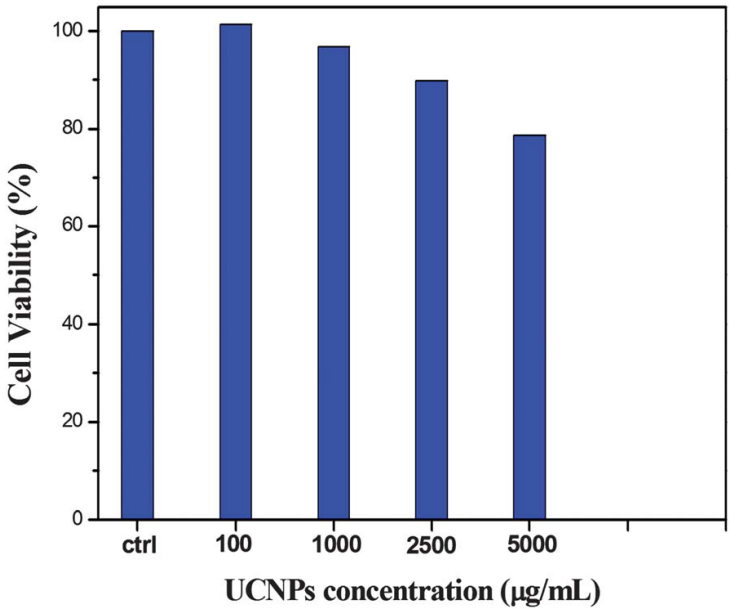

Figure 4.13 MTT assay for cytotoxicity of the $BaGdF_5$:Yb/Er UCNPs in HeLa cells. The UCNPs were incubated with HeLa cells at 37 ^oC for 24 h.

4.2.3.6 Magnetic resonance imaging

It is known that Gd^{3+} ions possess large magnetic moment and the doping of this ion into $BaGdF_5$:Yb/Er UCNPs enables the magnetic property. As a result, it is possible for the UCNPs to be used as a magnetic resonance imaging (MRI) contrast agent. Firstly, the magnetic property of $BaGdF_5$:Yb/Er UCNPs was revealed by VSM and the corresponding magnetization is measured from the applied magnetic field range -20 kOe to 20 kOe under room temperature (Fig. 4.14a). The UCNPs exhibit paramagnetic behavior and the paramagnetism in the UCNPsias originated from the seven unpaired inner 4f electrons, which are closely bound to the nucleus and effectively shielded by the outer closed shell electrons $5s^25p^6$ from the crystal field [2], [61]. The magnetic mass susceptibility of the amine-functionalized $BaGdF_5$ UCNPs is found to be 4.72 $x10^{-5}$ emu/gOe. The magnetization of $BaGdF_5$ UCNPs is about 0.95 emu/g at 20 kOe, which

was close to the value reported for nanoparticles used for common bioseparation [2], [82], [84]. After that, different concentrations of UCNPs were prepared to demonstrate the feasibility of using $BaGdF_5$ UCNPs as MRI contrast agent. A 3 T MRI scanner is applied to study the ionic longitudinal relaxivity (R_1) at different molar concentrations. From the slope of Fig. 4.14b, the molar relaxivity is found to be 1.194 S^{-1} mM^{-1}. Moreover, Fig. 4.14c show the typical concentration dependent MRI images of $BaGdF_5$ UCNPs and it can be clearly seen that the MRI contrast is greatly enhanced upon increment of UCNPs concentrations. Therefore, $BaGdF_5$ UCNPs may be able to be used as a T_1-weighted MRI contrast agent. Here, the results presented a simple protocol to prepare bi-functional UCNPs (fluorescent and magnetic property) and it had significantly reduced the need for complicated procedures.

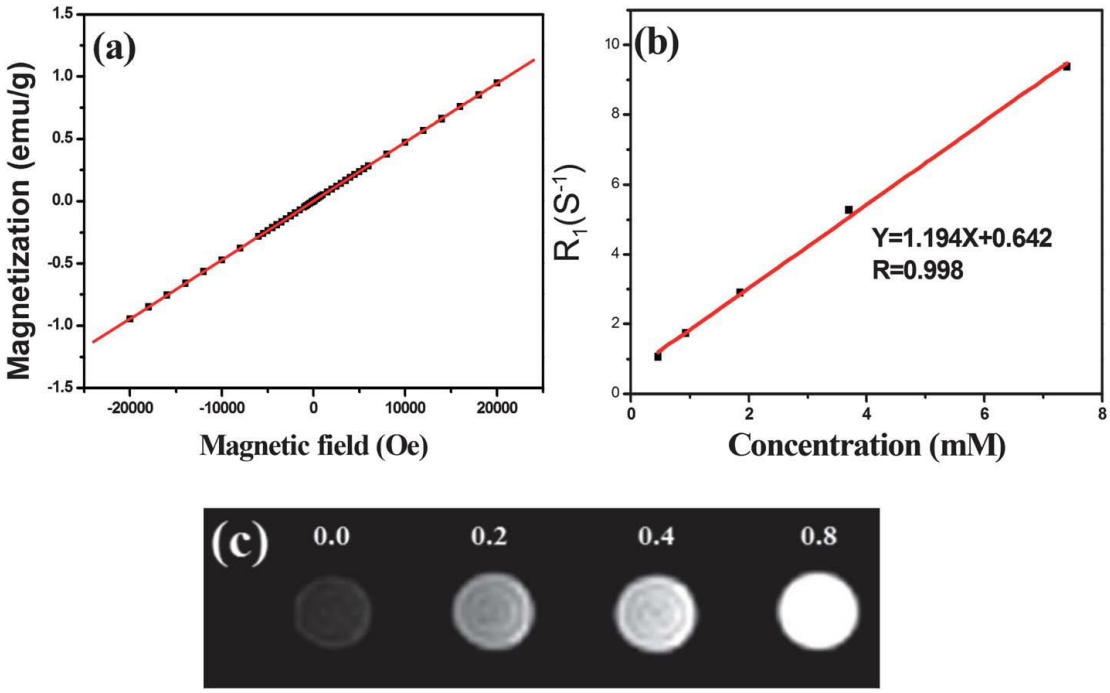

Figure 4.14 (a) Magnetization as a function of applied field for $BaGdF_5$:Yb/Er UCNPs at room temperature, (b) relaxation rate R_1 ($1/T_1$) versus various molar concentrations of $BaGdF_5$:Yb/Er UCNPs at room temperature using a 3 T MRI scanner, (c) T_1-weighted images of $BaGdF_5$:Yb/Er UCNPs with different concentrations (mM) in water.

4.3 Multi-modal fluorescent/MRI/CT imaging by $BaGdF_5$:Yb/Er UCNPs

4.3.1 Introduction

Recently, much effort has been focused on studying bioimaging because of its ability to visualize and realize many features, functions and structures of cells and tissues. Fluorescent imaging [96], [111-112], magnetic resonance imaging (MRI) [86], [113-114] and computed X-ray tomography (CT) [115-117] are three important bioimaging techniques. Among them, CT is a well-established clinical diagnostic technique which is capable of providing high-resolution 3D information of the anatomic structure of tissues based on the difference in X-ray absorption of the tissues. However, this imaging technique is limited by the low absorption of soft tissues and thus limits its applications in disease detection. On the other hand, MRI is capable of imaging excellent 3D soft tissue details and functional information because of the non-intrusive radiation. Despite the superior features of CT and MRI, they have limited planar resolution which is not suitable for cellular level imaging. In this regard, fluorescent imaging can compensate the shortage. As a result, it is worth to combine the three imaging techniques into a single system.

To date, there are limited reports about the development of trimodal imaging bioprobe. Recently, a trimodal fluorescent/MRI/CT imaging system based on CdS: Mn/ZnS quantum dots were reported [118]. Unfortunately, quantum dots suffer from non-idealities such as high toxicity and shallow penetration depth in tissues owing to the UV excitation. Hence, these non-idealities limited their biological applications. On

the other hand, $NaYF_4$ is a frequently reported UC fluorescent bioimaging agent [103-104], [119] and a recent report about the design of a trimodal bioimaging agent based on PEGylated NaY/GdF_4:Yb/Er, Tm@SiO_2-Au@PEG_{5000} UCNPs synthesized by co-thermolysis method in non-hydrolytic solvents and multi-step synthesis [120]. The problem of non-hydrophilic is solved by further surface modifications in which results in complicated and costly procedures. Thus, it is worthwhile to develop a facile method to prepare trimodal fluorescent/MRI/CT bioimaging agent. Previously, RE doped $BaGdF_5$ UCNPs demonstrate outstanding UC property with paramagnetic property because of the large magnetic moment of Gd^{3+} ions. By combining the two properties, a dual-modal fluorescent/MRI bioprobe was developed for biomedical applications [51], [86]. What deserved to be mentioned is the large K-edge values of barium (Ba) and gadolinium (Gd) in $BaGdF_5$ (Ba K-edge: 37.4 keV, Gd K-edge: 50.2 keV) [121] and high X-ray mass absorption coefficients (at 60 keV, Ba: 8.51 $cm^2\ g^{-1}$, Gd: 1.18 $cm^2\ g^{-1}$; at 80 keV, Ba: 3.96 $cm^2\ g^{-1}$, Gd: 5.57 $cm^2\ g^{-1}$) [122] which enable them for potential CT contrast imaging applications. Considering the different X-ray mass absorption coefficients and large K-edge values, $BaGdF_5$ host have high potential as CT contrast imaging agents at different photon energies for different groups of patient in clinical CT applications. Moreover, $BaGdF_5$:Yb/Er based trimodal fluorescent/MRI/CT probe has not been reported.

4.3.2 Experimental

4.3.2.1 Hydrothermal synthesis of PEG-modified $BaGdF_5$:Yb/Er UCNPs

Other materials and concentration of RE dopants are the same as section 4.1.2.1 and 4.2.2.1. The surfactant PEI was changed to Poly (ethylene glycol) methyl ether (PEG, average molecular weight = 5000), which was purchased from Sigma-Aldrich.

PEG-modified $BaGdF_5$:Yb/Er UCNPs were synthesized by a one-pot hydrothermal method [86]. The synthesis procedures were identical to the steps described in section 4.2.2.1 and 4.2.2.2. The surfactant was changed from PEI to PEG.

4.3.2.2 Characterizations

The characterizations of PEG modified BaGdF5:Yb/Er UCNPs were the same as described in section 4.2.2.2 while the PEI-modified $BaGdF_5$:Yb/Er UCNPs was changed to PEG-modified $BaGdF_5$:Yb/Er UCNPs.

PEG-modified $BaGdF_5$:Yb/Er UCNPs at different concentrations (0, 5, 10, 20, 40, 80 mM) were dispersed in de-ionized water for *in-vitro* CT imaging. In order to study the *in-vivo* CT imaging, a mouse was first anesthetized by intraperitoneal injection of chloral hydrate solution (10 wt%), and then 500 μL physiological saline solutions containing the PEG-modified $BaGdF_5$:Yb/Er UCNPs (0.05 M) were intravenously injected into the mouse via the mouse's caudal vein. CT images were acquired using ZKKS-MCT-Sharp (Chinese Academy of Sciences and Guangzhou Kaisheng Medical Technology Co., Ltd.) as following parameters: thickness, 0.14 mm; pitch, 0.07; 60 KVp, 0.5 mA; large field view; gantry rotation time, 0.5 s; speed, 5 mm/s.

4.3.3 Results and discussion

4.3.3.1 Structural property

TEM image of the as-prepared $BaGdF_5$:Yb/Er UCNPs is shown in Fig.4.15a. The UCNPs demonstrate excellent monodispersity. The UCNPs present spherical morphology with a measured average size of 12.02 ± 1.55 nm (inset of Fig. 4. 15a). In addition, the selected area electron diffraction (SAED) pattern in Fig. 4.15b indicated that the as-synthesized UCNPs are face-centered cubic (FCC) structure. High resolution TEM (HRTEM) image of a single NP is captured (Fig. 4.15c) and clear lattice fringes are observed. The measured d-spacing of 2.1 Å matches well with the (220) standard lattice plane of FCC phase of $BaGdF_5$. To further confirm the phase structure of PEG-modified $BaGdF_5$, powder X-ray diffraction (XRD) was applied to detect the phase composition. In Fig. 4.15d, the diffracted peaks are readily indexed to FCC $BaGdF_5$ (JSPDS 24-0098) and no impurity peaks were detected. Moreover, the substitution of Gd^{3+} by Yb^{3+} ions results in the shifting of diffracted peak to higher 2-theta angle in Fig. 4.15d [81-82], [84]. The chemical composition of $BaGdF_5$ UCNPs was investigated by energy dispersive X-ray spectroscopy (EDS) and Fig. 4. 15e suggests that the UCNPs consist of Ba^{2+}, Gd^{3+}, F^- and Yb^{3+} ions, in which Yb^{3+} ions were successfully doped into the $BaGdF_5$ matrix. It should be noted that the C and Cu peaks are due to the TEM copper grid and the covered carbon film on the supporting copper.

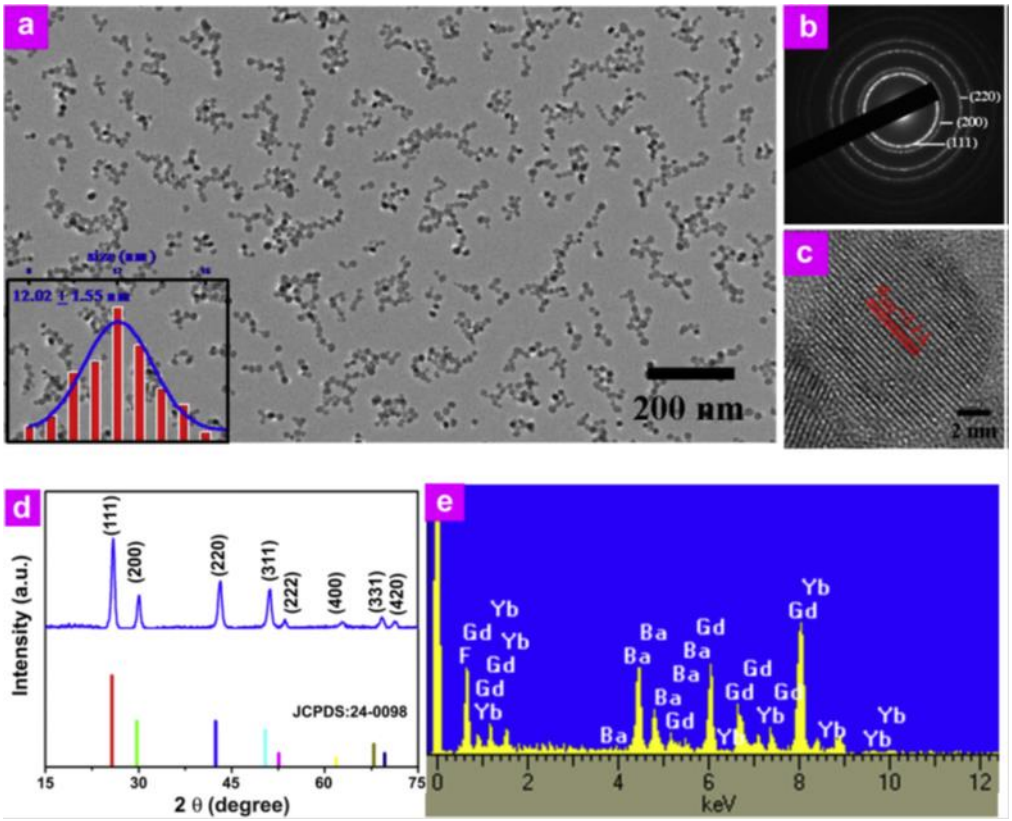

Figure 4.15 (a) TEM image and (inset) the size distribution with average size in nm (b) selected area electron diffraction (SAED) pattern (c) high resolution TEM (HRTEM) of a single NP showing the d-spacing (d) X-ray diffraction pattern indexed with standard FCC $BaGdF_5$ (JSPDS 24-0098) (e) energy dispersive X-ray spectrum of PEG-modified $BaGdF_5$:Yb/Er UCNPs.

4.3.3.2 Surface group characterization

Multi-functional PEG-modified $BaGdF_5$:Yb/Er UCNPs were synthesized by a one-step hydrothermal method using PEG as capping agent. Firstly, Fig. 4.16 shows the Fourier transform infrared (FTIR) spectrum and the broad absorption band centered at 3451 cm^{-1} is due to the O-H bond stretching vibration. Moreover, the absorption peaks at 1634 and 1496 cm^{-1} are attributed to the methylene scissoring and C–O–C stretching vibration [88]. The FTIR results indicate the successful capping of PEG on the surface

of $BaGdF_5$: Yb/Er UCNPs.

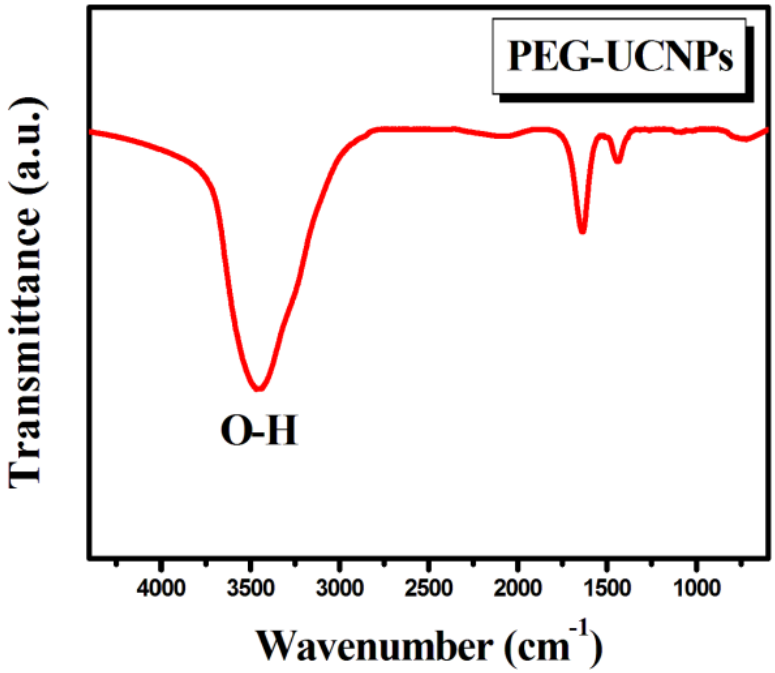

Figure 4.16 FTIR spectrum of the PEG-modified $BaGdF_5$:Yb/Er UCNPs.

4.3.3.3 Upconversion luminescence

The UC property of PEG-modified $BaGdF_5$:Yb/Er UCNPs was examined by 980 nm laser excitation. The resultant UC spectrum is shown in Fig. 4.17a. In the inset of Fig. 4.17a, intense and eye-visible green UC emission is observed in a 1 wt% colloidal solution of PEG-modified $BaGdF_5$:Yb/Er. From the UC emission spectrum, three UC emission peaks centered at 520, 544 and 660 nm are observed and the existence of corresponding emission peaks could be deduced by using the simplified energy level diagram of Yb/Er system (Fig. 4.4). The three emission bands with peaks at 520, 544 and 660 nm are attributed to the following electronic transitions: $^2H_{11/2}$ /$^4S_{3/2}$ → $^4I_{15/2}$ and $^4F_{9/2}$ → $^4I_{15/2}$ of Er^{3+} ions. To further reveal the UC mechanism of the transitions in Er^{3+} ions, the UC power dependence of the UC emission wavelengths

were studied by using the following formula, $I_{UC} \alpha I^{n}_{IR}$,where n is the number of NIR photon absorbed for per visible photon emitted and its value can be obtained from the slope of by linear fitting in the plot of log I_{UC} versus log I_{IR} (Fig. 4.17b) [86]. The slope values of the linear fit for the green and red emissions at 520, 544 and 660 nm are 2.05, 1.95 and 1.92, respectively. These values are close to two which means that a two photon UC process was involved in both green and red UC luminescence. Hence, the slope values can support the deduction in the simplified energy level diagram.

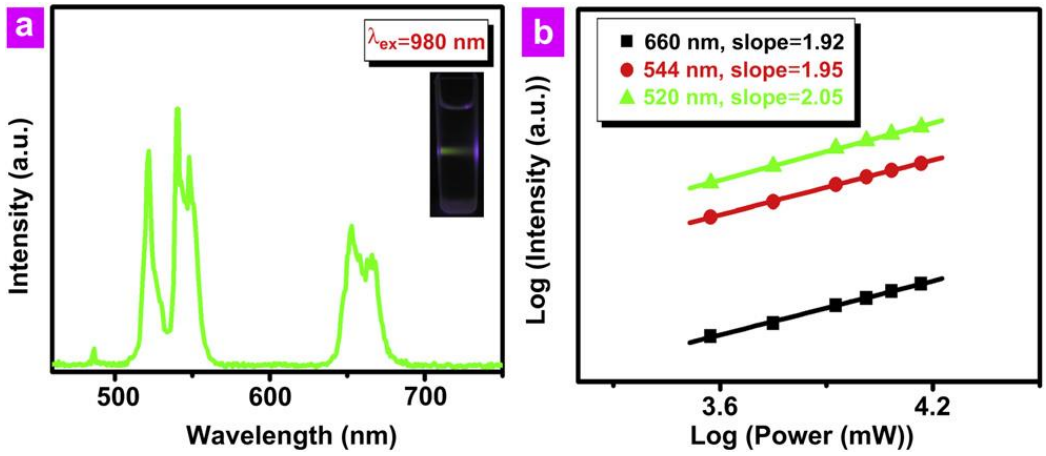

Figure 4.17 (a) UC photoluminescence spectrum of PEG-modified $BaGdF_5$:Yb/Er UCNPs under 980 nm laser excitation (inset showing intense green UC emission with 1 wt% UCNPs colloidal solution) (b) Log-log plot of UC intensity at 520,554 and 660 nm against output 980 nm laser excitation.

4.3.3.4 *In-vitro* fluorescent bioimaging and cytotoxicity

To test the bio-imaging ability of the PEG-modified $BaGdF_5$:Yb/Er UCNPs, UCNPs (150 μg ml^{-1}) were incubated with HeLa cells at 37 ^{o}C for 24 h under 5% CO_2 and then tested by confocal optical microscopy. The fluorescent bio-imaging were detected at green (500-600 nm) channel and red (600-700 nm) channel (Fig. 4.18). In

Fig. 4.18b and c, the cells appear green and red under 980 nm laser excitation and these results indicate the successful incubation of UCNPs into the HeLa cells. In addition, MTT assay (Fig. 4.19) shows that the as-prepared PEG-modified $BaGdF_5$:Yb/Er UCNPs for fluorescent bio-imaging had low toxicity. In Fig. 4.19, the corresponding cell viability of HeLa cells at various concentrations are shown. At high concentration (2500 μg ml^{-1}), the viability of HeLa cells could be maintained at about 86 % and it showed that the PEG-modified $BaGdF_5$:Yb/Er UCNPs are promising fluorescent bioprobe with low toxicity.

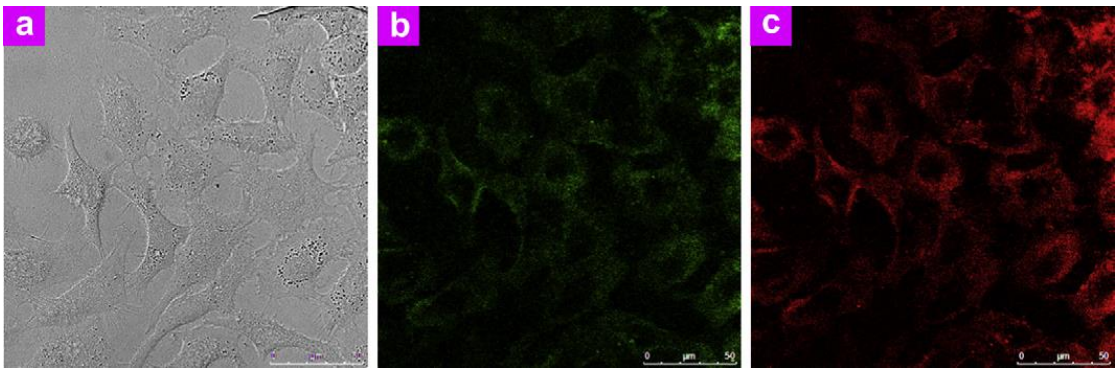

Figure 4.18 (a) bright field image of HeLa cells, (b) corresponding green UC fluorescent image (500-600 nm) and (c) the red emission UC fluorescent image (600-700 nm) of *in-vitro* bioimaging of the PEG-modified $BaGdF_5$:Yb/Er UCNPs (150 μg ml^{-1} in HeLa cells).

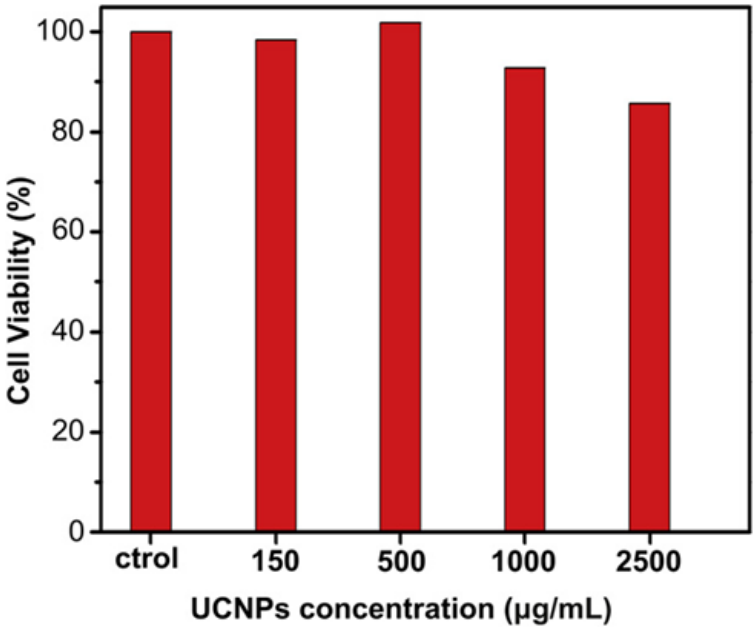

Figure 4.19 Cell viability of HeLa cells under various concentrations of PEG-modified $BaGdF_5$: Yb/Er UCNPs incubated at 37 ^oC for 24 h under 5% CO_2.

4.3.3.5 Computed X-ray tomography imaging

Owing to the large X-ray K-edge values of Ba and Gd in PEG-modified $BaGdF_5$:Yb/Er UCNPs, they have great potential to be used as a CT contrast agent. To test the CT imaging ability of the UCNPs, X-ray CT phantom images were captured by using different concentrations of PEG-modified $BaGdF_5$:Yb/Er in deionized water at 60 keV. In Fig. 4.20a, upon increment of concentrations of UCNPs, the CT images exhibit enhanced contrast. To analyze the results (Fig. 4.20b), the CT number called Hounsfield units (HU) increased linearly with the concentrations of the UCNPs which implies increased absorption at higher concentrations.

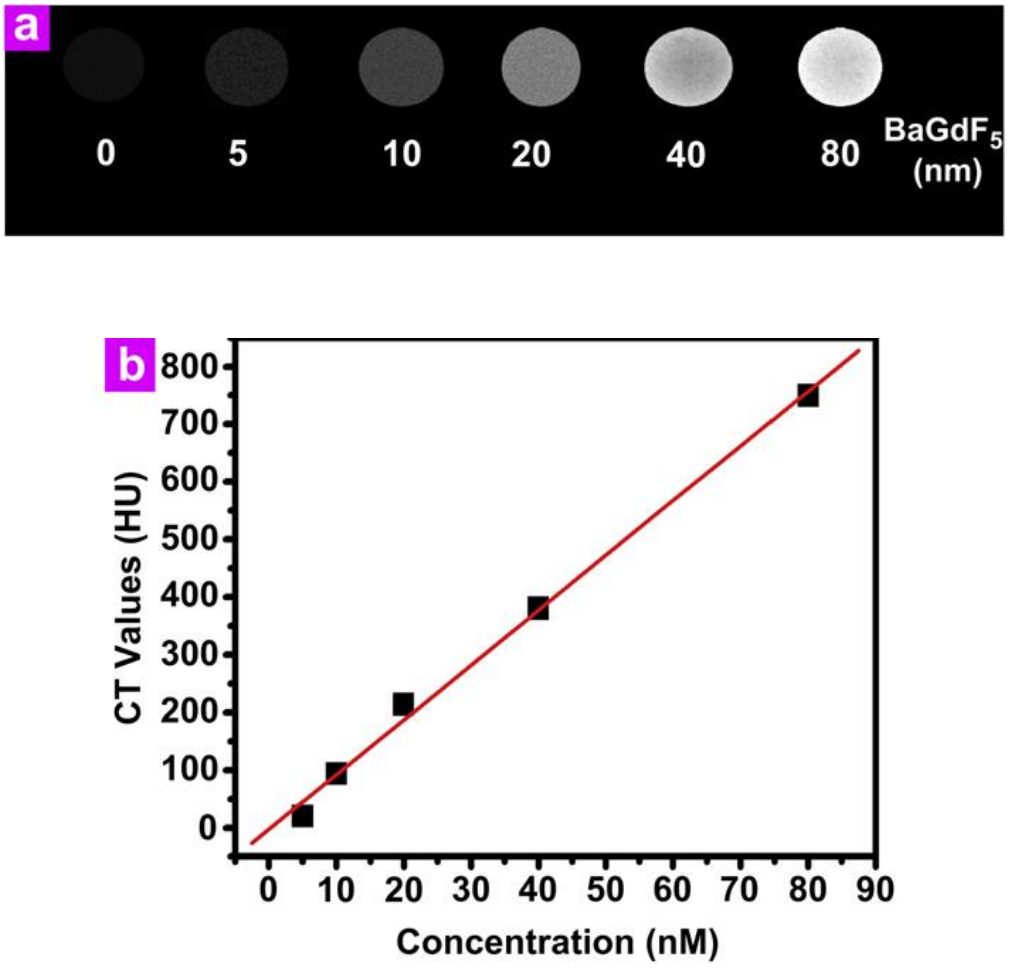

Figure 4.20 (a) CT images of water solutions under different concentrations and (b) the measured CT values (Hounsfield units, HU) of PEG-modified $BaGdF_5$: Yb/Er UCNPs.

To further validate the *in-vivo* application of PEG-modified $BaGdF_5$:Yb/Er UCNPs as a CT imaging bioprobe, a mouse was intravenously injected with PEG-modified $BaGdF_5$:Yb/Er UCNPs solution (500 mL, 0.05 M) and was detected by X-ray CT imaging at different injecting time (Fig. 4.21). Before injection, no soft tissues could be rendered by CT imaging (Fig. 4.21a). After injecting for 5 min, a weak signal of the spleen could be observed from the 3D volume-rendered (VR) CT image (Fig. 4.21b). When time increases to 30 to 60 min, enhanced CT image of the spleen could be observed in Fig. 4.21c and d. At 120 min, the spleen could be clearly imaged by 3D VR

(Fig. 4.21e) which manifests the UCNPs could be used as CT contrast imaging agent for splenic disease detection. Importantly, the persisting enhancement of the signal may improve the detection of diseases [117]. Moreover, owing to the different absorption coefficients of Ba and Gd at different photon energies in $BaGdF_5$ (Fig. 4.22) [122] the UCNPs might meet the requirements from various groups of patients for diagnostic imaging.

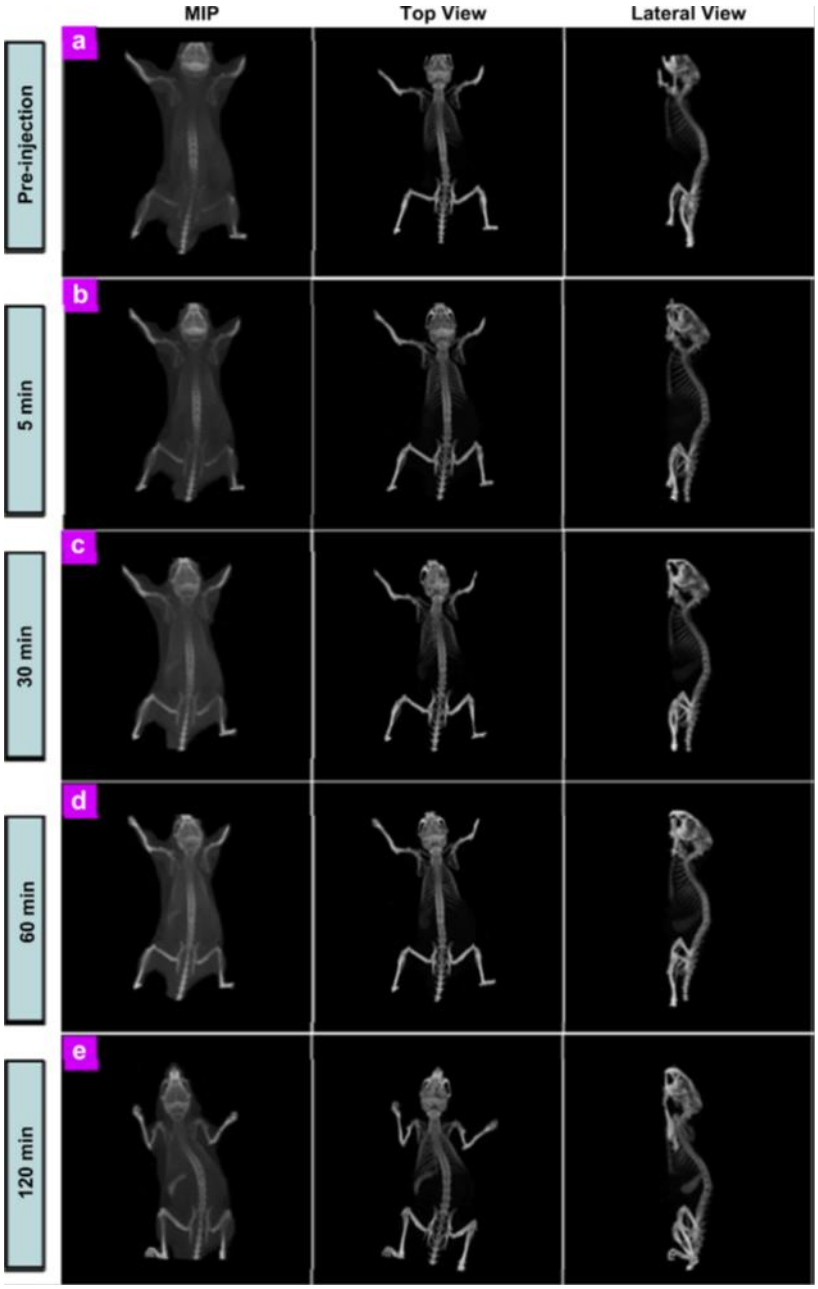

Figure 4.21 *In-vivo* X-ray CT imaging of a mouse before and after intravenous injection of 500 mL of PEG-modified $BaGdF_5$:Yb/Er UCNPs (0.05 M) at different time periods: (a) pre-injection, (b) 5 min, (c) 30 min, (d) 60 min, (e) 120 min. The left panel: maximum intensity projection (MIP), the middle panel: the corresponding 3D volume-rendered (VR). *In-vivo* CT images of mice, the right panel: lateral view of 3D VR CT images.

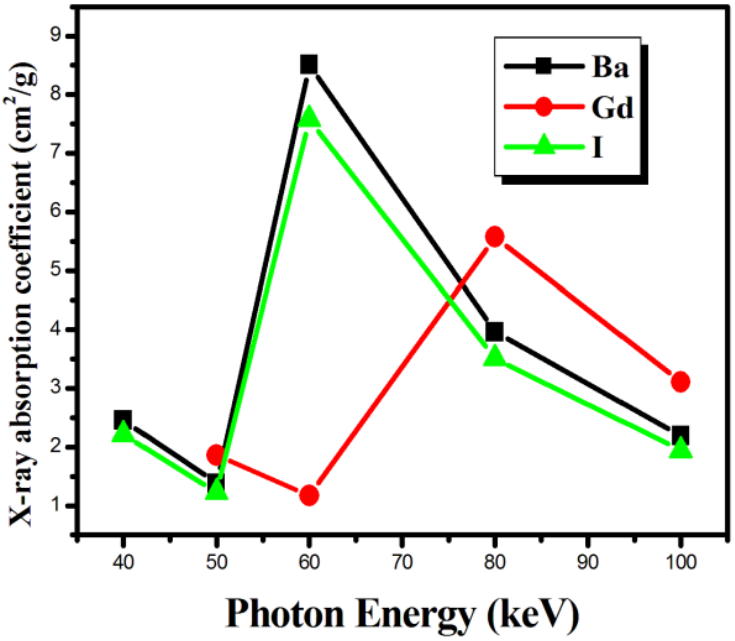

Figure 4.22 X-ray K-edge absorption coefficients of Ba, Gd, and I at different photon energies [6]. Ba has maximum X-ray absorption coefficient at 60 keV and Gd possesses maximum X-ray absorption coefficient at 80 keV. The graph shows that our designed PEG-modified $BaGdF_5$:Yb/Er UCNPs as CT contrast agent can achieve high CT contrast efficacy at different photon energy for various diagnostic imaging of various patient groups.

4.3.3.6 Magnetic property

Gd possesses large X-ray k-edge value thus it can facilitate X-ray CT, however it should be noted that Gd^{3+} also provides the UCNPs additional paramagnetic property (Fig. 4.23) owing to the large magnetic moment of Gd^{3+} which enables it be used as an MRI contrast agent. The arising of paramagnetic property is due to the seven unpaired inner 4f electrons in Gd^{3+} [107]. The magnetization and magnetic mass susceptibility of PEG-modified $BaGdF_5$ UCNPs at room temperature was found to be about 1.05 emu/g and 5.2 x 10^{-5} emu/g Oe at 20 kOe respectively. Importantly, these values are close to

the magnetization required for MRI and bio-separation applications [85], [107].

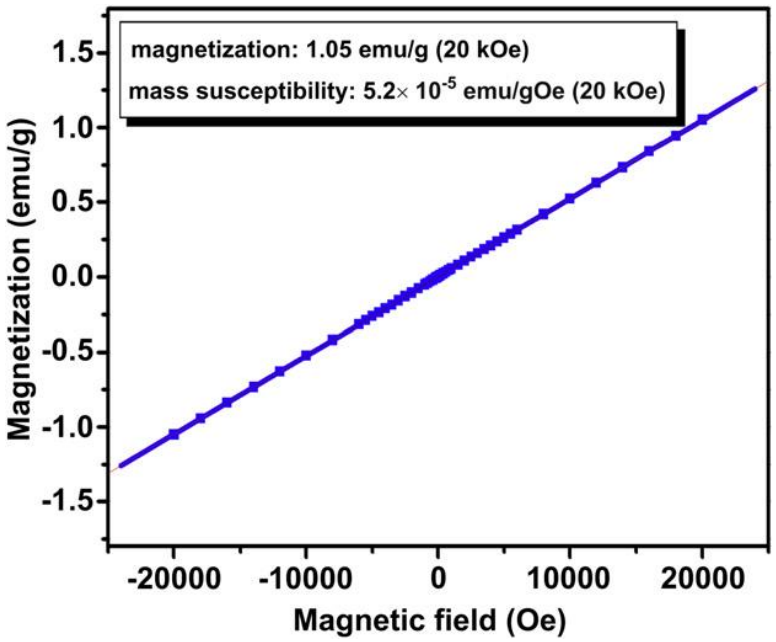

Figure 4.23 Magnetization as a function of applied magnetic field of PEG-modified $BaGdF_5$:Yb/Er UCNPs at room temperature.

Chapter 5 Conclusions and suggestions for future work

5.1 Conclusions

The present work aims to develop a new generation of fluorescent labeling agents based on RE doped phosphor. All RE doped phosphors are synthesized by a one-step hydrothermal method with surface modifiers to enhance water dispersibility.

Bi-functional $NaGdF_4$:Yb/Er UC phosphors with fixed amount of 3MPA, PEG and PEI possess UC and paramagnetic properties. Contrary to those common approaches, a simple protocol for simultaneous control of α to β-$NaGdF_4$ and tunable UC emission with different RGRs are demonstrated in 3MPA, PEG and PEI modified phosphors. When the phase was changed from α to β-$NaGdF_4$, the shape of phosphors was changed from a mixture of rods and spherical particles to pure spherical particles. Upon excitation of 980 nm laser, the phosphors exhibited tunable UC luminescence. Additionally, PEG modified phosphors exhibited intense CL emission under low voltage electron beam irradiation. Also, the phosphors possessed paramagnetic behavior with magnetic mass susceptibility and magnetization of 8.36×10^{-5} emu/gOe and 1.538 emu/g at 20 kOe. These results demonstrated that the phase, shape, and UC colors could be simultaneously modified simply by adjusting the surface modification agents. It is expected that these phosphors with tunable UC and paramagnetic property have high potential applications in lightings, anti-fake labeling systems and displays.

Besides, water dispersible Ba_2LaF_7:Yb/Er UCNPs were synthesized by simple and low temperature one-step hydrothermal reaction. While maintaining detectable upconversion luminescence for bioimaging application, the as-synthesized UCNPs

presented pure cubic phase structure, which had completely been absent of phase transition leading to large size in most reported UCNPs. The small-size UCNPs with PEI modification enable them to be suitable for bioprobe and the Ba_2LaF_7:Yb/Er UCNPs had successfully demonstrated fluorescent bioimaging in HeLa cells. Also, the Ba_2LaF_7:Yb/Er UCNPs exhibited a low toxicity at high concentrations. As a result, the Ba_2LaF_7:Yb/Er UCNPs are expected to be a very useful fluorescent bioprobe.

Furthermore, a new type of bi-modal imaging probe based on PEI modified $BaGdF_5$:Yb/Er UCNPs was synthesized for fluorescent imaging and T_1-weighted MRI applications. The PEI modified $BaGdF_5$:Yb/Er UCNPs have an average size of about 10 nm, making them ideal for bioprobes,. Owing to the positively charged amino group (+27.6 mV) on the surface, the novel UCNPs have high water solubility and could readily enter the cells. The as-prepared UCNPs were successfully used as fluorescent labels for the effective imaging of HeLa cells and the local luminescence ascribed to the energy transition of Er^{3+} ion was observed from fluorescent microscopy. Cytotoxicity assays revealed that the as-prepared UCNPs possess low toxicity. Moreover, $BaGdF_5$:Yb/Er UCNPs presented excellent paramagnetic property and relatively large longitudinal relaxivity of 1.194 S^{-1} mM^{-1}. Importantly, T_1-weighted MRI showed that the PEI modified $BaGdF_5$:Yb/Er UCNPs could be used as T_1-MRI contrast agent.

Additionally, PEG-modified $BaGdF_5$:Yb/Er UCNPs nanoprobe with optimal small size for tri-modal UC luminescence/CT/magnetic imaging was developed by a simple one-pot hydrothermal method for the first time. Apart from previously reported UC *in-vitro* fluorescent imaging and MRI applications, the enhanced CT phantom images revealed the feasibilities of using these UCNPs for CT contrast agent. Moreover,

in-vivo CT image of a mouse demonstrated the prolong enhancement of signal of spleen for 2 h. More importantly, the long circulation time *in-vivo* of these UCNPs could help to detect splenic diseases and future targeted tumor imaging. Besides, owing to the different X-ray absorption coefficients of Ba and Gd, the PEG-modified $BaGdF_5$:Yb/Er UCNPs can be used as a CT contrast agent at different operating voltages for various group of patients.

5.2 Suggestions for future work

A multi-modal imaging agent, $BaGdF_5$:Yb/Er UCNPs has been developed in this work. The three imaging techniques including fluorescent, MRI and CT are important to reveal internal structure, functions and diseases of cells, tissues and organs. Owing to the attractive results, we believe that UCNPs have great potential for future biological applications. The following suggestions can be regarded as an extension of the present work.

The present UCNPs emit intense visible radiation only. As a result, *in-vitro* fluorescent imaging is limited to visible region. However, some RE activators, such as Tm^{3+} and Yb^{3+} can emit NIR radiation upon illumination of NIR radiation. Therefore, NIR-NIR fluorescent imaging can be carried out *in-vitro* or *in-vivo* in the future study.

Owing to the small size and polar surface of UCNPs, the UCNPs can be conjugated with other types of bio materials such as DNA, peptides and avidin. After conjugation, the UCNPs can be used as a bio-sensing system through the fluorescent resonance energy transfer (FRET) mechanism to sense the existence or the change in amount of bio materials by photoluminescence.

Besides, nowadays, tracking tumor cells is a trend in modern bioimaging. Hence, the surface of UCNPs can be modified according to the surface protein of specific tumor cells. After conjugation to tumor cells, photodynamic therapy (PDT) can be carried out at the same time to kill cancer cells by using radicals.

References

[1] W. M. Yen, S. Shionoya and H. Yamamoto, Phosphor handbook, CRC Press/Taylor and Francis, 2007.

[2] H. T. Wong, H. L. W. Chan and J. H. Hao, "Magnetic and luminescent properties of multifunctional GdF_3:Eu^{3+} nanoparticles," *App. Phys. Lett.,* vol. 95, p. 022512, 2009.

[3] J. H. Zeng, J. Su, Z. H. Li, R. X. Yan and Y. D. Li, "Synthesis and upconversion luminescence of hexagonal-phase $NaYF_4$:Yb, $Er3^+$ phosphors of controlled size and morphology," *Adv. Mater.,* vol. 17, p. 2119, 2005.

[4] F. Wang, D. K. Chatterjee, Z. Q. Li, Y. Zhang, M. Q. W. X. P. Fan and M. Q. Wang, X. P. Fan and M. Q. Wang, "Synthesis of polyethylenimine/$NaYF_4$ nanoparticles with upconversion fluorescence," *Nanotechnology,* vol. 17, p. 5786, 2006.

[5] L. Wang and Y. Li, "Controlled synthesis and luminescence of lanthanide doped $NaYF_4$ nanocrystals," *Chem. Mater.,* vol. 19, p. 727, 2007.

[6] F. Auzel, "Upconversion and anti-stokes processes with f and d ions in solids," *Chem. Rev.,* vol. 104, p. 139, 2004.

[7] S. Sivakumar, F. V. Veggal and P. S. May, "Near-infrared (NIR) to red and green up-conversion emission from silica sol−gel thin films made with $La_{0.45}Yb_{0.5}0Er_{0.05}F_3$ nanoparticles, hetero-looping-enhanced energy transfer (hetero-LEET): A new up-conversion process," *J. Am. Chem. Soc.,* vol. 129, p. 620, 2007.

[8] Y. Liu, D. Tu, H. Zhu and X. Chen, "Lanthanide-doped luminescent nanoprobes: controlled synthesis, optical spectroscopy, and bioapplications (advance article)," *Chem. Soc. Rev.,* 2013.

[9] F. Wang, R. Deng, J. Wang, Y. H., H. Zhu, X. Chen and X. Liu, “Tuning upconversion through energy migration in core–shell nanoparticles,” *Nature Mater.,* vol. 10, p. 968, 2011.

[10] F. Wang, W. B. Tan, Y. Zhang, X. P. Fan and M. Q. Wang, "Luminescent nanomaterials for biological labelling," *Nanotechnology,* vol. 17, p. R1, 2006.

[11] J. F. Suyver, A. Aebischer, D. Biner, P. Gerner, J. Grimm, S. Heer, K. W. Kramer, C. Reinhard and H. U. Gudel, "Novel materials doped with trivalent lanthanides and transition metal ions showing near-infrared to visible photon upconversion," *Opt. Mater.,* vol. 27, p. 1111, 2005.

[12] M. Hasse and H. Schafer, "Upconverting nanoparticles," *Angew. Chem. Int. Ed.,* vol. 50, p. 5808, 2011.

[13] H. Kobayashi, N. Kosaka, M. Ogawa, N. Y. Morgan, P. D. Smith, C. B. Murray, X. C. Ye, J. Collins, G. A. Kumar, H. Bell and P. L. Choyke, "In vivo multiple color lymphatic imaging using upconverting nanocrystals," *J. Mater. Chem.,* vol. 19, p. 6481, 2009.

[14] D. R. Gamelin and H. U. Gudel, "Design of luminescent inorganic materials: new photophysical processes studied by optical spectroscopy," *Acc. Chem. Res.,* vol. 33, p. 235, 2000.

[15] F. Wang and X. G. Liu, "Recent advances in the chemistry of lanthanide-doped upconversion nanocrystals," *Chem. Soc. Rev.,* vol. 38, p. 976, 2009.

[16] J. S. Chivian, W. E. Case and D. D. Eden, "The photon avalanche: A new phenomenon in Pr^{3+}-based infrared quantum counters," *Applied Physics Letter,* vol. 35, p. 124, 1979.

[17] H. Chen, X. Zhai, D. Li, L. Wang, D. Zhao and W. P. Qin, "Water-soluble Yb^{3+}, Tm^{3+} codoped $NaYF_4$ nanoparticles: Synthesis, characteristics and bioimaging," *J. Alloys. Compd.,* vol. 511, p. 70, 2012.

[18] T. Sandrock, H. S. Cheife, E. Heumann and G. Huber, "High-power continuous-wave upconversion fiber laser at room temperature," *Opt. Lett.,* vol. 22, p. 808, 1997.

[19] E. Downing, L. Hesselin, J. Ralston and R. Macfarlane, "A three-color, solid-State, three-dimensional display," *Science,* vol. 273, p. 1185, 1996.

[20] J. W. Stouwdam and V. F. C. J. M. Veggal, "Near-infrared emission of redispersible Er^{3+}, Nd^{3+}, and Ho^{3+} doped LaF_3 nanoparticles," *Nano Lett.,* vol. 2,

p. 733, 2002.

[21] Z. Xu, C. Li, P. Yang, C. Zhang, S. Huang and J. Lin, "Rare earth fluorides nanowires/nanorods derived from hydroxides: hydrothermal synthesis and luminescence properties," *Cryst. Growth Des.,* vol. 9, p. 4752, 2009.

[22] R. Yan and Y. Li, "Down/up conversion in Ln^{3+}-doped YF_3 nanocrystals," *Adv. Funct. Mater.,* vol. 15, p. 763, 2005.

[23] S. Heer, K. Kompe, H. U. Gudel and M. Haase, "Highly efficient multicolour upconversion emission in transparent colloids of lanthanide-doped $NaYF_4$ nanocrystals," *Adv. Mater.,* vol. 16, p. 2102, 2004.

[24] F. Wang and X. Liu, "Upconversion multicolor fine-tuning: visible to near-infrared emission from lanthanide-doped $NaYF_4$ nanoparticles," *J. Am. Chem. Soc.,* vol. 130, p. 5642, 2008.

[25] Z. Li and Y. Zhang, "Monodisperse silica-coated polyvinylpyrrolidone/$NaYF_4$ nanocrystals with multicolor upconversion fuorescence emission," *Angew Chem.,* vol. 45, p. 7732, 2006.

[26] G. Yi, H. Lu, S. Zhao, Y. Ge, W. Yang, D. Chen and L. H. Guo, "Synthesis, characterization, and biological application of size-controlled nanocrystalline $NaYF_4$:Yb,Er infrared-to-visible up-conversion phosphors," *Nano Lett.,* vol. 4, p. 2191, 2004.

[27] D. Jiles, in *Introduction to magnetism and magnetic Materials*, London, Chapman and Hall, 1998, pp. 9,11.

[28] J. R. Christman, Fundamentals of solid state physics, New York: Wiley, 1988.

[29] G. S. Yi and G. M. Chow, "Synthesis of hexagonal-phase $NaYF_4$:Yb,Er and $NaYF_4$:Yb,Tm nanocrystals with efficient up-conversion fluorescence," *Adv. Funct. Mater.,* vol. 16, p. 2324, 2006.

[30] G. Y. Chen, T. Y. Ohulchansky, B. Kumar, H. Agren and P. N. Prasad, "Ultrasmall monodisperse $NaYF_4$:Yb^{3+}/Tm^{3+} nanocrystals with enhanced near-infrared to near-infrared upconversion photoluminescence," *ACS Nano,* vol. 4, p. 3163, 2010.

[31] G. Yi and G. Chow, "Colloidal LaF_3:Yb,Er, LaF_3:Yb,Ho and LaF_3:Yb,Tm nanocrystals with multicolor upconversion fluorescence," *J. Mater. Chem.,* vol.

15, p. 4460, 2005.

[32] Y. Zhang, X. Sun, R. Si, L. You and C. Yan, "Single-crystalline and monodisperse LaF_3 triangular nanoplates from a single-source precursor," *J. Am. Chem. Soc.,* vol. 127, p. 3260, 2005.

[33] J. C. Boyer, L. A. Cuccia and J. A. Capobianco, "Synthesis of colloidal upconverting $NaYF_4$: Er^{3+}/Yb^{3+} and Tm^{3+}/Yb^{3+} monodisperse nanocrystals," *Nano Lett.,* vol. 7, p. 847, 2007.

[34] F. Zhang, Y. Wan, T. Yu, F. Zhang, Y. Shi, S. Xie, Y. Li, L. Xu, B. Tu and D. Zhao, "Uniform nanostructured arrays of sodium rare-earth fluorides for highly efficient multicolor upconversion luminescence," *Angew. Chem. Int. Ed.,* vol. 46, p. 7976, 2007.

[35] F. Vetrone, J. C. Boyer, J. A. Capobianco, A. Speghini and M. Bettinelli, "Significance of Yb^{3+} concentration on the upconversion mechanisms in codoped Y_2O_3:Er^{3+}, Yb^{3+} nanocrystals," *J. Appl. Phys.,* vol. 96, p. 661, 2004.

[36] X. Luo and W. Cao, "Ethanol-assistant solution combustion method to prepare La_2O_2S:Yb, Pr nanometer phosphor," *J. Alloys Compd.,* vol. 460, p. 529, 2008.

[37] Y. Liu, D. Tu, H. Zhu, E. Ma and X. Chen, "Lanthanide-doped luminescent nano-bioprobes: from fundamentals to biodetection," *Nanoscale,* vol. 5, p. 1369, 2013.

[38] T. Terai and T. Nagano, "Fluorescent probes for bioimaging applications," *Curr. Opin. Chem. Biol.,* vol. 12, p. 515, 2008.

[39] M. Beija, C. A. M. Afonso and J. M. G. Martinho, "Synthesis and applications of Rhodamine derivatives as fluorescent probes," *Chem. Soc. Rev.,* vol. 38, p. 2410, 2009.

[40] M. Zhang, M. X. Yu, F. Y. Li, M. W. Zhu, M. Y. Li, Y. H. Gao, L. Li, Z. Q. Liu, J. P. Zhang, D. Q. Zhang, T. Yi and C. H. Huang, "A highly selective fluorescence turn-on sensor for cysteine/homocysteine," *J. Am. Chem. Soc.,* vol. 129, p. 10322, 2007.

[41] X. Michalet, F. F. Pinaud, L. A. Bentolila, J. M. Tsay, S. Doose, J. J. Li, G. Sundaresan, A. M. Wu, S. S. Gambhir and S. Weiss, "Quantum dots for live cells, in vivo imaging, and diagnostics," *Science,* vol. 307, p. 538, 2005.

[42] Q. B. Wang, Y. Liu, Y. G. Ke and H. Yan, "Quantum dot bioconjugation during core–shell synthesis," *Angew. Chem. Int. Ed.,* vol. 47, p. 316, 2008.

[43] J. Zhou, Z. Lin and F. Y. Li, "Upconversion nanophosphors for small-animal imaging," *Chem. Soc. Rev.,* vol. 41, p. 1323, 2012.

[44] W. M. Yen and M. J. Weber, Inorganic phosphors: Compositions, preparations and optical properties, Florida: CRC Press, 2004.

[45] G. Blasse and B. C. Grabmaier, Luminscent materials, Berlin: Springer, 1994.

[46] F. Wang, D. Banerjee, Y. Liu, X. Chen and X. Liu, "Upconversion nanoparticles in biological labeling, imaging, and therapy," *Analyst,* vol. 135, p. 1839, 2010.

[47] D. Dolmans, D. Fukumura and R. K. Jain, "Photodynamic therapy for cancer," *Nat. Rev. Cancer,* vol. 3, p. 380, 2003.

[48] D. Tu, L. Liu, Q. Ju, Y. Liu, H. Zhu, R. Li and X. Chen, "Time-resolved FRET biosensor based on amine-functionalized lanthanide-doped $NaYF_4$ nanocrystals," *Angew. Chem. Int. Ed.,* vol. 50, p. 6306, 2011.

[49] M. Wang, C. C. Mi, W. X. Wang, C. H. Liu, Y. F. Wu, Z. R. Xu, C. B. Mao and S. K. Xu, "Immunolabeling and NIR-excited fluorescent imaging of HeLa cells by using $NaYF_4$:Yb,Er upconversion nanoparticles," *ACS Nano,* vol. 3, p. 1580, 2009.

[50] S. F. Lim, R. Riehn, W. S. Ryu, N. Khanarian, C. K. Tung, D. Tankand and R. H. Austin , "In vivo and scanning electron microscopy imaging of up-converting nanophosphors in Caenorhabditis elegans," *Nano Lett.,* vol. 6, p. 169, 2006.

[51] Q. Liu, Y. Sun, T. Yang, W. Feng, C. Li and F. Y. Li, "Sub-10 nm hexagonal lanthanide-doped $NaLuF_4$ upconversion nanocrystals for sensitive bioimaging in vivo," *J. Am. Chem. Soc.,* vol. 133, p. 17122, 2011.

[52] C. T. Xu, J. Axelsson and S. A. Engels, "Fluorescence diffuse optical tomography using upconverting nanoparticles," *Appl. Phys. Lett.,* vol. 94, p. 251107, 2009.

[53] R. Kumar, M. Nyk, T. Y. Ohulchansky, C. A. Flask and P. N. Prasad, "Combined optical and MR bioimaging using rare earth ion doped $NaYF_4$ nanocrystals," *Adv. Funct. Mater.,* vol. 19, p. 853, 2009.

[54] G. K. Das, B. C. Heng, S. C. Ng, T. White, J. S. C. Loo, L. D. Silva, P.

Padmanabhan, K. K. Bhakoo, S. T. Selvan and T. T. Y. Tan, "Gadolinium oxide ultranarrow nanorods as multimodal contrast agents for optical and magnetic resonance imaging," *Langmuir,* vol. 26, p. 8959, 2010.

[55] G. Y. Chen, T. Y. Ohulchansky, W. C. Law, H. Agren and P. N. Prasad, "Monodisperse $NaYbF_4:Tm^{3+}/NaGdF_4$ core/shell nanocrystals with near-infrared to near-infrared upconversion photoluminescence and magnetic resonance properties," *Nanoscale,* vol. 3, p. 2003, 2011.

[56] S. J. Budijono, J. N. Shan, N. Yao, Y. Miura, T. Hoye, R. H. Austin, Y. G. Ju and R. K. Prud'homme, "Synthesis of stable block-copolymer-protected $NaYF_4:Yb^{3+}$, Er^{3+} up-converting phosphor nanoparticles," *Chem. Mater.,* vol. 22, p. 311, 2010.

[57] G. S. Yi, Y. F. Peng and Z. Q. Gao, "Strong red-emitting near-infrared-to-visible upconversion fluorescent nanoparticles," *Chem. Mater.,* vol. 23, p. 2729, 2011.

[58] M. X. Yu, F. Y. Li, Z. G. Chen, H. Hu, C. Zhan, H. Yang and C. H. Huang, "Laser scanning up-conversion luminescence microscopy for imaging cells labeled with rare-earth nanophosphors," *Anal. Chem.,* vol. 81, p. 930, 2009.

[59] F. Vetrone, R. Naccache, A. J. d. l. Fuente, F. S. Rodríguez, A. B. Castro, E. M. Rodriguez, D. Jaque, J. G. Solé and J. A. Capobianco, "Intracellular imaging of HeLa cells by non-functionalized $NaYF_4:Er^{3+}$, Yb^{3+} upconverting nanoparticles," *Nanoscale,* vol. 2, p. 495, 2010.

[60] J. Chen, C. Guo, M. Wang, L. Huang, L. Wang, C. Mi, J. Li, X. Fang, C. Mao and S. Xu, "Controllable synthesis of $NaYF_4$:Yb,Er upconversion nanophosphors and their application to in vivo imaging of Caenorhabditis elegans," *J. Mater. Chem.,* vol. 21, p. 2632, 2011.

[61] Z. L. Wang, J. H. Hao and H. L. W. Chan, "Down- and up-conversion photoluminescence, cathodoluminescence and paramagnetic properties of $NaGdF_4$: Yb^{3+},Er^{3+} submicron disks assembled from primary nanocrystals," *J. Mater. Chem.,* vol. 20, p. 3178, 2010.

[62] S. J. Zeng, M. K. Tsang, C. F. Chan, K. L. Wong and J. H. Hao, "PEG modified $BaGdF_5$:Yb/Er nanoprobes for multi-modal upconversion fluorescent, in vivo X-ray computed tomography and biomagnetic imaging," *Biomaterials,* vol. 33, p.

9232, 2012.

[63] L. Wang and Y. Li, "$Na(Y_{1.5}Na_{0.5})F_6$ single-crystal nanorods as multicolor luminescent materials," *Nano Lett.,* vol. 6, p. 1645, 2006.

[64] G. Wang, Q. Peng and Y. Li, "Luminescence tuning of upconversion nanocrystals," *Chem. Eur. J.,* vol. 16, p. 4923, 2010.

[65] F. Zhang, J. Li, J. Shan, L. Xu and D. Y. Zhao, "Shape, size, and phase-controlled rare-earth fluoride nanocrystals with optical up-conversion properties," *Chem. Eur. J.,* vol. 15, p. 11010, 2009.

[66] J. H. Zeng, Z. H. Li, J. Su, L. Y. Wang, R. X. Yan and Y. D. Li, "Synthesis of complex rare earth fluoride nanocrystal phosphors," *Nanotechnology,* vol. 17, p. 3549, 2006.

[67] C. Li and J. Lin, "Rare earth fluoride nano-/microcrystals: synthesis, surface modification and application," *J. Mater. Chem.,* vol. 20, p. 6831, 2010.

[68] "Catalogue of FLSP920 from Edinburgh Instruments Limited," Edinburgh Instruments Limited, [Online]. Available: http://www.edinst.com/flsp920.htm. [Accessed 29 5 2013].

[69] "Catalogue of LakeShore 7407 of LakeShore," LakeShore, [Online]. Available: http://www.lakeshore.com/products/vibrating-sample-magnetometer/models/Pages/Overview.aspx. [Accessed 2 6 2013].

[70] J. Hao, Y. Zhang and X. Wei, "Electric-induced enhancement and modulation of upconversion photoluminescence in epitaxial $BaTiO_3$:Yb/Er thin films," *Angew. Chem. Int. Ed.,* vol. 50, p. 6876, 2011.

[71] K. J. Konig, "Multiphoton microscopy in life sciences," *Microsc.,* vol. 200, p. 83, 2000.

[72] Y. L. Song, Q. W. Tian, R. J. Zou, Z. G. Chen, J. M. Yang and J. Q. Hu, "Phase and luminescent intensity control of hydrophilic rare-earth up-converting nanophosphors prepared by one-pot solvothermal synthesis," *J. Alloys Compd.,* vol. 509, p. 6539, 2011.

[73] M. Sameiro and T. Goncalves, "Fluorescent labeling of biomolecules with organic probes," *Chem. Rev.,* vol. 109, p. 190, 2009.

[74] I. L. Medintz, A. R. Clapp, F. M. Brunel, T. Tiefenbrunn and H. T. Uyeda, "Proteolytic activity monitored by fluorescence resonance energy transfer through quantum-dot-peptide conjugates," *Nat. Mater.,* vol. 5, p. 581, 2006.

[75] J. Hao and M. Concivera, "Luminescent characteristics of blue-emitting $Sr_2B_5O_9Cl$:Eu thin-film phosphors," *Appl. Phys. Lett.,* vol. 79, p. 740, 2001.

[76] J. Hao and J. Gao, "Abnormal reduction of Eu ions and luminescence in CaB_2O_4: Eu thin films," *Appl. Phys. Lett.,* vol. 85, p. 3720, 2004.

[77] Y. Liu, D. Tu, H. Zhu, R. Li, W. Luo and X. Chen, "A strategy to achieve efficient dual-mode luminescence of Eu^{3+} in lanthanides doped multifunctional $NaGdF_4$ nanocrystals," *Adv. Mater.,* vol. 22, p. 3266, 2010.

[78] H. Zhu, R. Li, W. Luo and X. Chen, "Eu^{3+}-doped β-Ga_2O_3 nanophosphors: annealing effect, electronic structure and optical spectroscopy," *Phys. Chem. Chem. Phys.,* vol. 13, p. 4411, 2011.

[79] W. B. Niu, S. Wu, S. F. Zhang and L. Li, "Synthesis of colour tunable lanthanide-ion doped $NaYF_4$ upconversion nanoparticles by controlling temperature," *Chem. Commun.,* vol. 46, p. 3908, 2010.

[80] J. X. Meng, C. T. Yang and Q. Q. Chen, "Photoluminescence characterization of Ce^{3+} and Dy^{3+} doped Li_2CaGeO_4 phosphors," *J. Lumin.,* vol. 130, p. 1320, 2010.

[81] F. Wang, Y. Han, C. S. Lim, Y. H. Lu, J. Wang, J. Xu, H. Y. Chen, C. Zhang, M. H. Hong and X. Liu, "Simultaneous phase and size control of upconversion nanocrystals through lanthanide doping," *Nature,* vol. 463, p. 1061, 2010.

[82] S. J. Zeng, J. J. Xiao, Q. B. Yang and J. H. Hao, "Bi-functional $NaLuF_4$:Gd^{3+}/Yb^{3+}/Tm^{3+} nanocrystals: structure controlled synthesis, near-infrared upconversion emission and tunable magnetic properties," *J. Mater. Chem.,* vol. 22, p. 9870, 2012.

[83] W. B. Niu, S. Wu and S. F. Zhang, "A facile and general approach for the multicolor tuning of lanthanide-ion doped $NaYF_4$ upconversion nanoparticles within a fixed composition," *J. Mater. Chem.,* vol. 20, p. 9113, 2010.

[84] S. J. Zeng, G. Z. Ren, C. F. Xu and Q. B. Yang, "Modifying crystal phase, shape, size, optical and magnetic properties of monodispersed multifunctional $NaYbF_4$

nanocrystals through lanthanide doping," *Cryst. Eng. Comm.,* vol. 13, p. 4276, 2011.

[85] G. Z. Ren, S. J. Zeng and J. H. Hao, "Tunable multicolor upconversion emissions and paramagnetic property of monodispersed bifunctional lanthanide-doped $NaGdF_4$ nanorods," *J. Phys. Chem. C,* vol. 115, p. 20141, 2011.

[86] S. J. Zeng, M. K. Tsang, C. F. Chan, K. L. Wong, B. Fei and J. H. Hao, "Dual-modal fluorescent/magnetic bioprobes based on small sized upconversion nanoparticles of amine-functionalized $BaGdF_5$:Yb/Er," *Nanoscale,* vol. 4, p. 5118, 2012.

[87] Z. H. Xu, C. X. Li, D. M. Yang, W. X. Wang, X. J. Kang, M. Shang and J. Lin, "Self-templated and self-assembled synthesis of nano/microstructures of Gd-based rare-earth compounds: morphology control, magnetic and luminescence properties," *Phys. Chem. Chem. Phys.,* vol. 12, p. 11315, 2010.

[88] Z. L. Wang, J. H. Hao, H. L. W. Chan, G. L. Law, W. T. Wong, K. L. Wong, M. B. Murphy, T. Su, Z. H. Zhang and S. Q. Zeng, "Simultaneous synthesis and functionalization of water-soluble up-conversion nanoparticles for in-vitro cell and nude mouse imaging," *Nanoscale,* vol. 3, p. 2175, 2011.

[89] K. Kamimura, D. Miyanoto, Y. Saito, K. Soga and Y. Nagasaki, "Design of poly(ethylene glycol)/streptavidin coimmobilized upconversion nanophosphors and their application to fluorescence biolabeling," *Langmuir,* vol. 24, p. 8864, 2008.

[90] W. J. Kim, M. Nyk and P. N. Prasad, "Color-coded multilayer photopatterned microstructures using lanthanide (III) ion co-doped $NaYF_4$ nanoparticles with upconversion luminescence for possible applications in security," *Nanotechnology,* vol. 20, p. 185301, 2009.

[91] H. Y. Du, W. H. Zhang and J. Y. Sun, "Structure and upconversion luminescence properties of $BaYF_5$:Yb^{3+}, Er^{3+} nanoparticles prepared by different methods," *J. Alloys Compd.,* vol. 509, p. 3413, 2011.

[92] S. Wu, G. Han, D. J. Milliron, S. Aloni, V. Altoe, D. V. Talapin, B. C. Cohen and P. J. Schuck, "Non-blinking and photostable upconverted luminescence from

single lanthanide-doped nanocrystals," *PNAS,* vol. 106, p. 10917, 2009.

[93] J. C. Boyer and V. F. C. J. M. Veggal, "Absolute quantum yield measurements of colloidal $NaYF_4$: Er^{3+}, Yb^{3+} upconverting nanoparticles," *Nanoscale,* vol. 2, p. 1417, 2010.

[94] C. Feldman, "Range of 1-10 kev electrons in solids," *Phy. Rev.,* vol. 117, p. 455, 1960.

[95] H. T. Wong, F. Vetrone, R. Naccache, H. L. W. Chan, J. Hao and J. A. Capobianco, "Water dispersible ultra-small multifunctional $KGdF_4$:Tm^{3+}, Yb^{3+} nanoparticles with near-infrared to near-infrared upconversion," *J. Mater. Chem.,* vol. 21, p. 16589, 2011.

[96] P. Sharma, S. Brown, G. Walter, S. Santra and B. Moudgil, "Nanoparticles for bioimaging," *Adv. Colloid Interface Sci.,* vol. 123, p. 471, 2006.

[97] W. C. Chan, D. J. Maxwell, X. Gao, R. E. Bailey, M. Han and S. Nie, "Luminescent quantum dots for multiplexed biological detection and imaging," *Curr. Opin. Biotechnol.,* vol. 13, p. 40, 2002.

[98] Z. Q. Li, Y. Zhang and S. Jiang, "Multicolor core/shell-structured upconversion fluorescent nanoparticles," *Adv. Mater.,* vol. 20, p. 4765, 2008.

[99] J. C. Boyer, F. Vetrone, L. A. Cuccia and J. A. Capobianco, "Synthesis of colloidal upconverting $NaYF_4$ nanocrystals doped with Er^{3+}, Yb^{3+} and Tm^{3+}, Yb^{3+} via thermal decomposition of lanthanide trifluoroacetate precursors," *J. Am. Chem. Soc.,* vol. 128, p. 7444, 2006.

[100] L. Wang and Y. Li, "Green upconversion nanocrystals for DNA detection," *Chem. Commun.,* p. 2557, 2006.

[101] L. Wang, R. Yan, Z. Huo, L. Wang, J. Zeng, J. Bao, X. Wang, Q. Peng and Y. Li, "Fluorescence resonant energy transfer biosensor based on upconversion-luminescent nanoparticles," *Angew. Chem. Int. Ed.,* vol. 44, p. 6054, 2005.

[102] R. Deng, X. Xie, M. Vendrell, Y. T. Chang and X. Liu, "Intracellular glutathione detection using MnO_2-nanosheet-modified upconversion nanoparticles," *J. Am. Chem. Soc.,* vol. 133, p. 20168, 2011.

[103] D. K. Chatterjee, A. J. Rufaihah and Y. Zhang, "Upconversion fluorescence

imaging of cells and small animals using lanthanide doped nanocrystals," *Biomaterials,* vol. 29, p. 937, 2008.

[104] M. Nyk, R. Kumar, T. Y. Ohulchansky, E. J. Bergey and P. N. Prasad, "High contrast in vitro and in vivo photoluminescence bioimaging using uear infrared to near infrared up-conversion in Tm^{3+} and Yb^{3+} doped fluoride nanophosphors," *Nano Lett.,* vol. 8, p. 3834, 2008.

[105] J. Zhou, Y. Sun, X. X. Du, L. Q. Xiong, H. Hu and F. Y. Li, "Dual-modality in vivo imaging using rare-earth nanocrystals with near-infrared to near-infrared (NIR-to-NIR) upconversion luminescence and magnetic resonance properties," *Biomaterials,* vol. 31, p. 3287, 2010.

[106] C. F. Xu, M. Ma, L. W. Yang, S. J. Zeng and Q. Yang, "Lanthanide doping-facilitated growth of ultrasmall monodisperse Ba_2LaF_7 nanocrystals with excellent photoluminescence," *J. Col. Int. Sci.,* vol. 368, p. 49, 2012.

[107] H. T. Wong, M. K. Tsang, C. F. Chan, K. L. Wong, B. Fei and J. Hao, "In-vitro cell imaging using multifunctional small sized $KGdF_4:Yb^{3+}$, Er^{3+} upconverting nanoparticles synthesized by one-pot solvothermal process," *Nanoscale,* vol. 5, p. 3465, 2013.

[108] Q. Ju, D. T. Tu, Y. S. Liu, R. F. Li, H. M. Zhu, J. C. Chen, Z. Chen, M. Huang and X. Y. Chen, "Amine-functionalized lanthanide-doped $KGdF_4$ nanocrystals as potential optical/magnetic multimodal bioprobes," *J. Am. Chem. Soc.,* vol. 134, p. 1323, 2012.

[109] D. M. Yang, C. X. Li, G. G. Li, M. M. Shang, X. J. Kang and J. Lin, "Colloidal synthesis and remarkable enhancement of the upconversion luminescence of $BaGdF_5:Yb^{3+}/Er^{3+}$ nanoparticles by active-shell modification," *J. Mater. Chem.,* vol. 21, p. 5923, 2011.

[110] J. F. Jin, Y. J. Gu, C. W. Y. Man, J. P. Cheng, Z. H. Xu, Y. Zhang, H. S. Wang, V. H. Y. Lee, S. H. Cheng and W. T. Wong, "Polymer-coated $NaYF_4:Yb^{3+}$, Er^{3+} upconversion nanoparticles for charge-dependent cellular imaging," *ACS Nano,* vol. 5, p. 7838, 2011.

[111] M. Han, X. Gao, J. Z. Su and S. Nie, "Quantum-dot-tagged microbeads for

multiplexed optical coding of biomolecules," *Nat. Biotecholo.,* vol. 19, p. 631, 2001.

[112] C. Wang, L. Cheng and Z. Liu, "Drug delivery with upconversion nanoparticles for multi-functional targeted cancer cell imaging and therapy," *Biomaterials,* vol. 32, p. 1110, 2010.

[113] J. H. Lee, Y. M. Huh, Y. Jun, J. Seo, J. Jang and H. T. Song et. al, "Artificially engineered magnetic nanoparticles for ultra-sensitive molecular imaging," *Nat. Med.,* vol. 13, p. 95, 2007.

[114] Y. Park, J. H. Kim, K. T. Lee, K. S. Jeon, H. B. Na and J. H. Yu et. al, "Nonblinking and nonbleaching upconverting nanoparticles as an optical imaging nanoprobe and T_1 magnetic resonance imaging contrast agent," *Adv. Mater.,* vol. 21, p. 4467, 2009.

[115] F. Hallouard, N. Anton, P. Choquet and A. Constantinesco, "Iodinated blood pool contrast media for preclinical X-ray imaging applications - A review," *Biomaterials,* vol. 31, p. 6249, 2010.

[116] W. H. Kong, W. J. Lee, Z. Y. Cui, K. H. Bae, T. G. Park and J. H. Kim et. al, "Nanoparticulate carrier containing water-insoluble iodinated oil as a multifunctional contrast agent for computed tomography imaging," *Biomaterials,* vol. 28, p. 5555, 2007.

[117] Y. Liu, K. Ai, J. Liu, Q. Yuan, Y. He and L. Lu, "A high-performance ytterbium-based nanoparticulate contrast agent for in vivo X-ray computed tomography imaging," *Angew. Chem. Int. Ed.,* vol. 51, p. 1437, 2012.

[118] S. Santra, H. Yang, P. H. Holloway, J. T. Stanley and R. A. S. Mericle, "Synthesis of water-dispersible fluorescent, radio-opaque, and paramagnetic CdS:Mn/ZnS quantum dots: A multifunctional probe for bioimaging," *J. Am. Chem. Soc.,* vol. 127, p. 1656, 2005.

[119] Z. L. Wang, J. H. Hao, H. L. W. Chan, W. T. Wong and K. L. Wong, "A strategy for simultaneously realizing the cubic-to-hexagonal phase transition and controlling the small size of $NaYF_4$:Yb^{3+},Er^{3+} nanocrystals for in vitro cell imaging," *Small,* vol. 8, p. 1863, 2012.

[120] H. Y. Xing, W. B. Bu, S. J. Zhang, X. P. Zheng, M. Li and F. Chen et. al, "Multifunctional nanoprobes for upconversion fluorescence, MR and CT trimodal imaging," *Biomaterials,* vol. 33, p. 1079, 2012.

[121] S. B. Yu and A. D. Watson, "Metal-based X-ray contrast media," *Chem. Rev.,* vol. 99, p. 2353, 1999.

[122] "Tables of X-ray mass attenuation coefficients," The U.S. Department of Commerce, [Online]. Available: http://physics.nist.gov/PhysRefData/XrayMassCoef/. [Accessed 30 5 2013].